UNIVERSITY OF CALIFORNIA, SAN DIEGO

InGaAsP/InP Intrastep Quantum Wells for Enhanced Solar Energy Conversion

A dissertation submitted in partial satisfaction of the
requirements for the degree Doctor of Philosophy

in

Electrical Engineering (Applied Physics)

by

Winnie Chen

Committee in charge:

> Professor Paul K.L. Yu, Chair
> Professor Prabhakar R. Bandaru
> Professor Clifford P. Kubiak
> Professor S.S. Lau
> Professor Yu-Hwa Lo
> Professor J.J. Song

2012

The Dissertation of Winnie Chen is approved, and it is acceptable in quality and form
for publication on microfilm and electronically:

_____

_____

_____

_____

_____

_____
Chair

University of California, San Diego

2012

DEDICATION

To my parents.

EPIGRAPH

*The people that walked in darkness have seen a great light:
they that dwell in the land of the shadow of death, upon them
hath the light shined.*

Isaiah 9:2, KJV

TABLE OF CONTENTS

LIST OF FIGURES

LIST OF TABLES

ACKNOWLEDGEMENTS

First and foremost I would like to acknowledge my dissertation advisor, Professor Paul Yu, whose guidance and support in research in the last seven years has been invaluable to my career. My first impression of Paul was during ECE graduate student recruitment before I decided to attend UCSD, during which time he was chair of the department, and he walked with all of the potential students from our hotel uphill through campus. He always made time around his hectic schedule (even when he was traveling) to meet with his students for discussion of our research. I'm especially grateful for the opportunity to co-author a patent on the solar spectral condenser, which was a project funded by the Von Liebig Center at UCSD.

I am most indebted to my unofficial advisor for the seven years of graduate school, Professor S. S. Lau, who was not only my teacher of academics but also of character and confidence. I am most grateful for the opportunity to work with Dr. Lau as a TA for ECE 136L and ECE 134, which funded over a third of my graduate studies, and for the desk in his lab among his students, which I occupied to do most of my work. I wish Dr. Lau the best and more in his retirement.

I would like to thank Professor Edward Yu, who is now at UT Austin, for giving me the opportunity to be part of the Von Liebig/DOE project on quantum well solar cells, a project that funded another third of my graduate studies. I would also

2005	B. S., Electrical Engineering
	University of California, Irvine
2007	M. S., Electrical Engineering (Applied Physics)
	University of California, San Diego
2009	C. Phil., Electrical Engineering (Applied Physics)
	University of California, San Diego
2012	Ph. D., Electrical Engineering (Applied Physics)
	University of California, San Diego

PUBLICATIONS

• Peng Chen, **Winnie V. Chen**, Paul K. L. Yu, Chak Wah Tang, Kei May Lau, Luke Mawst, Charles Paulson, T. F. Kuech, and S. S. Lau, "Effects of hydrogen implantation damage on the performance of InP/InGaAs/InP *p-i-n* photodiodes transferred on silicon," Appl. Phys. Lett. 94, 012101 (2009).

• D. Derkacs, **W. V. Chen**, P. M. Matheu, S. H. Lim, P. K. L. Yu, and E. T. Yu, "Nanoparticle-induced light scattering for improved performance of quantum-well solar cells," Appl. Phys. Lett. 93, 091107 (2008).

• Daniel Derkacs, **Winnie V. Chen**, Peter Matheu, Swee H. Lim, Paul K. L. Yu, and E. T. Yu, "Coupling of light scattered by nanoparticles into waveguide modes in quantum-well solar cells" (Proceedings Paper), Proc. SPIE, Vol. 7047, 704703 (2008).

ABSTRACT OF THE DISSERTATION

InGaAsP/InP Intrastep Quantum Wells for Enhanced Solar Energy Conversion

by

Winnie Chen

Doctor of Philosophy in Electrical Engineering (Applied Physics)

University of California, San Diego, 2012

Professor Paul K. L. Yu, Chair

This dissertation explores innovative ways of improving efficiency of solar energy harvesting devices and evaluates them both analytically and experimentally. Two devices of different energy-harvesting mechanisms are presented: (1) intra-step quantum well (IQW) photovoltaic solar cell and (2) solar spectral condenser with IQWs. The IQW structure, step-like Type 1 (straddling gap) heterojunction structure, is used in both devices in order to help increase the conversion efficiency from solar photons to harvestable energy.

Chapter 1 introduces the context of the research done, outlining an overview of past and present achievements in solar energy research. Chapter 2 describes the physical principles of the ideal solar cell, how to increase its efficiency, and figures of merit. In Chapter 3 the effect of IQWs compared with regular QWs in the solar cell are calculated using Schodinger's equations. In Chapter 4 the experimental results comparing bulk InP, regular QW, and IQW solar cells are presented and discussed. The solar cell sample with IQWs proved to have better efficiency than the cell with regular QWs and the bulk InP cell. In Chapter 5 the solar spectral condenser, which converts random, broad-spectrum solar light into guided, narrow spectrum photons to be collected by optical fibers, is studied. Design and expected performance of the solar spectral condenser device based on a slab waveguide with absorbing IQWs is presented. In Chapter 6, fabrication, experimental setup, and measurement results for the solar spectral condenser device are presented and discussed. The solar spectral condenser proved to amplify the seed laser at the expected wavelength when exposed to concentrated solar illumination. Chapter 7 summarizes the dissertation and outlines some future work. The goal of this research is to break new ground in solar cell research by studying a new structure, the IQW, for photovoltaic cells, and inventing a new device, the solar spectral condenser. The calculations and simulations were done based on principles in optoelectronics, which focused on photodetectors and lasers, but are applied to solar cells. The measurement setup for the solar spectral condenser is a completely new and original idea.

Chapter 1

Introduction to Solar Cells

1.1   Introduction

Solar energy is an important global topic due to two main factors: worldwide need for more energy and global need for cleaner energy. While fossil fuel energy sources are being depleted and the safety of nuclear energy is being debated, alternative energy sources are needed to keep up with the world's energy consumption. Solar energy's source, the sun, is not only clean and safe but also abundant, supplying more than 170,000TW of power to the earth at any given moment, enough in about one hour to supply energy for the world for one year at the current energy consumption rate [1, 2]. In addition, it is obvious that the energy the sun shines on the earth will not deplete due to use. In this context, it might not be too hard to imagine a world fully powered by non-renewable energy sources.

However, the energy from the sun has not yet been used to its full potential. World solar PV (photovoltaic) capacity (grid-connected, installed PV) was about 30GW in 2011, with approximately 22GW in Europe and 2GW in the U.S., but could

increase significantly with aggressive policy changes and economic incentives [3]. In 2010, solar energy accounted for only 0.2% of all U.S. energy production, including PV (photovoltaic) and CSP (concentrated solar power), but still has a lot of potential to grow with implementation of government policy [4].

While policymakers and the market drive the solar power industry, the scientific community must also work on how to more economically and efficiently harvest, store, and transport the solar energy. Solar energy harvesting has been improved using methods such as concentrating sunlight (for instance, with mirrors and lenses), which decreases entropy and thus increases the efficiency thermodynamically, and increasing the intrinsic absorption efficiency of the active material. Usually grid-connected PV modules can provide electricity directly to the grid to be distributed centrally. The conversion loss from DC power generated by the PV module to AC for the grid can range around 2-10%, depending on the quality of the inverter used. Once into the grid, solar power suffers the same losses as any other source, and improvements can be made with programs such as the Smart Grid. Storage of PV-generated power in chemical batteries, capacitors, and even thermal masses, can be done. Concentrated solar power, which uses mirrors to concentrate sunlight, stores thermal power from the sun that can be used to generate electrical power by boiling water to rotate turbines in a thermal generator.

1.2   Timeline of solar cell technologies

Photovoltaic solar cells have been around since the 1950s, just after the time the first field-effect transistors were made.   Silicon-based solar cells with efficiencies of about 5-10% were first widely produced and used for space applications [5] . Since then, the worldwide race for the best efficiency and/or lowest cost solar cells has borne a variety of different PV cells. The best reported research solar cells (i.e., produced and tested in the lab), according to NREL (National Renewable Energy Laboratory) are shown in Figure 1-1 [6]. In the figure the different colored lines represent the different solar cell technologies, each beginning with one revolutionary idea represented by the first point of each line, followed by notable improvements in subsequent years by the same or different groups. For example, the group in RCA that published the first thin-film amorphous Si solar cells in 1976 [7] with samples that exhibited 2.4% efficiency, also predicted a maximum efficiency of amorphous Si solar cells to be 14-15%, and were followed by several decades of incremental improvement by many different groups until the current maximum of around 12.5% (indicated by green open circles in Figure 1-1). After silicon, the first of other thin-film materials and technologies such as GaAs [8], CdTe [9], and CIGS [10] have also launched their own trends of upward efficiency improvements. Among all of the PV technologies available today, the best efficiencies have come from thin-film III-V semiconductor materials, multijunction cells. Emerging, low-cost PV technologies include dye-sensitized cells [11] and organic solar cells [12].
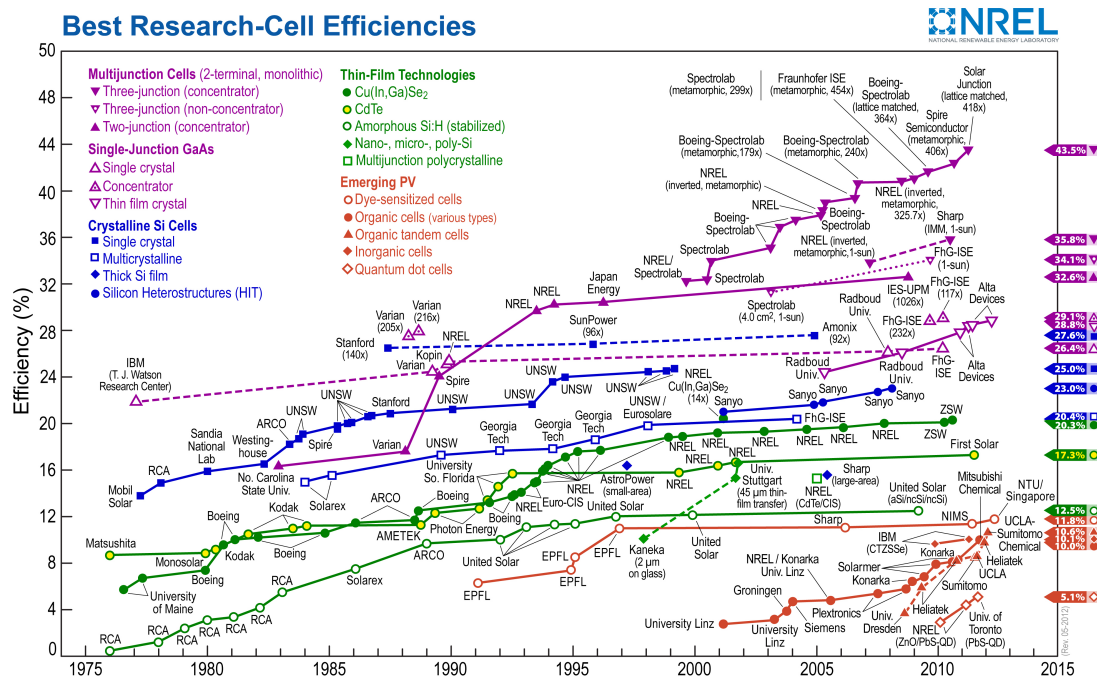
Figure 1-1   Best Research-Cell Efficiencies to date from NREL (National Renewable Energy Laboratory) [6].

Among the different improvements made by the different solar cell technologies in Figure 1-1, there is also a significant efficiency improving technology called the "concentrator" which is a PV solar cell with an externally implemented concentrating lens to multiply the solar power incident on the cell, illustrated in Figure 1-2. Thus the number in parentheses, for example, (140x), refers to the concentration of sunlight on the cell. The output power usually increases more than one-to-one with the amount of concentrated solar power in a concentrator system because of the reduction of entropy due to high input power, thus increasing the efficiency of the cell.

concentrator

n suns intensity

1 sun intensity

solar cell

solar cell

Without concentrator
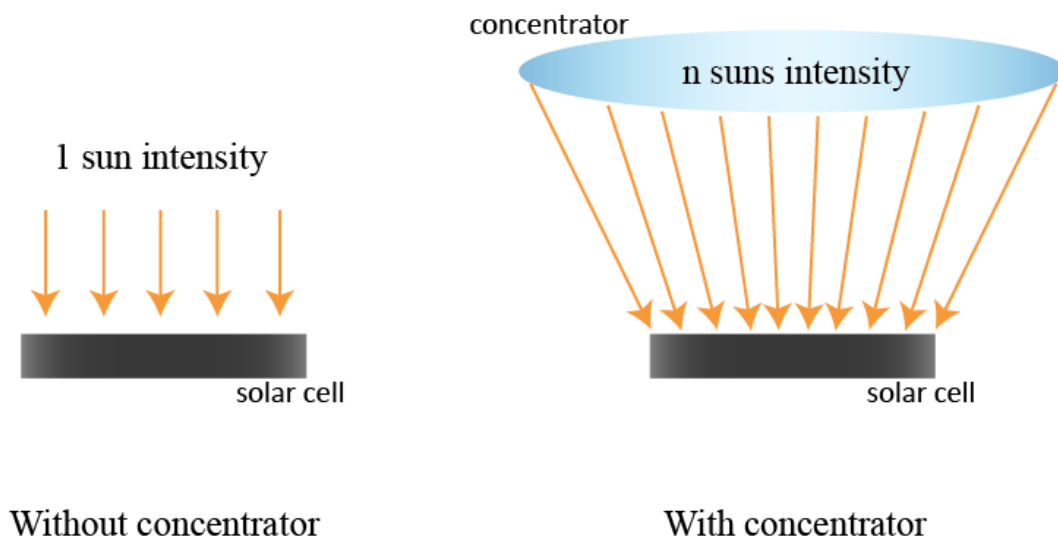
With concentrator

Figure 1-2   Physical layout of PV solar cell with and without concentrator system. Without concentrator, solar cell is illuminated with power from one sun. With a concentrator (depicted here as a single optical lens, but may also be a system with reflectors and lenses), the solar cell is illuminated with the power of n suns, n being the number of suns concentrated into the absorbing area of same size.

Some of the highest efficiencies in Figure 1-1 have been achieved with concentrator technology, but there are some challenges to it as well.   First, concentration of sunlight increases the heating of the solar cell, which could shorten the life of the device if not sufficiently cooled. Second, adding passive concentrating elements such as lenses or reflectors, which take up a significant amount of physical space and add to the complexity and cost of the system, may or may not in the end be as economical as having a larger area solar cell.

1.3   Overview of the dissertation

This dissertation addresses the solar cell efficiency improvement in the way that is not attempting to incrementally improve on previous technologies but to explore two new technologies that can potentially revolutionize solar energy harvesting. In Chapter 2 details the physics of solar cells and how efficiency is measured. Chapters 3 and 4, divided into theory and experiment, describe the intrastep quantum well solar cell (IQWSC), where quantum wells with an intrastep are implemented in a typical PV solar cell absorbing region in order to increase the efficiency by increasing absorption and current. Chapters 5 and 6, also divided into theory and experiment, describe the solar spectral condenser, a completely new kind of solar energy device that transforms the sun's broad spectrum light into semi-coherent, narrow bandwidth light that can be transported efficiently via optical fibers. Instead of converting solar energy into electricity and then transporting it, the solar spectral condenser's output can be transported as narrow spectral light for short distances and then converted into whatever type of energy (electricity, heat, or light) later. By allowing an alternative energy conversion and transport system, this new solar spectral concenrator technology, which has a patent pending, could be used to change the entire landscape of energy, giving engineers an additional degree of freedom when solving the problem of power matching individual solar cells to the grid.

1.4   References

[1]   http://www.nature.com/news/2008/080813/full/454816a.html

[2]   http://www.nature.com/nature/journal/v454/n7206/full/454805a.html

[3]   http://files.epia.org/files/Global-Market-Outlook-2016.pdf

[4]   http://www.nrel.gov/analysis/pdfs/51680.pdf

[5]   D. M. Chapin, C. S. Fuller, and G. L. Pearson, "A New Silicon *p-n* Junction Photocell for Converting Solar Radiation into Electrical Power," J. Appl. Phys., Vol. 25, No. 5, p. 676 (1954).

[6]   http://www.nrel.gov/ncpv/images/efficiency_chart.jpg

[7]   D. E. Carlson and C. R. Wronski, "Amorphous silicon solar cell," Appl. Phys. Lett., Vol. 28, No. 11, p. 671 (1976).

[8]   J. M. Woodall and H. J. Hovel, "An isothermal etchback-regrowth method for high-efficiency $Ga_{1-x}Al_xAs$-GaAs solar cells," Appl. Phys. Lett., Vol. 30, No. 9, p. 492 (1977).

[9]   N. Nakayama, H. Matsumoto, K. Yamaguchi, S. Ikegami and Y. Hioki, "Ceramic Thin Film CdTe Solar Cell," Jpn. J. Appl. Phys., Vol. 15, p. 2281 (1976).

[10]   L. L. Kazmerski, F. R. White, and G. K. Morgan, "Thin-film $CuInSe_2$/CdS heterojunction solar cells," Appl. Phys. Lett. Vol. 29, No. 4, p. 268 (1976).

[11]   B. O'Regan and M. Grätzel, "A low-cost, high-efficiency solar cell based on dye-sensitized colloidal TiO_2 films," Nature, Vol. 353, p. 737 (1991).

[12]   S. E. Shaheen, et al., "2.5% efficient organic plastic solar cells," Appl. Phys. Lett., Vol. 78, No. 6, p. 841 (2001).

Chapter 2

Efficiency of Solar Cells

2.1   Introduction

In order for solar cells to be competitive in the energy industry, they must be as efficient as possible. Efficiency can be divided into two subcategories: extrinsic and intrinsic. Extrinsic efficiency depends on factors such as effectiveness of anti-reflective coatings, the geometry of metal contacts, the external circuit, etc. Intrinsic efficiency depends on the material quality and electronic structure of the cell.

This chapter discusses the basic physics of solar cells and summarizes some of the approaches that have been explored to improve the efficiency of solar cells. Specifically, the maximum efficiency of a single-junction, single material cell is discussed. First, the calculation of the maximum efficiency of an ideal solar cell is discussed. Next, the physics of a *p-n* junction solar cell is discussed, the circuit model of solar cells is outlined in detail, the figures of merit, that is, maximum power, fill factor, and efficiency, are described, and the parasitic resistances modeled by the solar cell circuit model are discussed.

2.2   Maximum efficiency of an ideal solar cell

In this section the analysis for the maximum efficiency of an ideal solar cell is summarized. The efficiency, defined as the ratio of output to input power, is the most important figure of merit of the device. The input power is the total power from sunlight incident on the device area. The standard for the input is the American Society for Testing Materials (ASTM) G173-03 Reference Spectra, AM0, AM1.5g, and AM1.5d, shown in Figure 2-1.
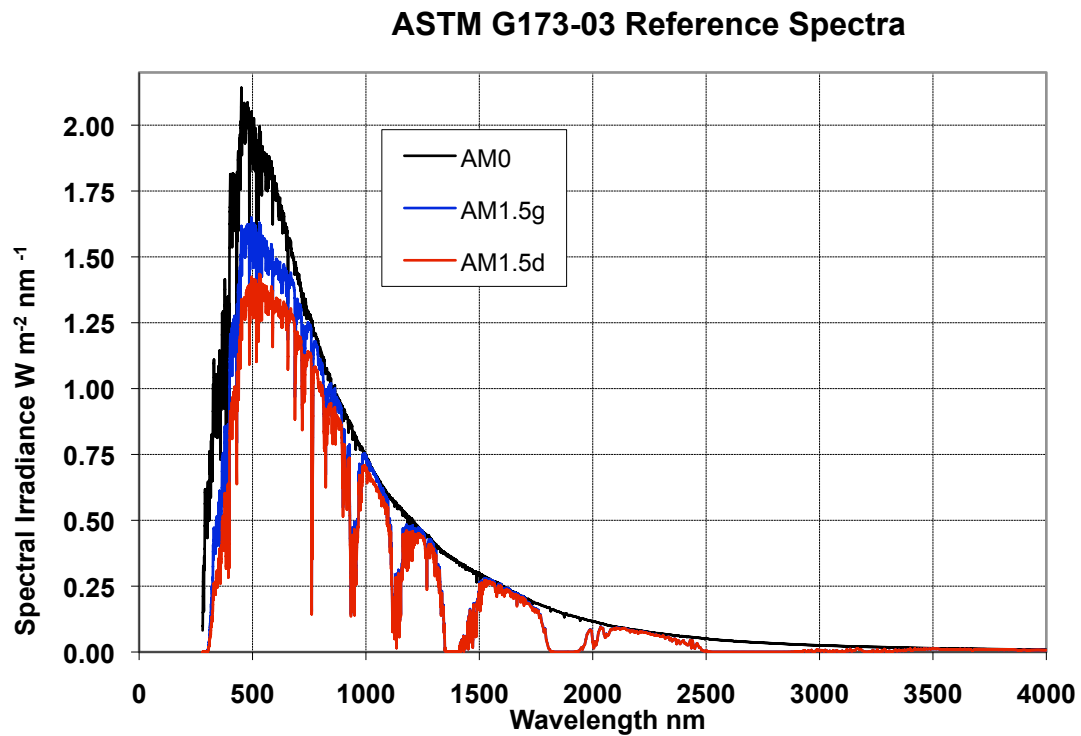
Figure 2-1   AM0, AM1.5g, and AM1.5d solar spectra from ASTM [1].

The solar spectrum depends on the atmosphere the light travels through prior to being measured. AM0, with a total power integrated over the whole spectrum of 1348W/m^2, refers to the solar spectrum seen in the space above earth's atmosphere, where the 0 means zero atmospheres. AM1.5, which refers to the solar spectrum at the solar zenith angle 48.2^o (and thus 1.5 atmospheres), is widely used for the standard solar cell measurements. AM1.5g is the global solar spectrum including direct, diffuse, and reflected light, with a total power of 1000W/m^2. AM1.5d, with a total power of 900W/m^2, is the direct solar radiation spectrum [2].

The solar spectrum AM1.5g in Figure 2-1, in W/m^2 per nm wavelength, can be expressed in eV/s/m^2 per nm wavelength for every increment of nm wavelength using Eq. 2-1. Then another conversion to number of photons/s/m^2 can be done using Eq. 2-2, which gives the energy of one photon in eV of a given wavelength. The AM1.5g solar spectrum in S.I. intensity, or W/m^2, per nm can be converted to photon flux, or $dn_{ph}/d\lambda$ in photons/s/m^2 per nm, as shown in Figure 2-2.

$$1W = 1\frac{J}{s} = 6.24 \times 10^{18}\frac{eV}{s} \qquad \text{Eq. 2-1}$$

$$E_{photon}(eV) = \frac{1240eV \cdot nm}{\lambda(nm)} \qquad \text{Eq. 2-2}$$
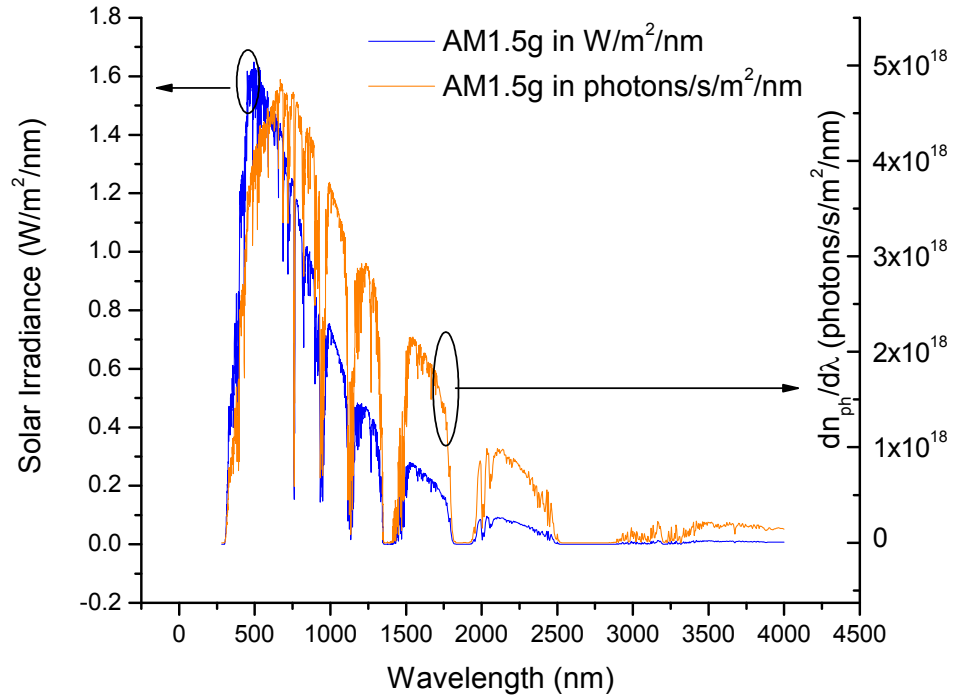
Figure 2-2   Solar spectrum in intensity and in photon flux. The left axis, which corresponds to the blue curve, is the same as the AM1.5g spectrum in Figure 2-1, the solar irradiance or intensity in W/m^2 per nm. The right axis corresponds to the orange curve, which is the photon flux per wavelength derived from the blue curve for every increment of wavelength in nm using Eqs. 2-1 and 2-2.

Assuming a material that is completely opaque for photons with energy equal to or larger than its bandgap, and completely transparent for photons with energy less than its bandgap (such a material can be realized by making it very thick), then the number of photons absorbed by this material can be found using Figure 2-2 by integrating the number of photons/s/m^2 per nm wavelength with respect to nm wavelength from zero nm wavelength to the material bandgap energy equivalent wavelength. Then the number of photons absorbed per second can be multiplied by

the work done per photon to get the power out per unit area. The efficiency for this material is then the power out divided by the power in. This calculation can be done for every bandgap energy, and plotted versus bandgap energy. This describes how to find the number of solar photons absorbed by a given material and thus possibly converting to electrical energy, essentially a brute-force method for calculating the efficiency of a solar cell.

This method, called the detailed balance limit for solar cell efficiency (using a blackbody radiation source instead of the solar spectrum, since the standard solar spectrum was not measured until 1977, reported in ERDA/NASA/1022-77/16), was developed by Shockley and Queisser in 1961 [3]. Shockley and Queisser integrated the number of photons absorbed by an ideal, single-junction, single-bandgap solar cell modeled by a blackbody sphere at 300°K surrounded by a spherical 6000°K blackbody source and came up with a curve of the ultimate efficiency $u(E_g)$, that is, the efficiency of a solar cell with bandgap E_g if "Each photon with energy greater than hv_g produces one electronic charge q at a voltage of $V_g=hv_g/q$," and no recombination (radiative or non-radiative) occurred. Then, the actual detailed balance limit was found by a reducing factor f, which may account in detail for the solar cell geometry (planar cell with normal incidence from the source, instead of spherical), radiative recombination, and other losses so that efficiency $\eta(E_g)=f \times u(E_g)$. The result using the AM1.5g solar spectrum, plotted in Figure 2-3, is that the maximum efficiency for a solar cell is about 31%, if the material had a bandgap of approximately 1.1-1.3eV. This efficiency has since been a rule-of-thumb for solar cells.

Also pictured in Figure 2-3 is the AM1.5g spectrum $dn_{ph}/d(hv)$ in photons/s/cm^2 per eV, which is found using $dn_{ph}/d\lambda$ in Figure 2-2 and the conversion,

$$\frac{dn_{ph}}{d(hv)} = \frac{dn_{ph}}{d\lambda} \cdot \frac{d\lambda}{d(hv)} \qquad \text{Eq. 2-3}$$

then plotting against photon energy hv. The AM1.5g spectrum in this form is useful for visualizing the number of photons from the solar spectrum that can be absorbed by a material with bandgap E_g as the area under the curve from energy E_g to infinity.
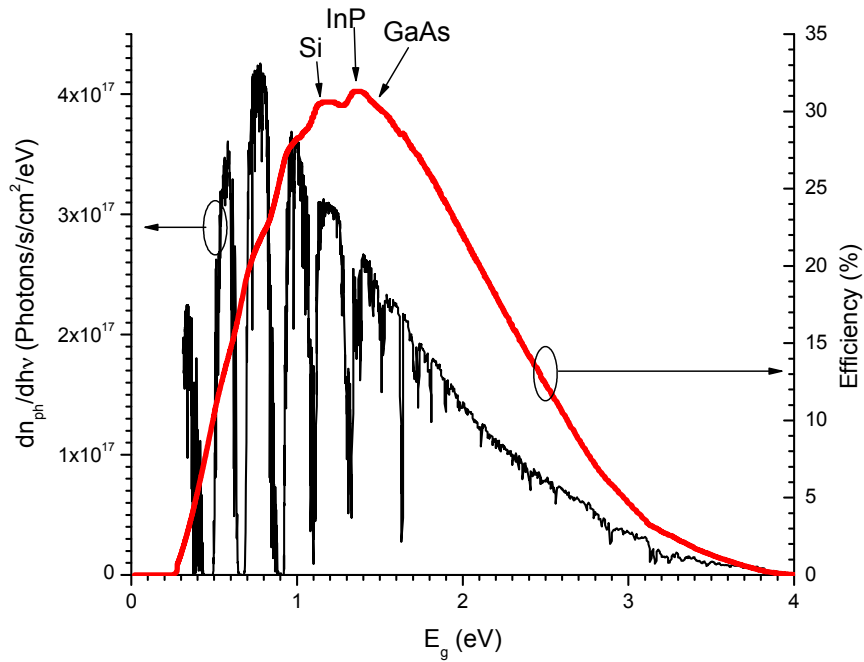
Figure 2-3   Efficiency versus bandgap for single-junction ideal solar cells. Also pictured: AM1.5g solar spectrum in photon flux per photon energy $dn_{ph}/d(hv)$. After [3, 4].

Almost two decades after Shockley and Queisser, C.H. Henry, in 1980, then came up with a graphical way to analyze the solar cell maximum efficiency using the graph of the number of photons/s/cm^2 n_{ph} absorbed by a material with bandgap E_g, found by integrating the spectrum in Figure 2-3 from E_g to infinity,

$$n_{ph}(E_g) = \int_{E_g}^{\infty} \frac{dn_{ph}}{dh\nu} dh\nu \qquad\qquad \text{Eq. 2-4}$$

shown in Figure 2-4 [4]. In Henry's analysis, the total power per area incident on the solar cell is represented by the area under the red (outer) curve, which is the integral of n_{ph} with respect to E_g, converting each photon/s back to units of power. The ideal solar cell has three losses: (1) photons with energy greater than the bandgap of the solar cell produce electron-hole pairs which immediately thermalize and drop to the energy of the bandgap, represented by the area filled with vertical lines, (2) photons with energy less than the bandgap of the solar cell pass through without being absorbed, represented by the area filled with horizontal lines, and (3) electron-hole pairs generated in the solar cell can also radiatively recombine, creating a steady state number of photons to emerge from the cell instead of being converted into electrical current, represented by the area with diagonal hash lines, which is bounded by the curve W, the average work done by each absorbed photon, which is less than the bandgap energy E_g of the solar cell (more details can be found in [4]). The maximum power output from a solar cell with bandgap E_g is then $n(E_g) \times W$, and the efficiency η is the ratio between $n(E_g) \times W$ and the total area under the red (outer) curve.
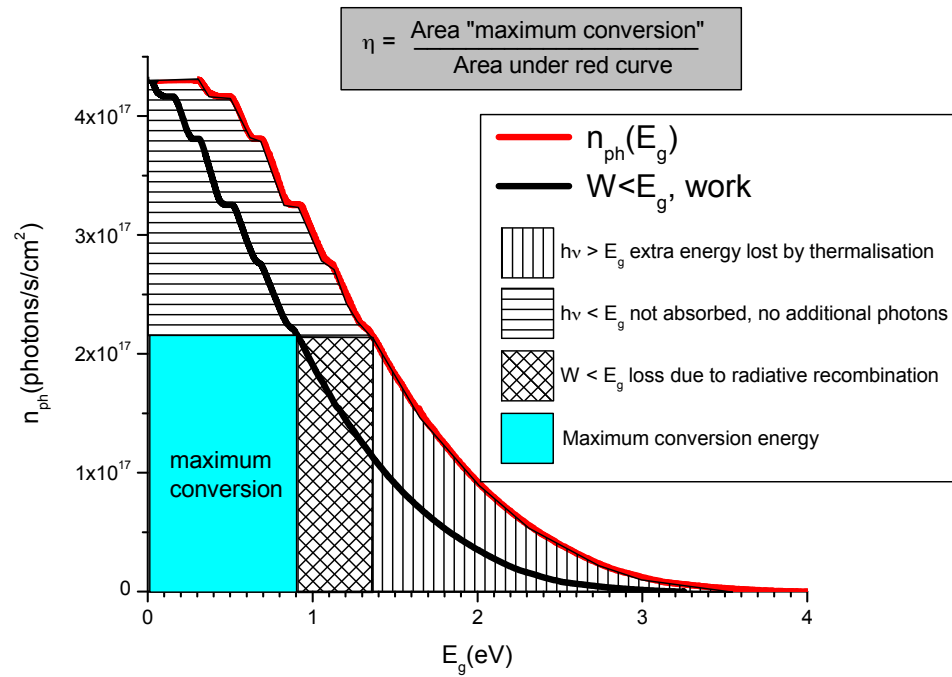
Figure 2-4   Graphical analysis of single-bandgap, single-junction ideal solar cell efficiency [4].

In addition to predicting the efficiency of a solar cell with one bandgap, CH Henry's method can also calculate the efficiency of multi-junction or tandem solar cells, which have two or more *p-n* junction PV cells in series with tunnel junctions in between so that the top-most cell collects photons of higher energy and the bottom-most cell collects photons of lowest energy, so that more of the solar spectrum is absorbed, resulting in higher photocurrent. However, in this configuration, since the cells are connected in series, careful design is required so that the currents in each cell match, because the total current is limited by the current source of lowest current.

2.3   Physics of a solar cell

This section describes the basic working principles of an ideal solar cell and its electrical circuit model, introduces the figures of merit of measured solar cells, and discusses the main non-idealities that could affect the solar cell's efficiency.

2.3.1   Solar cell energy band diagrams: dark, open-circuit, and short-circuit

Regardless of the materials the solar cell is made of or its dimensions, the most basic physical structure of a solar cell consists of a *p-n* junction (or a *p-i-n* junction), which naturally has a built-in electric field, and has some area which can be exposed to light. This *p-n* junction is then connected to the external circuit which could simply be represented by a resistive load. A *p-n* junction in equilibrium has a built-in voltage due to the electric field E induced by the space-charge region around the metallurgical junction between the *p* and *n* sides. The diffusion and drift currents are at equilibrium (thus net current is zero), and the Fermi level throughout the structure is flat.
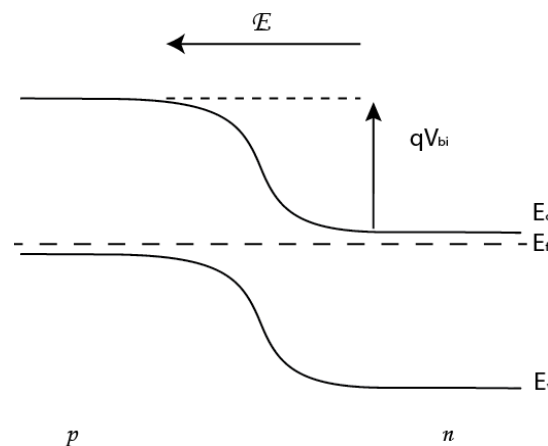
Figure 2-5. Solar cell p-n junction in the dark at thermal equilibrium.

The *p-n* junction illuminated with light is no longer in equilibrium, because electron-hole pairs are generated, as in Figure 2-6. In steady-state the excess electrons drift along the electric field to go towards the *n*-side and the excess holes go towards the *p*-side so that the Fermi level E_f separates into two quasi-Fermi levels, E_{fp} and E_{fn}. If the illuminated *p-n* junction is not connected to anything, it is in open-circuit configuration, the photogenerated electrons and holes cannot complete a circuit, then the excess electrons on the n-side and the excess holes on the *p*-side create an electric field in the opposite direction as the built-in field. This results in an open-circuit voltage V_{oc} which causes the forward bias diffusion current of the *p-n* junction exactly counteracting the drift current from the photogeneration, so that there is no net current. If the light were to be removed from this configuration, then the photogenerated current would be instantaneously cut off, allowing a momentary diffusion current to flow until the excess electrons and holes previously generated fully recombine until the *p-n* junction comes to equilibrium (i.e., E_{fn} and E_{fp} return to E_f) as in Figure 2-5.
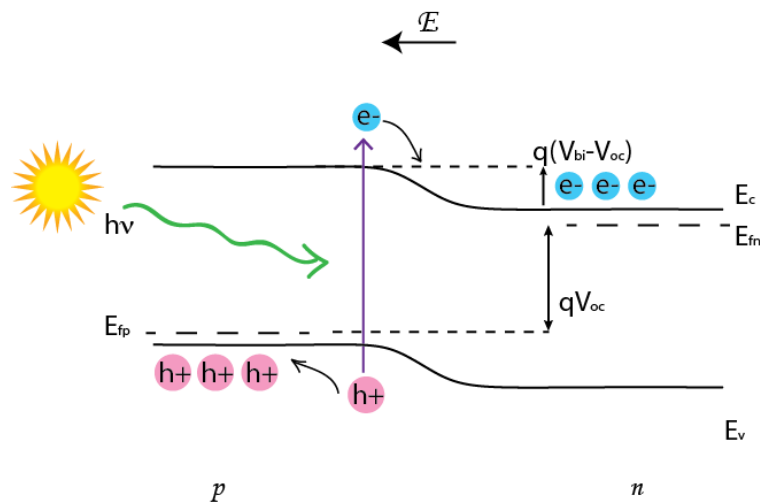
Figure 2-6.   Solar cell energy band diagram in open-circuit.

If the illuminated *p-n* junction were to be connected in short-circuit, then the photogenerated electrons and holes are free to move and complete the circuit, resulting in a short-circuit current I_{sc}. In short circuit, the quasi-Fermi level on the far *p* side would line up with the quasi-Fermi level on the far *n* side, bending the conduction band and valence band energies back to how it looked in the dark (i.e., the built-in voltage V_{bi} is the same as in the dark), except now the photogenerated electrons make their way around the short circuit and recombine with the holes at the other end.
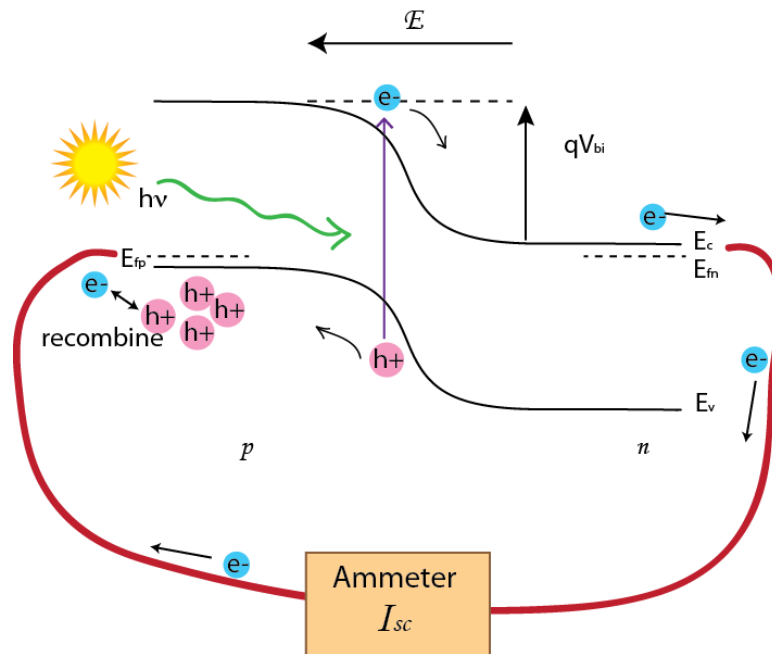
Figure 2-7.   Solar cell energy band diagram in short-circuit.

The above descriptions of the energy band diagrams of solar cells can also be applied to *p-i-n* structures as well. In general, photons can generate electron-hole pairs in the *p, i,* and *n* regions, but whether or not the generated carriers contribute to the

current delivered to the external circuit depends on the diffusion lengths of the minority carriers. The carriers generated in the i-region have the best chance of contributing to the current, but only the minority carriers of the n and p regions generated within the diffusion length of the depletion region add to the current. The diffusion length for electrons and holes depend on doping, and the depletion region thickness depends on doping and bias. Therefore, for simplicity, it is often assumed for structures with highly doped n and p regions that the absorption region is essentially equal to the thickness of the i-layer. For p-n junctions, the absorption region would be the depletion region thickness, which depends on the bias voltage.

2.3.2   Equivalent circuit model of a solar cell

In the above subsection the illuminated solar cell in open-circuit and short-circuit, prior to connecting to an external load, was discussed. In this subsection the equivalent circuit model of a solar cell, including the presence of a load, is presented. The current versus voltage (I-V) characteristic of an ideal solar cell and the power delivered to the load are described. The non-idealities, namely, parasitic resistances, which can be added to the circuit model, are discussed later in section 2.3.4.

No $P=I{\times}V$ power is generated when the solar cell is either open-circuit or short circuit even though it is illuminated , because one has zero current and the other has zero voltage. However, when a resistive load is connected to the illuminated solar cell, power can be drawn from the cell. In order to understand this, it is necessary to

separate the solar cell, a *p-n* junction diode under illumination, into two circuit elements in parallel with each other as represented by the equivalent circuit shown in Figure 2-8: (1) a diode without any illumination and (2) a current source I_L flowing in "reverse" of the diode (i.e., drifting with the E-field), where the magnitude of I_L depends on the light intensity.
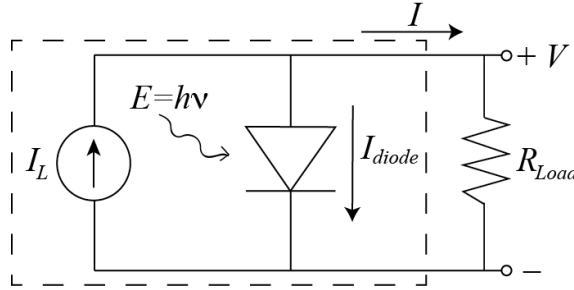
Figure 2-8   Equivalent circuit of ideal solar cell.   Elements inside the dotted rectangle represent what is inside the solar cell.

When R_{Load} approaches infinity, all of I_L flows through the diode, consistent with the open-circuit configuration. When R_{Load} approaches zero, all of I_L flows through R_{Load}, but the voltage drop on the load is then zero so the bias on the diode is also zero, consistent with the short-circuit configuration. When R_{Load} is a finite positive value, part of the current I_L flows to the resistor R_{Load} and causes a voltage drop V on R_{Load}, and at the same time V biases the diode in the "forward" direction, so that there is a current I_{diode} through the diode. The current I flowing through the load resistor in steady state can be found using Kirchhoff's Current Law (KCL),

$$I = I_{diode} - I_L = I_S(e^{\frac{qV}{kT}} - 1) - I_L$$ Eq. 2-5

where I_{diode} is the ideal diode current in the dark, I_L is the current generated by the incident photons with energy $h\nu$, I_S is the saturation current of the diode, q is the basic charge, V is the voltage drop on the load R_{Load}, kT is the thermal energy. The short-circuit current, I_{sc}, is usually very close to the photogenerated current I_L. The power $I \times V$ delivered to the load is

$$P = (I_s(e^{\frac{qV}{kT}} - 1) - I_L) \cdot V \qquad \qquad \text{Eq. 2-6}$$

The voltage drop V on R_{Load} is due to the current I, i.e., $V = I * R_{Load}$, but it in turn drives the diode current $I_{diode} = I_s(e^{qV/kT} - 1)$. If one increases V by increasing R_{Load}, I_{diode} increases, but the current I through the load decreases, because the photocurrent I_L is constant, and the total power decreases. If one decreases V by decreasing R_{Load}, then I_{diode} diminishes, and I through the load increases, but the total power decreases because of a smaller V. If I_L is fixed (i.e., the illumination intensity is fixed), then there is one R_{Load} value that would maximize the power delivered to the load.

2.3.3 Figures of merit of solar cells

The figures of merit of a solar cell can be determined by measuring its *I-V* characteristics by sweeping the bias voltage on the solar cell using a voltage source and using an ammeter to monitor the current going through the cell under illumination of a solar spectrum simulator lamp. Note that a load resistor is not connected during the *I-V* measurement of a solar cell. Rather, using the *I-V* characteristic, one can find

the matching load resistance that can yield the maximum power from this solar cell under the given illumination. From the last subsection it was discussed that the voltage drop on the load resistor (and therefore the voltage biasing the diode) depends on the resistance as well as the photogenerated current. Therefore sweeping the bias voltage in the *I-V* characterization measurement simulates sweeping the load resistance value. In Figure 2-9 two curves are the *I-V* characteristics of solar cells under illumination and without illumination. Assuming that the photogenerated current I_L is independent of the bias voltage, the illuminated *I-V* curve is the same as the dark *I-V* curve, offset by a constant I_L.
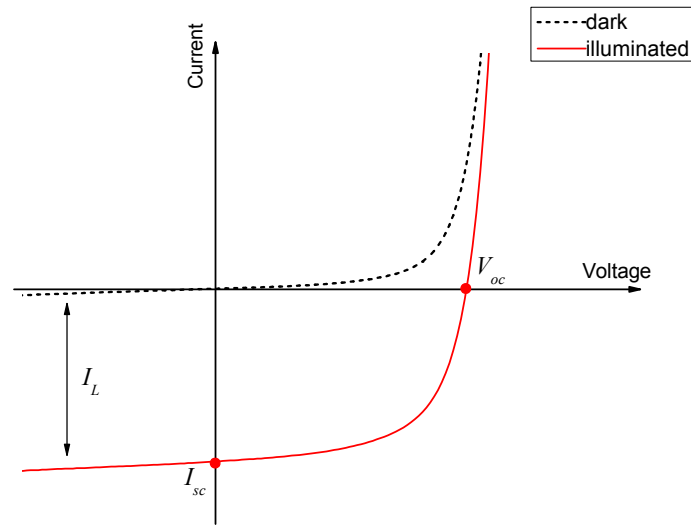
Figure 2-9   *I-V* characteristic of a solar cell. The dark *I-V* curve resembles typical diode, and the illuminated curve is similar but offset by photogenerated current I_L. As labeled, short-circuit current I_{sc} occurs when bias voltage V is zero, and open-circuit voltage when total current I is zero.

The power $P=I*V$ generated from the solar cell can be found by multiplying the current I by its corresponding bias voltage V in the *I-V* curve, and plotted also with

respect to V, as shown in Figure 2-10. It is common practice to plot the power generated from the solar cell as a positive value, so the figure actually shows $-P$.
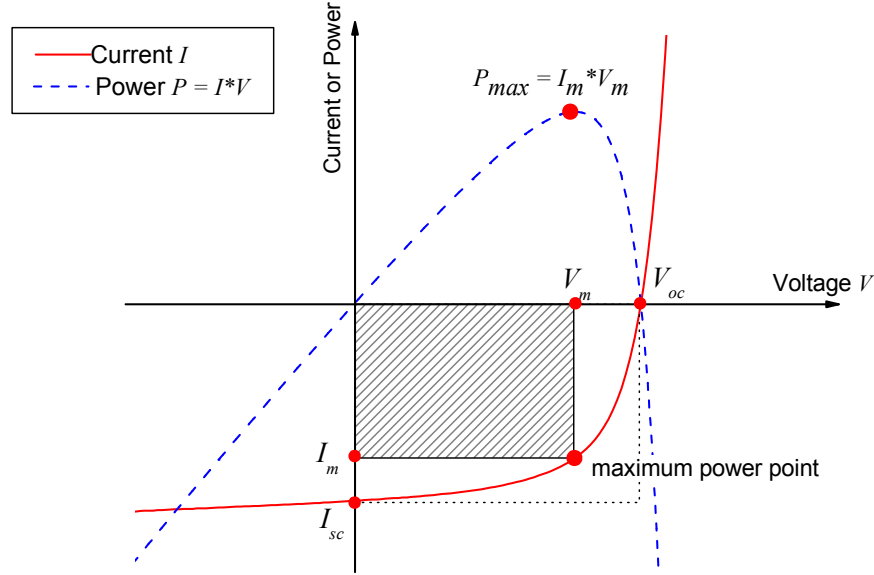
Figure 2-10   Solar cell *I-V* and *P-V* graphs showing figures of merit.

Solar cell figures of merit are highlighted in the *I-V* and *P-V* curves above: short-circuit current I_{sc}, open-circuit voltage V_{oc}, maximum power P_{max}, maximum power current I_m and maximum power voltage V_m.   The point in the *I-V* curve at which maximum power occurs is also highlighted. The area of the shaded rectangle, the largest rectangle that can fit within the *I-V* curve in the fourth quadrant, represents the maximum power. The more ideal the solar cell, the closer P_{max} would be to $I_{sc}*V_{oc}$, characterized by the figure of merit, fill factor *FF*:

$$FF = \frac{I_m \cdot V_m}{I_{sc} \cdot V_{oc}}$$

Eq. 2-7

The fill factor is maximized when the solar cell behaves as an ideal rectifying diode, which can be seen by measuring the dark *I-V* characteristics. There is also a characteristic resistance $R_{char}=V_m/I_m$, which is the ideal R_{Load} that draws the maximum power from the solar cell for a given illumination intensity and spectrum. That is to say, maximum power is only achieved when $R_{Load}=R_{char}$.

The efficiency of a solar cell is defined as

$$\eta = \frac{P_{max}}{P_{in}} = \frac{I_m V_m}{P_{solar}}$$

Eq. 2-8

The efficiency is highly dependent on the material, physical, and electronic structure of the cell. In a single bandgap material, single junction cell, and with one sun incident, in the most ideal case, the maximum possible efficiency is 31% with a bandgap of about 1.1-1.3eV. This ideal case considers that there is no reflection, the device is completely opaque for photons with energy greater than the bandgap and perfectly transparent for photons with energy less than the bandgap. In this case, each photon absorbed would produce one electron-hole pair, which are swept to either side of the junction due to the electric field, determined by the difference between the built-in voltage and the voltage drop across the device, which is the current that flows through a solar cell. The power output by the solar cell is the current times the voltage drop on the cell.

2.3.4 Parasitic resistances of solar cells

In this section the parasitic resistances and their effect on the overall efficiency, are discussed. A model of a realistic solar cell with parasitic resistances is shown in Figure 2-11, where R_{Shunt} is the parasitic parallel or shunt resistance, R_{Series} is the parasitic series resistance, and R_{load} is the load resistance. Ideally, if $R_{Series} = 0$ and $R_{Shunt} = \infty$, Figure 2-11 would be identical to Figure 2-8.
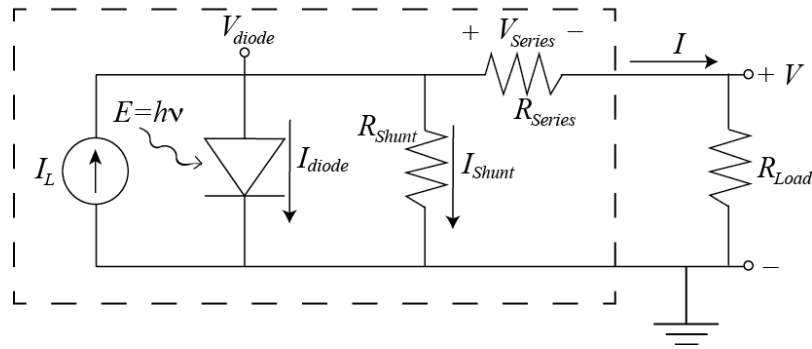
Figure 2-11   Equivalent circuit model of a solar cell with parasitic resistances. The elements within the dotted rectangle represent the solar cell. It is obvious that $V_{diode}=V_{Series}+V$, $V_{Series} = I*R_{Series}$, and $I_{Shunt}=V_{diode}/R_{Shunt}$.

Using KCL on Figure 2-11, the current I through the load R_{Load} is

$$I = I_L - I_S(e^{q\frac{V+I\cdot R_{Series}}{nkT}} - 1) - \frac{V+I\cdot R_{Series}}{R_{Shunt}}$$ Eqn. 2-9

where I_L is the photogenerated current, I_S is the saturation current, q is the fundamental charge, V is the voltage drop on the load, n is the ideality factor, and kT is the thermal energy. To better understand parasitic resistances and their effect on the solar cell, the series and shunt resistances can be examined separately.

The series resistance can be caused by poor Ohmic contacts at the semiconductor-metal junction or poor current spreading in the semiconductor area. These can be a result of poor design or fabrication of the device. In the case of R_{Series} alone (assume R_{Shunt} is very large), in Figure 2-11, the voltage produced by the solar cell V_{diode} is now shared between R_{Series} and R_{Load} so that the voltage V seen by the load is reduced by V_{Series}. In the presence of R_{Series} in order for I to remain the same as without R_{Series}, R_{Load} must be reduced by R_{Series} so that the sum of the resistances equal the ideal R_{Load}. Also, in the presence of R_{Series}, the R_{Load} corresponding to the maximum power point would not be the same as the ideal R_{Load}. The effect of series resistance is shown in Figure 2-12.
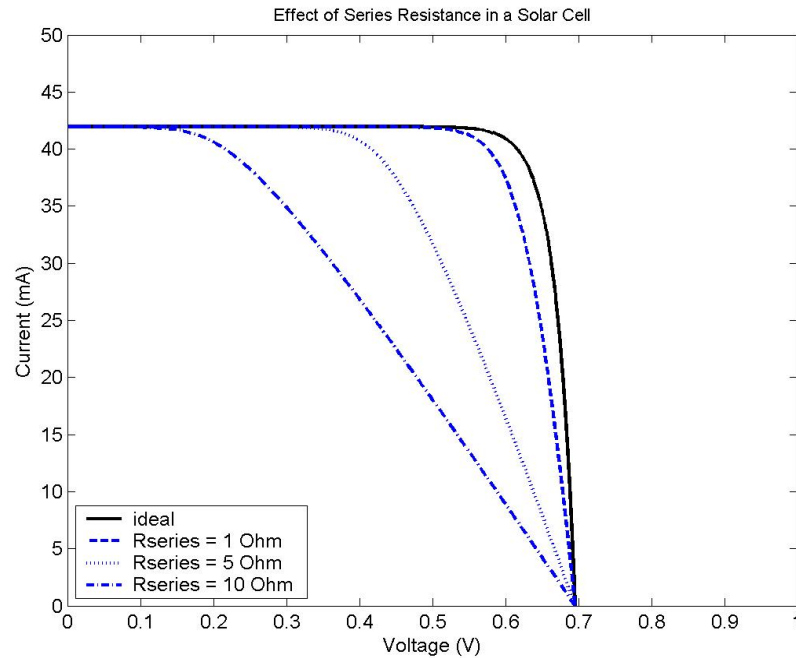
Figure 2-12   Effect of series resistance on a solar cell. Calculated using Eqn. 2-9, assuming solar cell area of 1cm^2, photogenerated current density of 42mA/cm^2, reverse saturation current density of 1E-10mA/cm^2, and thermal energy kT of 26meV.

Shunt resistance may be due to dislocations in the semiconductor material that form undesired current paths, especially at the *p-n* junction and its interface with the surrounding material. This can be due to poor material quality, lattice mismatch, and different material growth conditions. In the case of R_{Shunt} alone (assume R_{Series} is negligibly small), in Figure 2-13, the current produced by the solar cell I_L now has three paths: through the diode, R_{Shunt}, and R_{Load} so that the current I through the load is reduced by I_{Shunt}. In the presence of R_{Shunt} in order for V to remain the same as without R_{Shunt}, the resistance of the new R_{Load} in parallel with R_{Shunt} must equal the ideal R_{Load}. Also, in the presence of R_{Shunt}, the R_{Load} corresponding to the maximum power point would not be the same as the ideal R_{Load}. The effect of shunt resistance is shown in Figure 2-13.
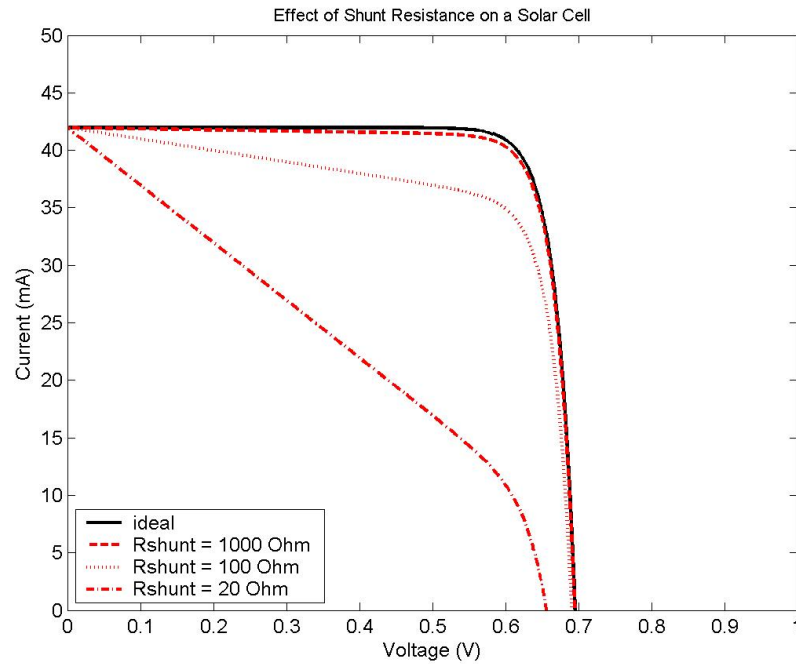
Figure 2-13   Effect of shunt resistance on a solar cell. Calculated using Eqn. 2-9, assuming solar cell area of 1cm^2, photogenerated current density of 42mA/cm^2, reverse saturation current density of 1E-10mA/cm^2, and thermal energy kT of 26meV.

Most practical solar cells have a combination of series and shunt resistances, which together can further reduce the efficiency. Figure 2-14 illustrate the effect of both parasitic resistances compared to an ideal solar cell and solar cells with only one type of parasitic resistance. In most cases (i.e., a first-order approximation for solar cells with parasitic resistances that are not too severe), as is shown in Figure 2-14, the inverse slope of the *I-V* curve near *V*=0 is equal to R_{Shunt} and the inverse slope of the *I-V* curve near *I*=0 is equal to the R_{Series}.
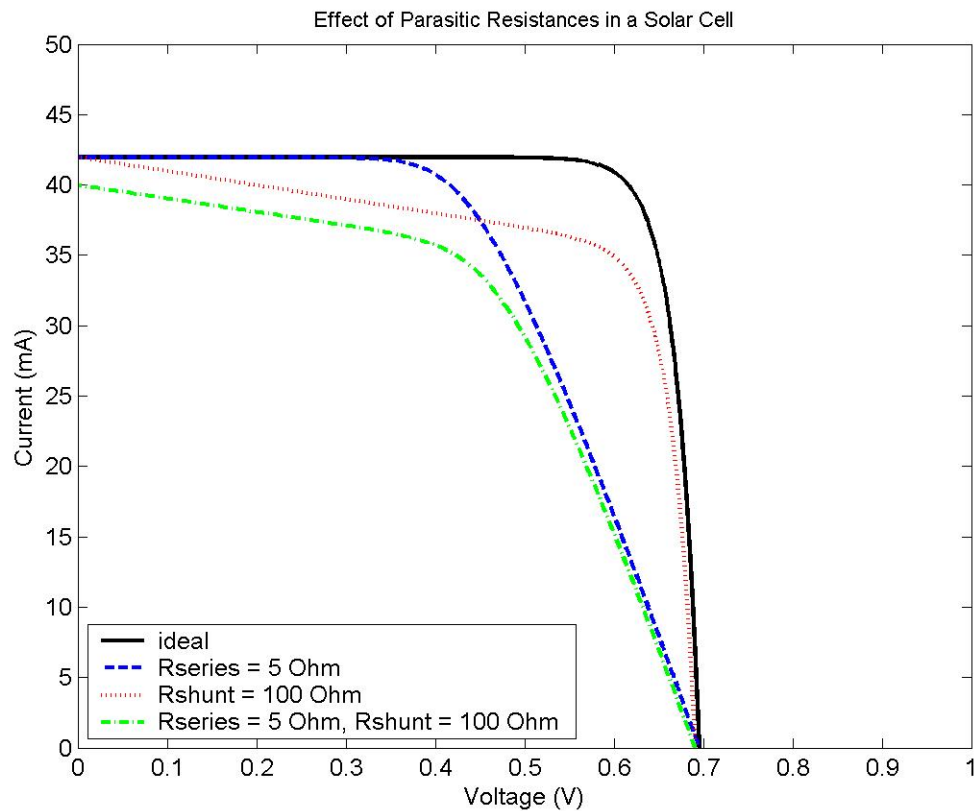
Figure 2-14   Effect of parasitic resistances. Calculated using Eqn. 2-9, assuming solar cell area of 1cm^2, photogenerated current density of 42mA/cm^2, reverse saturation current density of 1E-10mA/cm^2, and thermal energy *kT* of 26meV.

In addition to reducing the efficiency and maximum power of a solar cell, another severe effect of parasitc resistances is that they add to the heating up of the solar cell. The power dissipated in the cell due to parasitic resistances is I^2R, where I here refers to the current through the respective parasitic resistance R.

2.4   Summary of basic solar cell principles

This chapter covered the efficiency of ideal solar cells, the basic physics of solar cells, figures of merit associated with solar cells, and parasitic resistances of solar cells. The efficiency of a solar cell depends on the bandgap(s) of the solar cell materials. The physics of a *p-n* junction solar cell, including its operation in short-circuit and open-circuit, were discussed. A solar cell's *I-V* characteristics, measured by applying a voltage and measuring the current under a fixed illumination, determine its figures of merit, open-circuit voltage V_{oc}, short-circuit current I_{sc}, maximum power voltage V_m, maximum power current I_m, maximum power P_{max}, fill factor *FF*, characteristic resistance R_{char}, and efficiency η. Finally, the effects of parasitic resistances, R_{Series} and R_{Shunt}, were illustrated and described. The formulae, models, and definitions described in this chapter are the basis of the theories and experiments in the following chapters of this dissertation.

2.5   References

[1]   http://rredc.nrel.gov/solar/spectra/am1.5/

[2]   http://rredc.nrel.gov/solar/pubs/shining/page12_fig.html

[3]   W. Shockley and H. J. Queisser, "Detailed Balance Limit of Efficiency of *p-n* Junction Solar Cells," J. Appl. Phys., Vol. 32, No. 3, p. 510 (1961).

[4]   C. H. Henry, "Limiting efficiencies of ideal single and multiple energy gap terrestrial solar cells," J. Appl. Phys., Vol. 51, No. 8, p. 4494 (1980).

Chapter 3

Theory of Intrastep Quantum Well Solar Cells

3.1   Introduction

In the last chapter it was established that the bandgap of a material is one of the most important factors that determines whether it could make an efficient solar cell, and theoretically, for a single-bandgap, single junction PV cell the best efficiency that can be achieved is about 30% with bandgap of around 1.1eV. Si, whose bandgap is 1.1eV, has been widely used as a solar cell material not only because of its bandgap but also because of the ease of manufacturing and abundance of Si. However, Si is not the most efficient solar cell material, because it has an indirect bandgap, which means that any optical transition must also involve phonons, so the absorption coefficient of Si is low compared to a direct bandgap material. The GaAs and InP family of materials have been widely studied for solar cell applications because they are direct bandgap materials with bandgaps within the range for high power

conversion efficiency. Multi-junction or tandem PV cells made of these materials have set the records for the highest efficiencies to date. Quantum well solar cells (QWSCs) comprised of AlGaInAsP alloys have also been shown to improve the efficiency of a solar cell compared to solar cells of uniform material [1]. Detailed balance calculations of QWSCs have shown efficiencies of up to 64%, which is higher than that of 2- or 3-stack multi-junction cells [2].

3.1.1 Current-matching of multi-junction solar cells

A multi-junction solar cell consists of several layers, each of a different material and consisting of a *p-n* junction, usually with tunneling junctions in between each layer. The order of stacking the layers is to have the largest bandgap materials on top and the smallest bandgap materials at the bottom such that the shortest wavelength photons are absorbed first and the longest wavelength photons are absorbed last. This sequence reduces the amount of loss from thermalisation of electrons and holes that have been generated by photons with energy greater than the bandgap of the material.

One of the challenges of multi-junction solar cells is designing them with proper current-matching when the layers are stacked in series. Since each layer absorbs different sections of the solar spectrum, each layer also may produce a different number of electrons and holes and thus a different current contribution. Since the layers are like individual solar cells that are connected in series, the total current seen by the external circuit is limited by the layer with the lowest current.

In order to understand the current matching issue in multi-junction solar cells, it is useful to consider a simple scenario with two ideal solar cells, cell 1 and cell 2, in series under illumination with different short-circuit currents I_1 and I_2, where $I_1 > I_2$, in short-circuit, as shown in Figure 3-1. Each of the two solar cells is modeled as a current source in parallel with a diode. The total current seen by the external circuit is I, equal to the lower current I_2. Cell 1, however, still generates a current $I_1 > I_2$, so according to Kirchhoff's law, I_1-I_2 >0 must flow through cell 1's diode D_1, forward-biasing it at $V_{bias} > 0$. Since the entire circuit is shorted, there is a voltage drop of $-V_{bias}$ on cell 2, reverse-biasing D_2 (but the current is still close to zero, or at least much smaller than photocurrent, for an ideal diode in reverse). Ultimately, current mismatch causes the efficiency of the entire system to be reduced because of the power P $=V_{bias}*(I_1$-I_2) dissipated in cell 1 [3].
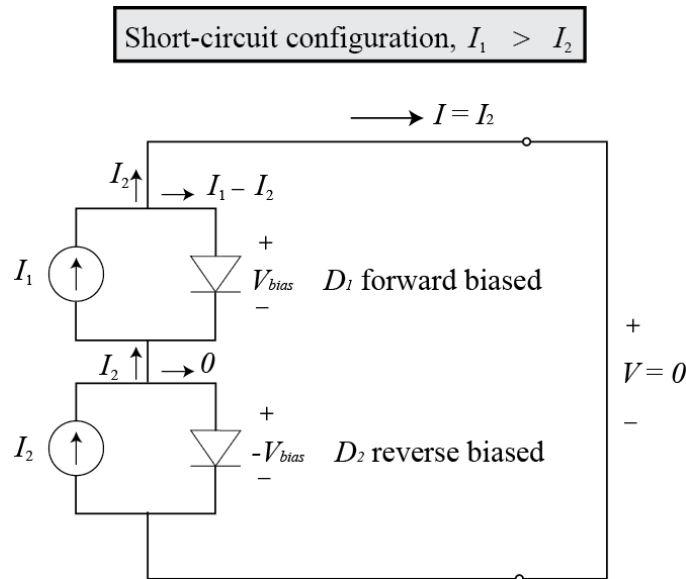
Figure 3-1   Current mismatch of multi-junction solar cells. After [3].

The current mismatch issue can be reduced if the multi-junction solar cell is well-designed. The layer thicknesses must be tailored exactly so that the absorption of each layer match, for a given solar spectrum. However, the amount of light absorbed can vary with different spectra or with different concentration of light. QWSCs are similar to multi-junction solar cells in that they can absorb more of the solar spectrum than a single-bandgap cell. In contrast, QWSCs have one *p-i-n* junction, so the current mismatch issue does not apply in the same way as for multi-junction cells.

In this chapter quantum wells (QWs) and intrastep quantum wells (IQWs) for use in the absorption region of solar cells are discussed. First, the theory of QWs in solar cells is described and the key advantages and challenges of QWSCs versus single bandgap solar cells are outlined. Then, the intrastep quantum well solar cell (IQWSC) is introduced. The theory of the effect of IQWs in solar cells is described, simulation results of IQWs and QWs are shown, and key advantages of using certain IQW structures over QWs are outlined. The simulation results from this chapter are used as a basis on which the IQWSC is designed, fabricated, and tested in the next chapter.

3.2 Quantum well solar cells

In general, QWSCs consist of a *p-i-n* structure with the *p* and *n* region having a bandgap of the host or bulk material, and the *i* region consisting of multiple quantum wells, as shown in Figure 3-2. Not only photons with energy greater than the host

material bandgap can be absorbed, but also photons matching any allowed optical transitions within the quantum well states. Energy levels inside quantum wells provide states for photons with energy less than the host material bandgap to be absorbed. These states could be, in the case of a rigid quantum well, "hard" quantum states, or, in the case of multiple quantum wells with slight variations (due to non-uniform growth or even different illumination intensities at different depths), could span a semi-continuum between $E_g{}^{host}$ and $E_g{}^{well}$. Electrons and holes inside wells escape by thermionic emission and are swept to either side of the *p-i-n* diode by the electric field. Electron-hole pairs generated by photons with energy higher than the host bandgap lose energy through thermalisation and fall to the conduction and valence energy levels before being swept by the E-field. An electron or hole passing through the *i* region could be in danger of falling back into or being captured by a well if there is an unoccupied state, but it could just as easily thermally escape again.

Figure 3-2   Quantum well solar cell energy band diagram. After [4].

There are two main advantages that a well-designed QWSC has compared to solar cells without quantum wells, illustrated in Figure 3-3. First, compared to a solar cell made of the host material alone, more of the solar spectrum can be absorbed because of the addition of quantum wells, which results in higher photocurrent [5]. Second, compared to a solar cell made of the well material alone which has lower open-circuit voltage due to its smaller bandgap, the QWSC's open-circuit voltage may be closer to that of a solar cell made entirely of the host material, which has a higher open-circuit voltage due to its larger bandgap [4, 6]. Overall, the maximum power of a QWSC can be greater than both the barrier only and well only solar cells.
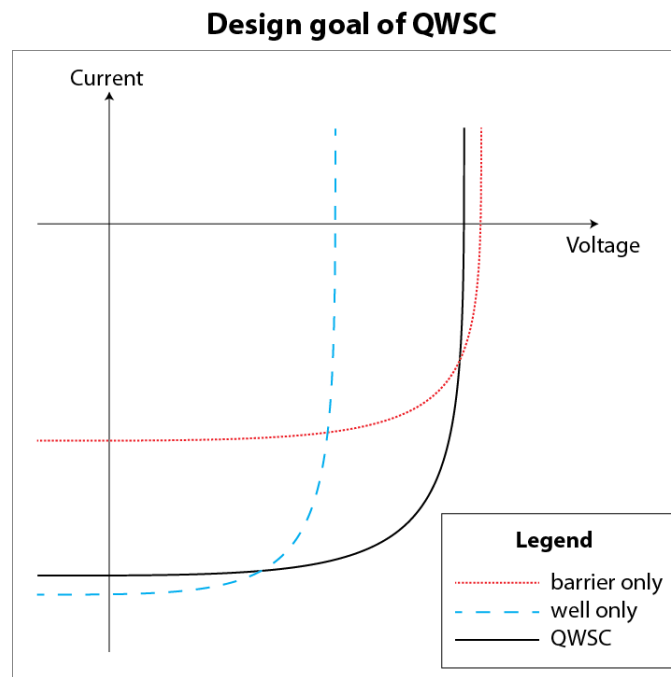
Figure 3-3   Effect of a properly designed QWSC. The QWSC is able to absorb more photons, so short-circuit current I_{sc} should increase, close to that of a solar cell with well material only. The QWSC is able to hold a higher open-circuit voltage V_{oc}, close to that of the solar cell with barrier material only.

There are also some auxiliary uses of QWs that could enhance the efficiency of QWSCs. QWSCs can be designed so that the QWs stack in phase with a distributed Bragg reflector substrate, resulting in photon recycling effect, increasing the effective length of the *i*-region seen by a photon and thus increasing absorption [7]. The *i*-region in the QWSC can also act as a waveguide for photons scattered by nanoparticles, which also increases the effective distance travelled by photons in the active region [8]. Strain-balanced QWSCs could also be used as a layer within a tandem solar cell stack, possibly reducing the strain in the overall structure [9].

Several design and growth challenges must be met in order to achieve the goal of QWSC, because the amount of power conversion efficiency enhancement due to quantum wells depends on the host material bandgap, the bandgap difference between the host and well, and non-radiative effects that are often due to poor material quality [10]. The dimensions of the *i*-region must be optimized so that it is thick enough for a significant amount of absorption in the shorter wavelengths but short enough so that the E-field that falls over the individual quantum wells is large enough for carriers inside the well to thermal escape before recombining [11]. Also, growing so many layers in the QWSC structure gives rise to greater possibility of lattice imperfections such as impurities, dislocations, and stacking faults, which could cause non-infinite shunt resistance or non-radiative recombination centers, significantly reducing the enhancement of efficiency. All of the challenges for QWSCs are also applicable to IQWSCs.

3.3 Intrastep quantum well solar cell theory

In this section intrastep quantum wells (IQWs) are introduced and compared to regular quantum wells (QWs) for the absorption layer in solar cells. For the different types of quantum wells, two main factors are considered: (1) the overlap between the electron and hole envelope wavefunctions and (2) barrier heights for electrons and holes in the wells. To determine these, the envelope wavefunctions and energy levels were calculated by the Schordinger equations based on the known energy band structure of the quantum wells, and presented graphically in this section. Finally, the implications these have on the efficiency of the solar cell are discussed.

3.3.1 Electronic structures of IQW, flipped IQW, and regular QW

An intrastep quantum well (IQW) in this study is a quantum well with two different bandgaps. Typically in the InP-lattice-matched InGaAsP, the material band structures line up as Type I heterostructures, where the conduction level for the material with smaller bandgap is lower than the one with larger bandgap, and the valence band level for the material with smaller bandgap is higher than the one with larger bandgap. In particular, for InGaAsP lattice-matched to InP, the energy band offset for the valence level is assumed to be 60% of the total energy band offset and for the conduction band it is 40%. The energy band diagram for an IQW struture is shown in Figure 3-4. Figure 3-5 shows the energy bandgap versus As molar fraction of InGaAsP lattice matched to InP.
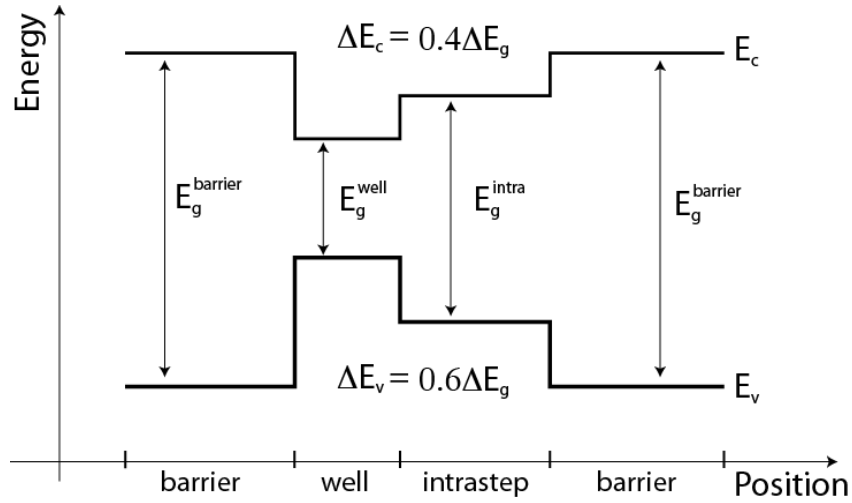
Figure 3-4   Electronic structure of IQW, flatband (no E-field). E_c and E_v are the bottom of the conduction band and the top of the valence band, respectively, for each layer. ΔE_c and ΔE_v are the band offsets for the conduction and valence levels, respectively. For this study, the barrier material is InP, and the well and intra materials are InGaAsP quaternary alloys lattice-matched to InP.
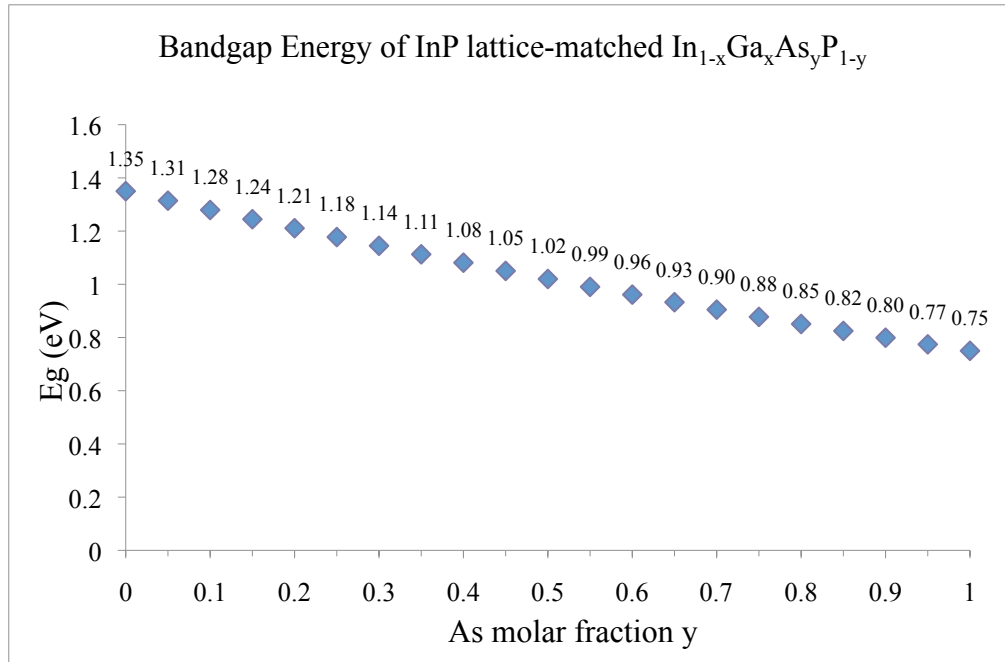
Figure 3-5   Bandgap Energy versus As molar fraction of InGaAsP lattice matched to InP, according to Vegard's Law. The bandgap energies in eV are labeled next to each point (y increment of 0.05). The left-most point (E_g=1.35eV) is InP, and the right-most point (E_g=0.75eV) is $In_{0.53}Ga_{0.47}As$. The relationship is nearly linear.

Within the QW there are two different bandgap materials as in the IQW, the energy wavefunctions of the electrons and holes can be very different from that of a regular quantum well. In a solar cell with IQWs, the overlap between the envelope wavefunctions of the electrons and holes could either increase or decrease, affecting the overall absorption of photons, and the barrier heights for the electrons and holes to travel to either the *n* or *p* sides, respectively, will also be different, affecting the total current. The above figure shows the well and intra materials of about the same thickness, but these could also be varied to tailor the overall envelope wavefunctions and energy levels. For a solar cell with IQWs, the goal is to increase the total power. In order to do so, IQWs should be designed to:

- Maximize the overlap of the electron and hole envelope wavefuctions, especially at the operating point, which is the maximum power point (at which there is a finite electric field bending the band structure).

- Minimize the barrier heights which electrons and holes in the quantum wells must overcome by thermionic emission to be collected as current.

With the above considerations, as well as the consideration that the IQWs should have dimensions that are realistic for MOCVD growth (i.e., each layer should be at least several monolayers thick in order to be realized in epitaxial growth), the IQW structure described by Figure 3-6 and Table 3-1 was chosen for investigation in this study. Note that Figure 3-6 shows one IQW of the multiple-IQWs inside of a *p-i-n*

solar cell. The IQW structure was calculated by solving the Schrodinger equation for

the eigenvalues. The values used for solving the Schrodinger equation for the IQW

structure, energy band gap E_g, conduction and valence band effective masses m_c and

m_v (both relative to mass of an electron m_o), and thickness t, are listed in Table 3-1.
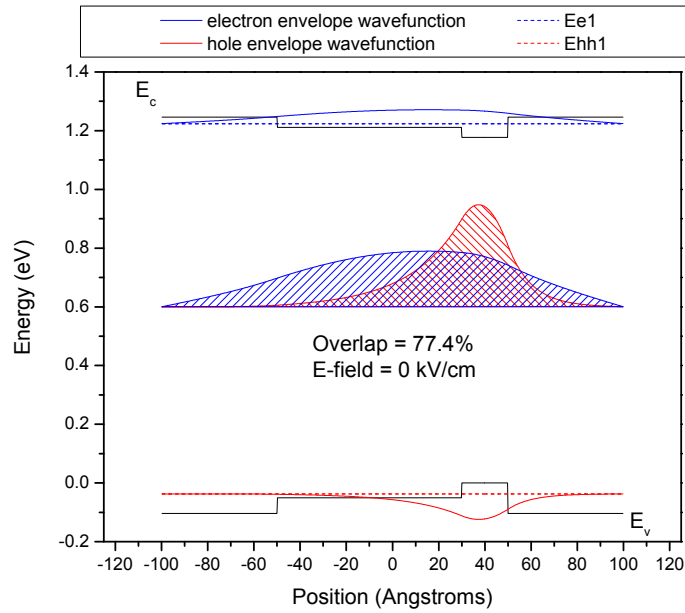
Figure 3-6   IQW structure chosen for investigation. The energy band structure is
shown with zero electric field (or flat band). Table 3-1 lists the parameters for each
material in this figure.

Table 3-1   IQW band structure parameters used for simulation

	InP	intrastep	well
E_g (eV)	1.35	1.26	1.18
m_c	0.0770	0.0744	0.0712
m_v	0.5600	0.5535	0.5471
t (Å)	--	80	20

The full IQWSC structure contains five IQWs as shown above in Figure 3-6 inside a 125nm thick *i*-region between highly doped InP *p* and *n* layers. Figures 3-7, 3-8, and 3-9 show the energy band diagram of the *p-i-n* structures at equilibrium without illumination for the IQW solar cell (IQWSC), the flipped IQWSC (that is, the position of the well and the intrastep are flipped with respect to the *p* and *n* sides), and the regular QWSC. As described in Chapter 2 Section 2.3.1, because of the *p-i-n* structure, during solar cell operation there is an electric field across the *i*-region, which is a combination of (1) the built-in potential of the *p-i-n* structure and (2) the voltage seen by the diode at the operating point, determined by the external load (which should be the maximum power point, if the load is chosen correctly). In the next two subsections the simulations of electron and hole envelope wavefunction overlap and barrier heights for different electric fields are presented.

Regular QWSC energy band diagram
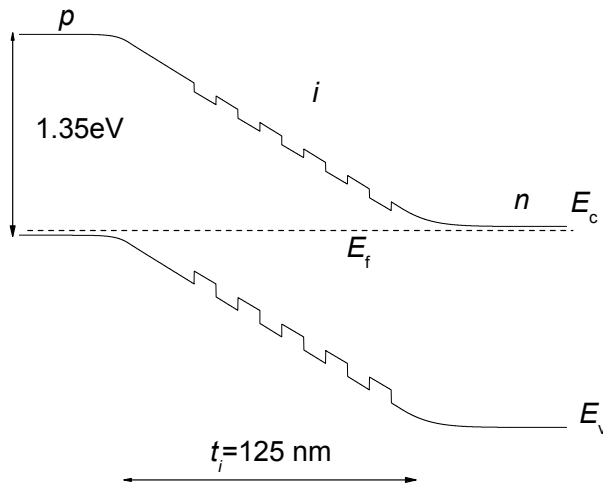
Figure 3-7   Energy band diagram of a regular QWSC.

IQWSC energy band diagram
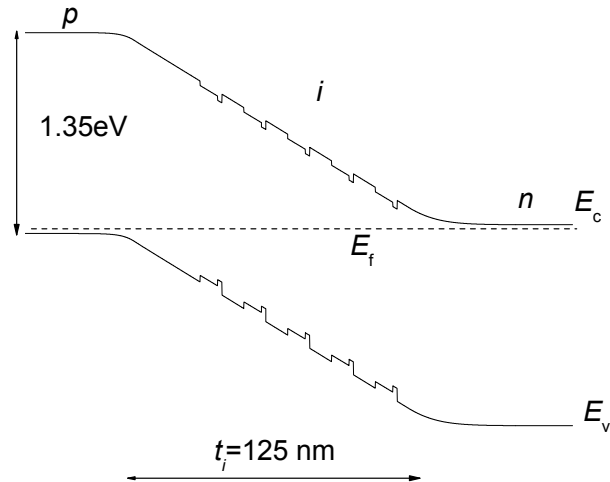
Figure 3-8   Energy band diagram of a IQWSC with intra (shallower well) facing the p-side.

flipped IQWSC energy band diagram
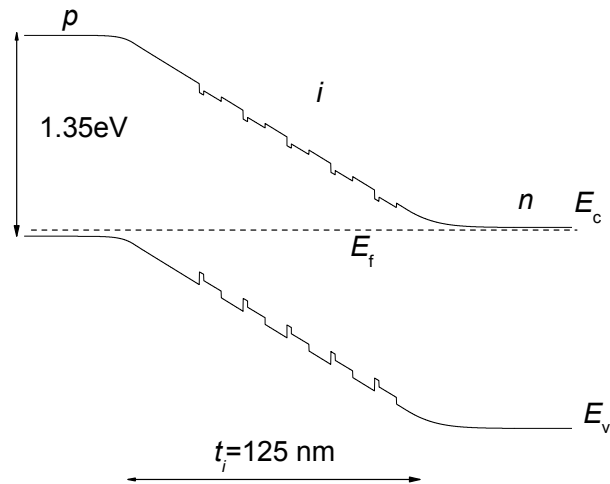
Figure 3-9   Energy band diagram of a flipped IQWSC with deeper well facing the p-side.

3.3.2   Electron and hole envelope wavefunction overlap

Since it is desirable to maximize the electron and hole envelope function overlap at the operating bias voltage point of the solar cell, in this subsection, the overlap for the three different structures, regular QW, IQW, and flipped IQW, are calculated and compared for different bias voltages to find the best structure for maximum overlap.

Since the well and intra materials are quite shallow, there is only one bound electron level, e1.   Although there may be more than one hole level, the optical transition selection rule limits transitions between levels of the same momentum only. Therefore, in the structure under investigation, only the ground heavy hole level, hh1, is considered.   The light hole level, lh1, could also be considered, but for simplicity, only the transition between hh1 and e1 are considered for the analysis of electron and hole envelope wavefunction overlap.

In normal solar cell operation the *p-i-n* structure would be biased at a voltage V_m due to equalization of the illumination and the external load, resulting in an overall electric field

$$E = (V_{bi}{}^0 - V_m)/t_i \qquad\qquad \text{Eq. 3-1}$$

where t_i is the *i*-layer thickness, assuming that all of the *E*-field drops on the *i*-layer because of the high doping in the *n* and *p* layers, $V_{bi}{}^0$ is the built-in voltage of the *p-i-n* structure in the dark and without bias voltage. Assuming such a high doping that $V_{bi}{}^0$ is 1.3V (very close to $E_g{}^{InP}$=1.35eV), the electric field *E* in Eq. 3-1 is proportional to

the operating voltage V_m, which for an ideal solar cell is about 0.3-0.4V lower than the bandgap E_g of the material.

The calculation of the energy band structures and electron and hole energy levels and wavefunctions were done for the QW, IQW, and flipped IQW structures while varying the electric fields. The MATLAB code for the calculation is printed in Appendix A. Below in Figures 3-10, 3-11, 3-12 the results are shown for one particular electric field, 31.1kV, which corresponds to approximately V_m=0.91V (for V_{bi}^0=1.3V and t_i=125nm), an ideal value for maximum power point. Figure 3-13 shows the electron and hole envelope wavefunction overlaps versus electric field (or bias voltage) for IQWSC, flipped IQWSC, and QWSC.
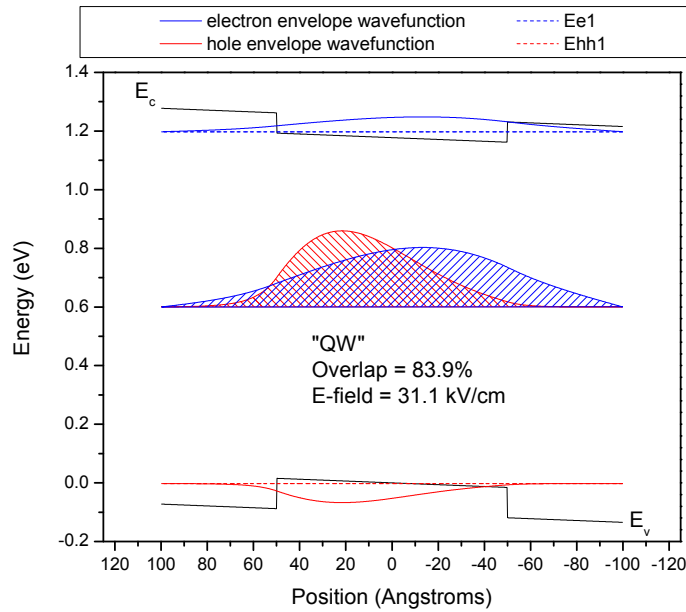
Figure 3-10   Quantum Well energy band diagram with E-field showing electron and hole envelope wavefunctions and their overlap.
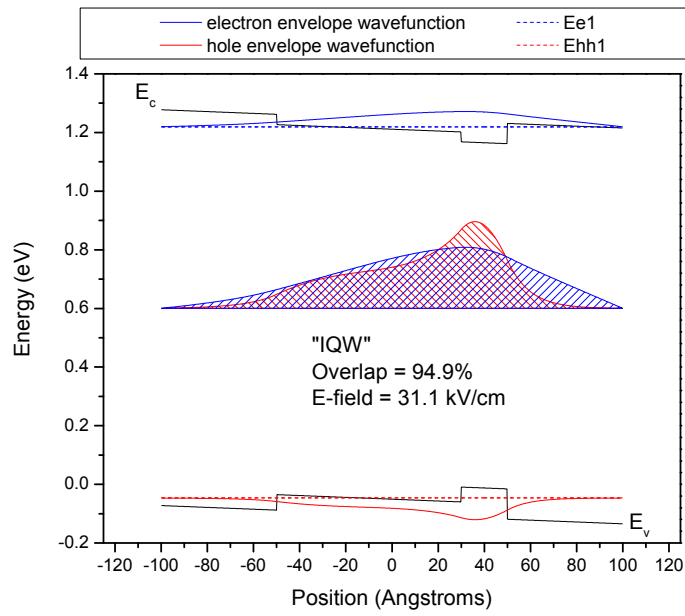
Figure 3-11   Intrastep Quantum Well energy band diagram with E-field showing electron and hole envelope wavefunctions and their overlap.
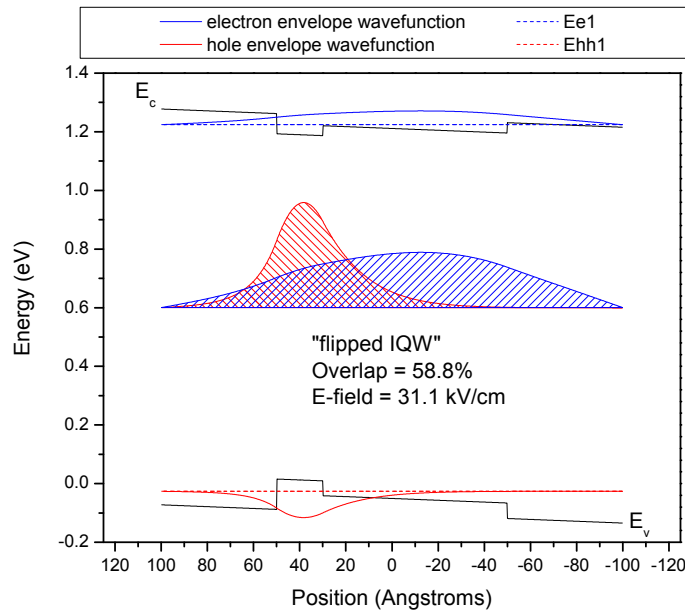
Figure 3-12   Flipped Intrastep Quantum Well energy band diagram with E-field showing electron and hole envelope wavefunctions and their overlap.

Bias Voltage (V) assuming 125nm i-layer and $V_{bi}(V_{bias}=0)=1.3V$
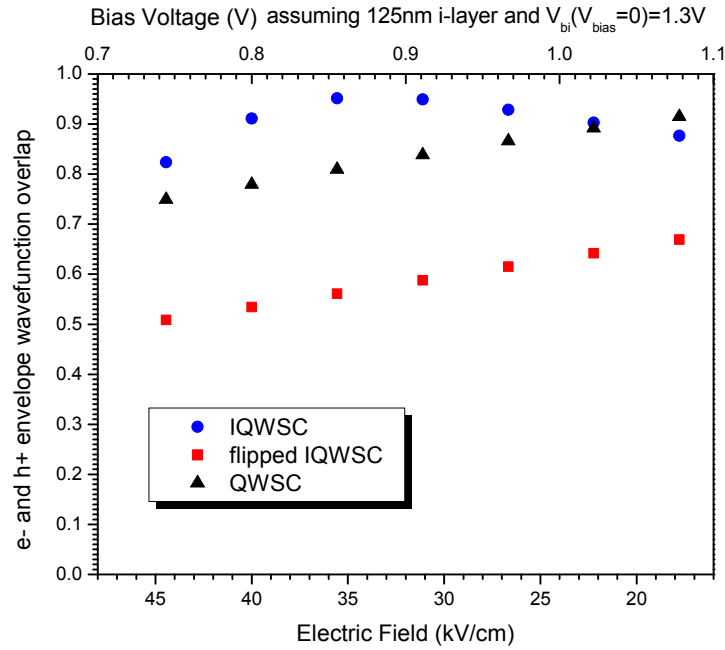
Figure 3-13   Electron and hole envelope wavefunction overlaps versus electric field (or bias voltage) for IQWSC, flipped IQWSC, and QWSC.

3.3.3   Electron and hole barrier heights

In addition to maximizing the overlap of the electron and hole wavefunctions, to increase the current of a solar cell, another strategy is minimizing the barrier heights that the carriers must overcome to escape the quantum wells by thermionic emission, which is assumed to be the only way carriers can escape in this analysis since the InP layer between is relatively thick (tunneling is not considered). In this subsection the barrier heights and the thermionic current for the regular QW, IQW, and flipped IQW are compared. The quantum energy states inside the wells are shown in the above subsection in Figures 3-10, 3-11, and 3-12 as blue and red dotted lines, respectively for electron states and hole states. Figure 3-14 shows a clearer illustration of electrons

and holes overcoming their respective barrier heights. Since electrons drift to the right (*n*-side) during solar cell operation, the barrier height for electrons is the difference between the conduction band level on the right-hand side and the electron state energy level inside the well. Since holes drift to the left (*p*-side), the barrier height for holes is the difference between the valence band level on the left-hand side and the hole energy level inside the well. The barrier heights seen by the electrons and holes are different for each of the different structures (QW, IQW, and flipped IQW) at different biases (i.e., different electric fields). The electron and hole barrier heights versus electric field are plotted in Figures 3-15 and 3-16.
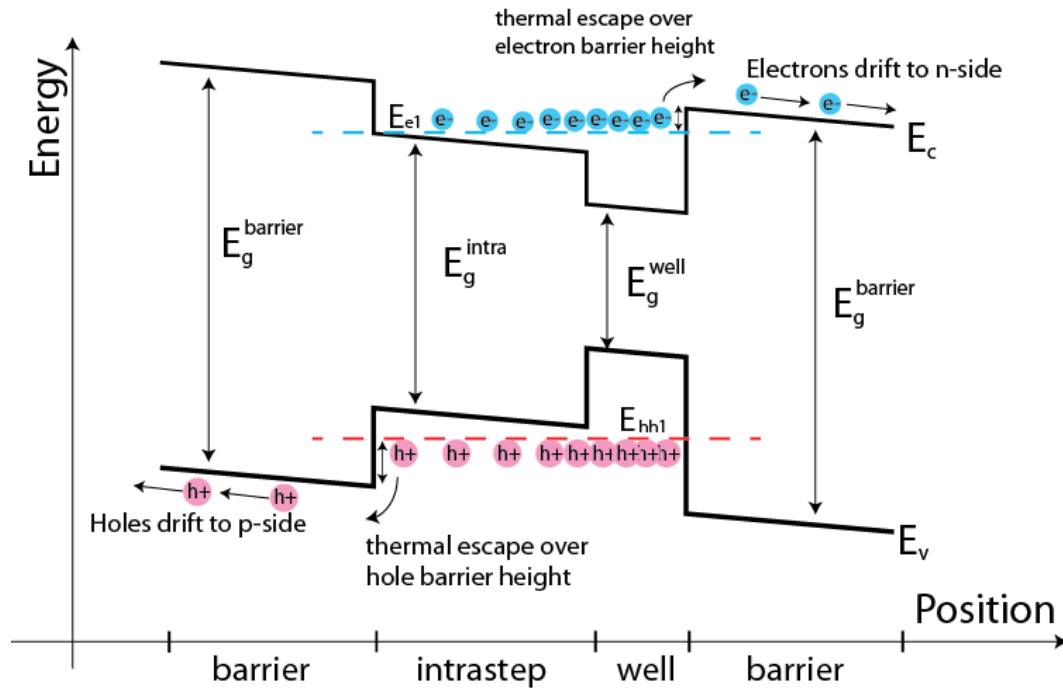
Figure 3-14   Illustration describing electron and hole barrier heights in IQW. Electrons (holes) inside the quantum well are distributed spatially according to the electron (hole) envelope wavefunction at the electron (heavy hole) energy level E_{el} (E_{hh1}). In order for electrons (holes) inside the well to get to the *n*-side (*p*-side), they must first overcome the barrier on the right-hand (left-hand) side of the well, $E_c - E_{el}$ for electrons ($E_{hh1} - E_v$ for holes).
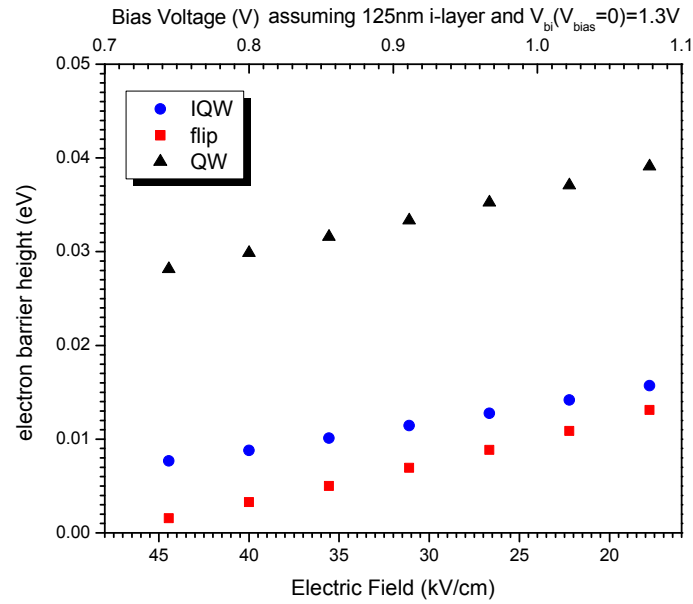
Figure 3-15   Electron barrier height dependence on electric field for IQW, flipped IQW, and QW structures.
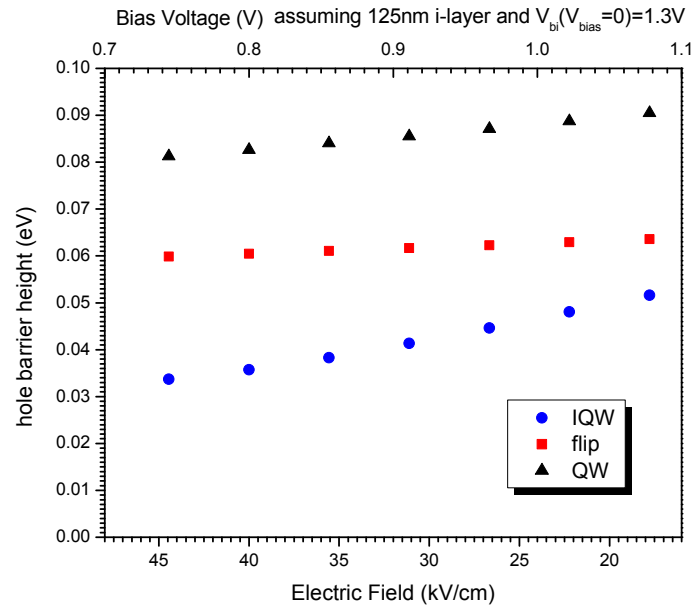
Figure 3-16   Hole barrier height dependence on electric field for IQW, flipped IQW, and QW structures.

Electrons or holes overcoming a barrier due to thermal energy is called thermionic emission, $J_{thermionic}$ which is related to the barrier height by:

$$J_{thermionic} = \int_{E_{c\_barrier}}^{\infty} qv_x dn, \text{ where } dn = g(E)f(E)dE$$

<div align="right">Eqn. 3-2</div>

where $E_{c\_barrier}$ is the conduction band energy of the barrier, q is the fundamental charge, v_x is the carrier velocity in the direction of transport, $g(E)$ is the density of states, and $f(E)$ is the Fermi-Dirac distribution. In the case of the quantum well, $g(E)$ for carriers inside the well is the 2-D density of states $g_{2D}(E)$, but once outside the well, they obey the 3-D density of states $g_{3D}(E)$,

$$g_{2D}(E) = \frac{m^*}{\pi\hbar^2}$$

<div align="right">Eqn. 3-3</div>

$$g_{3D}(E) = \frac{1}{2\pi^2}\left(\frac{2m^*}{\hbar^2}\right)^{\frac{3}{2}}(E - E_c)^{\frac{1}{2}}$$

<div align="right">Eqn. 3-4</div>

where m^* is the effective mass, and $\hbar$ is Planck's constant. The Fermi-Dirac distribution is

$$f(E) = \frac{1}{1 + e^{\frac{E - E_f}{kT}}}$$

<div align="right">Eqn. 3-5</div>

which can be estimated by the Boltzmann distribution

$$f(E) = e^{-\frac{E - E_f}{kT}}$$

Eqn. 3-6

where E_f is the Fermi level and kT is the thermal energy. The simpler Boltzmann distribution can be used if the semiconductor remains non-degenerate with optical generation, which is the case for solar cell with only 1 sun illumination.

Without going through the mathematical details which are often detailed in semiconductor device textbooks (especially in the section on Schottky diode calculations), it is evident, then, that the thermionic emission current is proportional to the effective mass of the carrier m^* and inversely proportional to exponential of the barrier height. With all other things being equal, the difference between the regular QW, the IQW, and the flipped IQW thermionic currents can be described by a thermionic emission factor F, where

$$J_{thermionic} \propto F = m^* \cdot e^{-\frac{E_{barrier}}{kT}}$$

Eqn. 3-7

From this, one can plot out and compare the thermionic emission factor F of the regular QW, the IQW, and the flipped IQW for different bias voltages, shown in Figures 3-17 and 3-18.
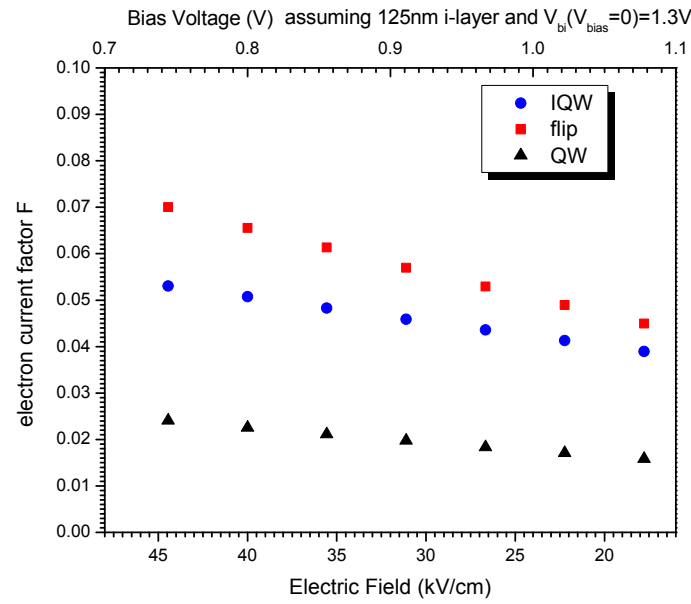
Figure 3-17   Electron thermionic current factor F dependence on electric field for IQW, flipped IQW, and QW structures.
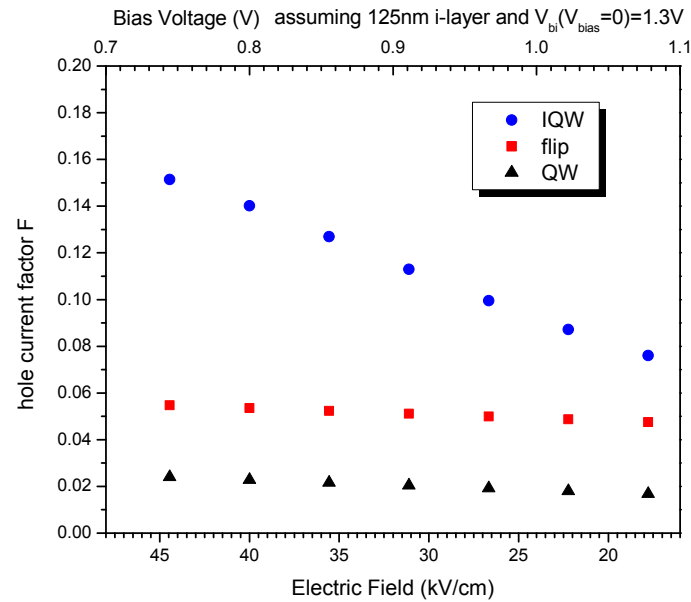
Figure 3-18   Hole thermionic current factor F dependence on electric field for IQW, flipped IQW, and QW structures.

The larger the thermionic current factor the greater chance of carriers in the quantum wells to escape and finally contribute to the overall current of the solar cell. In the case of electrons and holes that are already outside of the wells, if they become recaptured in another well they can also escape faster. The faster the escape times the less chance there is for electrons and holes inside the wells to recombine. Therefore, solar cells with IQWs designed to help carriers escape the wells may have reduced radiative recombination losses.

3.4   Summary of IQWSC theory

In summary, simulations above have shown that the addition of intrastep quantum wells in solar cells can improve the efficiency by (1) increasing the overlap of electron and hole wavefunctions inside the well, thus improving the absorption of photons, and (2) decreasing the barrier height for holes and electrons so that they can more easily thermally escape and thus contribute to the solar cell's current. In the next chapter, the IQWSC and flipped IQWSC are compared with the regular QWSC as well as bulk experimentally.

3.5   Reference

[1]   K. W. J. Barnham, et al., "Recent results on quantum well solar cells," J. Mat. Sci.: Materials in Electronics II, pp. 531-536 (2000).

[2]   S. P. Bremner, et al., "Detailed Balance Efficiency Limits with Quasi-Fermi Level Variations," IEEE Transactions on Electron Devices, Vol. 46, No. 10, p. 1932 (1999).

[3]   http://pveducation.org/pvcdrom/modules/mismatch-for-cells-connected-in-series

[4]   K. Barnham, et al., "Voltage enhancement in quantum well solar cells," J. Appl. Phys.,Vol. 80, No. 2, p. 1201 (1996).

[5]   K. Barnham, et al., "Short-circuit current and energy efficiency enhancement in a low-dimensional structure photovoltaic device," Appl. Phys. Lett., Vol. 59, No. 1, p.137 (1991).

[6]   N. G. Anderson and S. J. Wojtczuk, "Open-circuit voltage characteristics of InP-based quantum well solar cells," J. Appl. Phys., Vol. 79, No. 4, p. 1977 (1996).

[7]   D. C. Johnson, et al., "Observation of photon recycling in strain-balanced quantum well solar cells," Appl. Phys. Lett., Vol. 90, p. 213505 (2007).

[8]   D. Derkacs, et al., "Nanoparticle-induced light scattering for improved performance of quantum-well solar cells," Appl. Phys. Lett., Vol. 93, p. 091107 (2008).

[9]   N. J. Ekins-Daukes et al., "Strained and strain-balanced quantum well devices for high-efficiency tandem solar cells," Solar Energy Materials & Solar Cells, Vol. 68, pp. 71-87 (2001).

[10]   N. G. Anderson, "Ideal theory of quantum well solar cells," J. Appl. Phys., Vol. 78, No. 3, p. 1850 (1995).

[11]   I. Serdiukova et al., "Critical built-in electric field for an optimum carrier collection in multiquantum well *p-i-n* diodes," Appl. Phys. Lett., Vol. 74, No. 19, p. 2812 (1999).

Chapter 4

Experimental Results for Intrastep Quantum Well Solar Cells

4.1   Introduction

In the previous chapter, simulations have shown that it is possible to improve the efficiency of QWSCs by adding an intrastep because (1) the barrier height for holes can be decreased and (2) the overlap between electron and hole envelope wavefunctions can be increased. In this chapter the intrastep quantum well solar cell (IQWSC) is put to the test. The device structure design for the real samples follows the simulations in the previous chapter. The tested IQWSC structure is compared to a InP-only solar cell, a QWSC, and a flipped IQWSC. Wafers were grown by MOCVD and fabricated into solar cell chips, and then tested for current-voltage (I-V) characteristics as well as spectral response via photocurrent measurements, and the results for the different structures are compared.

4.2   Fabrication of IQWSCs

In the experiment four different structures of solar cells were compared: IQWSC, flipped IQWSC, regular QWSC, and InP only. Apart from the *i*-layer (intrinsic layer), all of these structures are identical, shown in Figure 4-1. The layers were grown on 1cm x 1cm rectangular n-type InP (100) substrates by MOCVD, and the growth is described in detail in the next subsection. The *i*-layer contents of the four structures are listed in Table 4-1. Energy band diagrams of the material structure in the *i*-layer can be found in the previous chapter, Figures 3-7 through 3-12.

InGaAs p+ 2.5e18 cm^{-3} (Zn) ~50nm, p–contact layer
InP p+ 2.5e18 cm^{-3} (Zn) 100nm
InP undoped 25nm, Zn diffusion block
i–layer 100nm, varies (see Table)
InP n–type 8e17 cm^{-3} (Si) ~200nm, MOCVD growth buffer
InP n–type ~3e18cm^{-3} (S) (100), substrate Thickness ~400um Area of wafer=1cmx1cm

Figure 4-1   Physical structure of MOCVD-grown solar cell wafer. The bottom-most layer is the *n*-InP substrate. Layers were grown from bottom up. The *i*-layer varies for each sample; descriptions can be found in Table 4-1. The top *p*+InGaAs layer has composition In$_{0.53}$Ga$_{0.47}$As so that it is lattice-matched to InP.

Table 4-1   List of four solar cell samples and their respective *i*-layer contents. InGaAsP1 and InGaAsP2 are lattice-matched quaternary materials with energy bandgaps E_g = 1.26eV and 1.18eV, respectively. InP has a bandgap of 1.35eV.

Sample name	*i*-layer structure from top to bottom
IQWSC3	5x (5nm InP / 8 nm InGaAsP1 / 2 nm InGaAsP2 / 5 nm InP)
Flipped IQWSC3	5x (5nm InP / 2 nm InGaAsP2 / 8 nm InGaAsP1 / 5 nm InP)
QWSC3	5x (5nm InP / 10nm InGaAsP2 / 5 nm InP)
InP	100nm InP

4.2.1 MOCVD growth

Beginning with a new 2-inch InP substrate cleaved into 1cm x 1cm pieces and cleaned in D.I. water in an ultra-sonic bath inside the UCSD Nano3 cleanroom, the MOCVD growth was done at UCSD in a lab outside of the cleanroom in a horizontal-flow reactor chamber with reactant gases trimethyl-indium (TMI) for In, triethyl-gallium (TEG) for Ga, arsine (AsH_3) for As, phosphine (PH_3) for P, silane (SiH_3) for Si dopant, and diethyl-zinc (DEZn) for Zn dopant, and H_2 as the carrier gas. The layers in Figure 4-1 were grown from the bottom ("MOCVD growth buffer" layer) up at 650°C at 20 Torr, except for the top *p* layers, which were grown at 525°C to prevent Zn diffusion into the lower layers. During the switching of gases between layers the pressure inside the chamber was carefully balanced by adjusting the amount of carrier H_2 gas flow for each layer as well as a feedback controlled butterfly valve at the output of the reactor chamber. Prior to growing the final structure, recipes for each layer was developed by growing them separately on InP substrates and measuring their lattice-matching and growth rates by x-ray diffraction (XRD), bandgaps by photoluminescence (PL), and doping concentrations by Hall measurement.

4.2.2 Fabrication procedure

After MOCVD growth, the remaining fabrication was done in UCSD's Nano3 cleanroom (Figure 4-3). First, the wafers were cleaned with solvents (acetone, methanol, isopropyl alcohol), rinsed with DI water, and then cleaned with BOE and rinsed with DI water, and baked at 120°C for 1 minute to remove any water. Next, the p-metal contacts were patterned by conventional photolithography and lift-off in acetone of e-beam evaporated Pd/Ti/Au (50nm/50nm/100nm). The pattern, shown in Figure 4-2, is of a concentrator style metal pattern. Using the patterned metal as a mask, the exposed p+-InGaAs layer was etched with a $3H_3PO_4:4H_2O_2:1H_2O$ solution for ~5s. A layer of SiO_x (~50nm, thin enough to be scratched through by electrical probes for measurement) was deposited by PECVD to passivate the newly exposed p-InP. Finally, Pd/Ti/Au (50nm/50nm/200nm) was deposited on the entire back side of the wafer, that is, the bulk n-InP, by e-beam evaporation, for the n-metal contact.
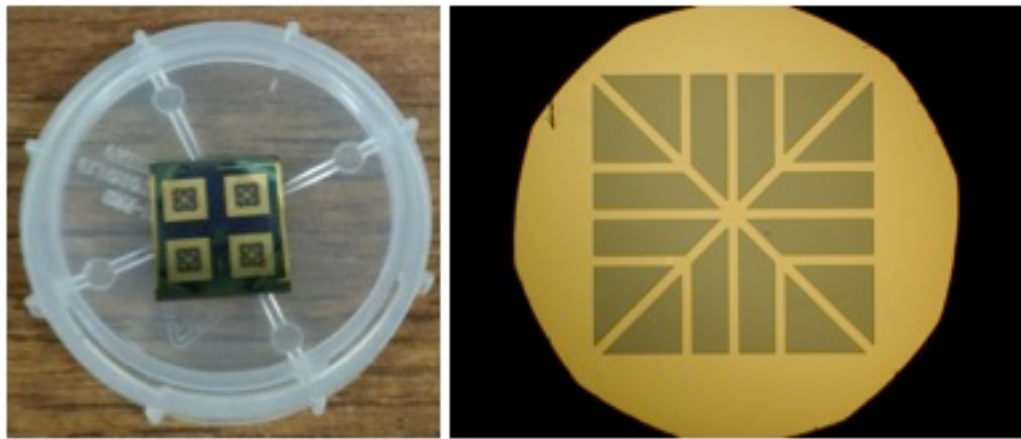
Figure 4-2   Pictures of fabricated solar cell chips. Left: Array of four solar cells on one 10mm by 10mm substrate inside a 1-inch wafer container. Right: Optical microscope image of metal pattern.

1. Wafer is cleaned with acetone, methanol, isoproanol, and DI water.

~50nm p+InGaAs layer

Other layers, substrate

wafer after MOCVD growth

2. Top p-metal Ti/Pd/Au is patterned by photolithography, e-beam evaporation, and metal lift-off.

Metal (Ti/Pd/Au)

3. Exposed p+InGaAs is etched for 5s with 3H_3PO_4:4H_2O_2:1H_2O solution using metal pattern as an etch mask, exposing p-InP through the windows.

p-InP exposed

4. 50nm SiO_x is deposited by PECVD over entire top surface to passivate top p-InP layer. Electrical probes can scratch through this layer for top contact.

SiO_x

5. Ti/Pd/Au n-metal is deposited on entire backside by e-beam evaporation.

Metal (Ti/Pd/Au)

6. Fabricated chip is diced and mounted on sapphire handler via Cu tape.

Diced chip

Copper conductive tape

Sapphire handler wafer

Figure 4-3   Fabrication steps of solar cell chips.

The samples were then diced using a diamond saw blade into individual chips or quarter chips. The reason for the dicing is to isolate areas of the wafer that have severe shunts or shorts that have occured during MOCVD growth. Only the pieces that exhibited the best I-V curves (low series resistance and high shunt resistance) were used. For the measurements, the pieces were mounted on electrically conducting copper tape, which was adhered to a 2-inch sapphire handler wafer, as seen in Figure 4-4. The copper tape has a direct electrical connection with the back n-InP substrate. The purpose of the sapphire handler wafer is for robust handling and convenient mounting of the samples on the measurement stage, usually by vacuum.
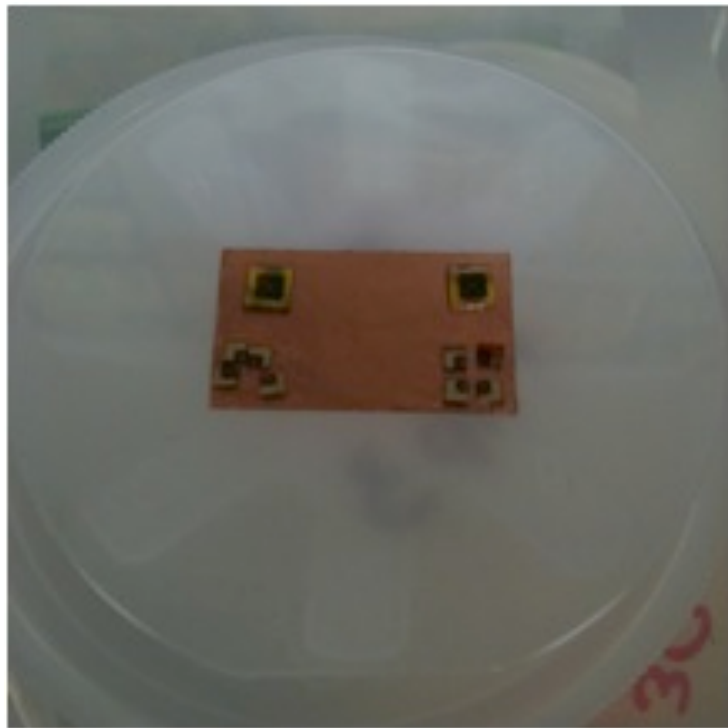
Figure 4-4   Picture of diced solar cell chips. Each chip was diced along the edge of the metal pattern into squares. Some samples were further diced into quarters. Back metal n-contact is in electrical contact with copper tape (rectangular area), which was mounted on a 2-inch sapphire handler wafer.

4.3 IQWSC Measurements

In this section the IQWSC measurement results are presented and discussed. Two types of measurements were done: (1) current versus voltage (I-V) measurements with illumination from a solar simulator lamp with the illumination of 1 sun at AM1.5 and (2) spectral photocurrent measurements, where a monochromator was used to select narrow spectral segments of a white light source to be incident on the sample, and the resulting electrical current was measured. The measurement results for the IQWSC, an IQWSC with the intra-layer and the well-layer were flipped (which is referred to in this section as the "flip" sample), were compared to that of the QWSC and the bulk InP solar cell.

4.3.1 *I-V* measurements

The *I-V* characteristics of the IQWSC, flipped IQWSC, regular QWSC, and InP solar cells were measured in the configuration illustrated in Figure 4-5. The solar cell, attached to the sapphire handler wafer via electrically conducting copper tape, was illuminated from above by one sun, AM 1.5 solar simulator. The sapphire handler wafer was positioned on the measurement stage by vacuum. Manual positioners (not shown) were used to connect electrical probes to the solar cell terminals. For the *p*-side, the probe was directly in contact with the metal on the *p*+InGaAs; for the *n*-side, the probe was in contact with the conductive copper tape, which was in electrical contact with the backside metal on the *n*-InP substrate. The probes were then

connected to Agilent B1500 semiconductor parameter analyzer for the *I-V* measurement. The current *I* was measured while voltage *V* varied from -1V to +1V.
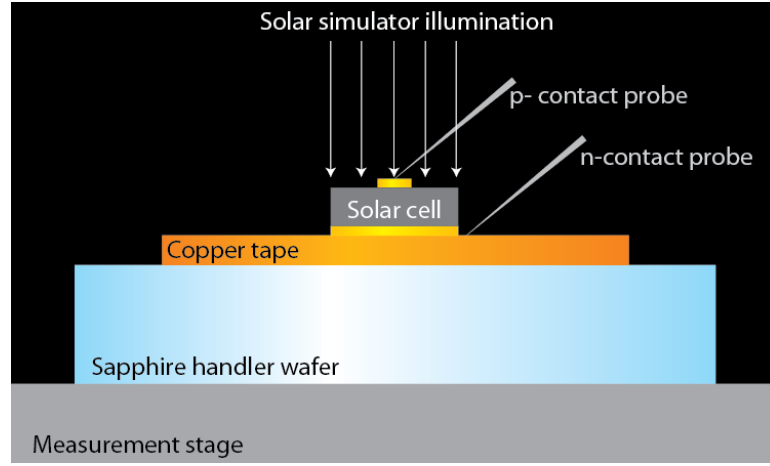
Figure 4-5   Solar cell measurement schematic (lateral view).

Table 4-2 shows the figures of merit from the measurement results. The IQWSC had the largest I_{sc}, P_{max}, *FF*, and η. Figures 4-6 and 4-7 show the illuminated *I-V* and *P-V* curves, respectively. The overall low efficiencies measured in this experiment (1-2%) are likely due to the fact that the absorbing *i*-region is very thin (only 100nm), and that the growth and fabrication are not fully optimized.

Table 4-2   Solar cell figures of merit from measured *I-V* results.

	InP control	QWSC3	IQWSC3	Flip3
V_{oc} (V)	0.58	0.57	0.58	0.60
I_{sc} (µA)	31.5	34.0	36.9	34.8
P_{max} (µW)	11.5	12.0	14.2	13.4
FF	0.63	0.62	0.67	0.64
Efficiency η	1.6%	1.7%	2.0%	1.9%

Figure 4-6 shows the *I-V* characteristics of each solar cell under AM1.5, 1 sun illuination. The short-circuit current I_{sc}, an indication of how much light is absorbed and converted into electrons and holes, of the InP-only cell is the lowest, followed by the regular QW cell, then the flipped IQW cell, and the IQW cell with the highest I_{sc}. The open-circuit voltage V_{oc} of the flipped IQW solar cell is unexpectedly the highest.

Measured solar cell I-V characteristics
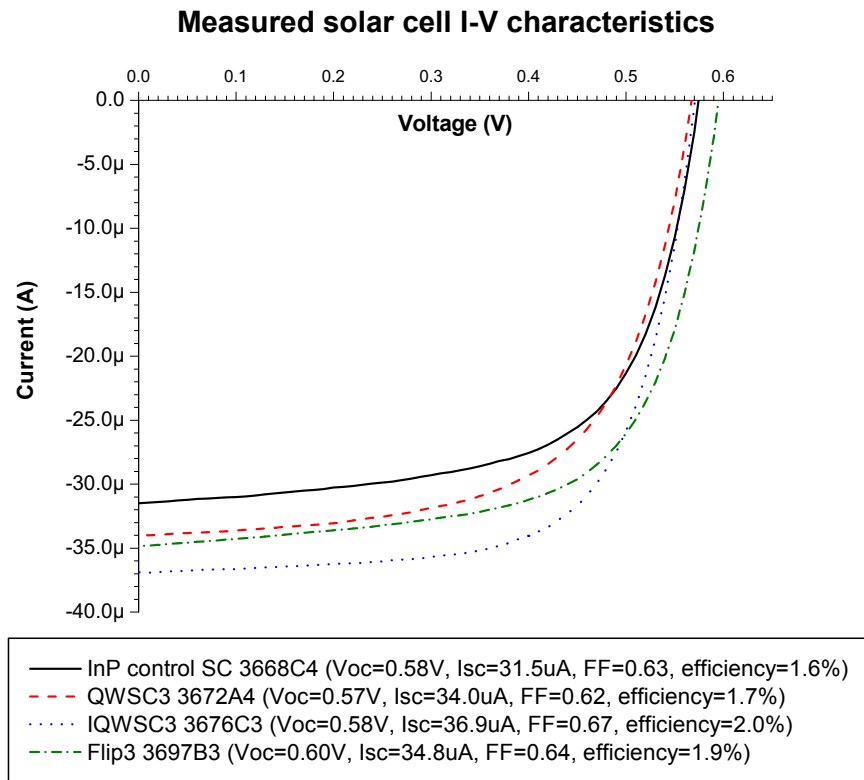
Figure 4-6   Measured Solar Cell *I-V* curves.

Studies have shown that QWSCs can have higher V_{oc} than expected due to low dark current of QW *p-i-n* structure compared to a uniform *p-i-n* structure with the same effective bandgap as the QWs [1]. Carrier escape sequence may also play a part in higher V_{oc} when electrons escape first, which is the case with the flipped IQW

structure [2]. However, neither of these can explain the flipped IQWSC having a V_{oc} larger than the InP control cell. Rather, it is most likely due to parasitic effects from fabrication, which is discussed later.

Figure 4-7 shows the power versus voltage *P-V* curve, which was derived from the *I-V* curve simply by multiplying *I* by *V* for *P*. This curve is useful for finding the actual maximum power P_{max} for each solar cell, defined as the maximum point in the *P-V* graph, although it occurs at different *V* for each cell. The *V* at which the P_{max} occurs is called V_{max}. V_{oc}, where *P*=0 (since *I*=0) can also be read from this graph.
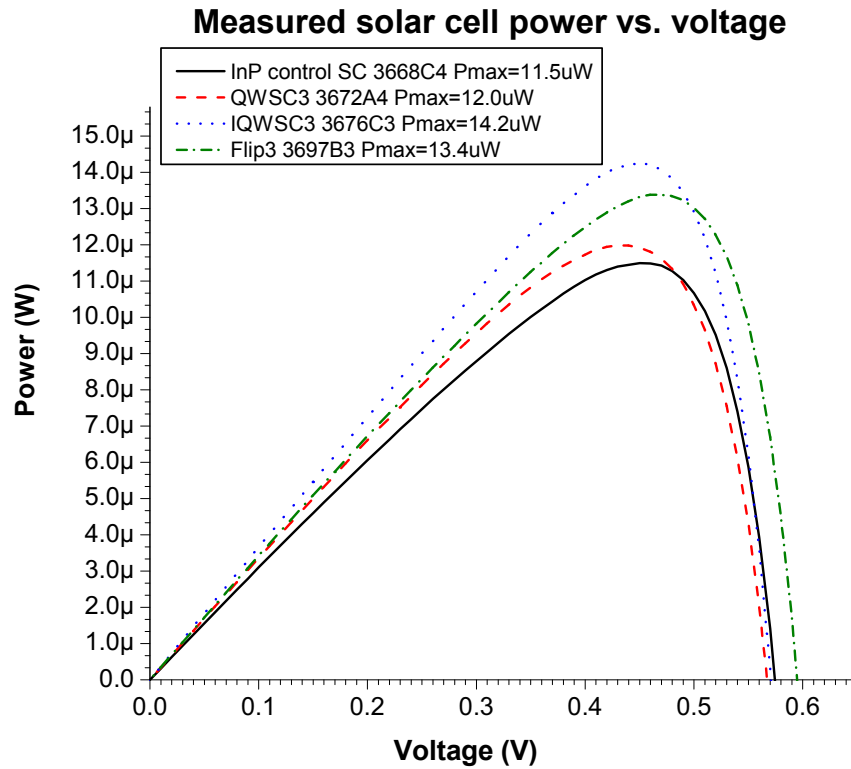
Figure 4-7   Measured Solar Cell Power-Voltage curves.

The dark *I-V* characteristics (Figure 4-8) give some insight to the quality of the solar cell, which affects its efficiency. Generally, materials with higher (effective) bandgaps have lower dark current, and in this case, the InP control cell should have lowest dark current. However, if there is a difference in material quality or electrical contact quality, there may be unexpected dark current results. An interesting anomaly in this set of samples is that the flipped IQW cell exhibits the lowest dark current, lower than the InP control cell. The InP control cell has the highest dark current for voltage ranges between 0 and ~0.4V, but is lower than the regular QW cell and the IQW cell for voltages greater than 0.4V. The low dark current could partly explain the high V_{oc} of the flipped IQW cell.

Measured solar cell Dark I-V characteristics
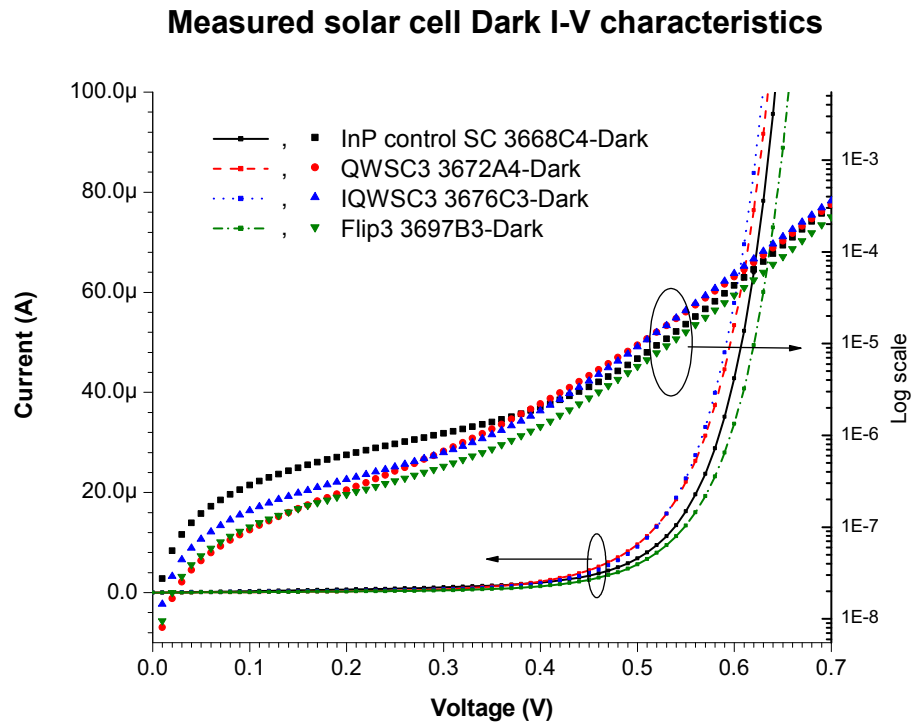
Figure 4-8   Measured solar cell dark *I-V* characteristics. Both linear (left axis) and log (right axis) are shown.

4.3.2   Parasitic resistances of measured solar cells

Non-idealities of solar cells, attributed to material quality issues, design non-idealities, and fabrication anomalies, can be modeled by parasitic resistances, series resistance R_{Series} and shunt resistance R_{Shunt}, as discussed in Chapter 2.   Parasitic resistances cause a drop in fill factor and maximum power, as well as reduction of I_{sc} and V_{oc}, when they are severe.

In this subsection the method of extracting R_{Series} and R_{Shunt} from measured dark I-V data is described. In the dark the current source I_L is zero, and the equivalent circuit of the solar cell is as shown in Figure 4-9. Notice that the polarity for current I is flipped compared to the equivalent circuit in Figure 2-11, for simplicity in the dark I-V analysis. The parasitic resistances are assumed to be "mild," that is, R_{Series} is a few Ohms and R_{Shunt} is greater than a few thousand Ohms.
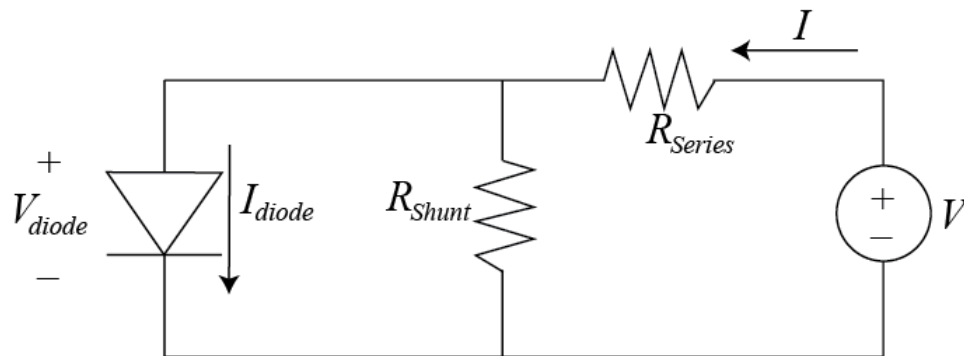
Figure 4-9   Equivalent circuit of solar cell with parasitic resistances in the dark.

First, in the case of large, positive voltage V, the diode is forward-biased so that the current I goes through the diode rather than R_{Shunt}, so for simplicity, $I = I_{diode}$,

$$I = I_s \cdot e^{q\frac{V - IR_{Series}}{nkT}}$$ Eqn. 4-1

where I_s is the saturation current, n is the ideality factor of the diode, kT is the thermal energy. The -1 in the ideal diode equation is neglected here since high forward bias is assumed. The natural log of both sides of Eqn. 4-1 can be taken,

$$\ln(I) = \ln(I_s) + q\frac{V - IR_{Series}}{nkT}$$ Eqn. 4-2

Then the derivative with respect to I can be applied to both sides of Eqn. 4-2, a linear relationship between the derivative of V with respect to I and the inverse of I can be found, from which R_{Series} can be extracted.

$$\frac{dV}{dI} = R_{Series} + \frac{nkT}{q}\left(\frac{1}{I}\right)$$ Eqn. 4-3

Using the dark I-V data for each solar cell, dV/dI can be plotted versus $1/I$. In this case, the area of interest is in the range of large, positive current I, or when $1/I$ approaches zero, as shown in Figure 4-10. R_{Series} is then the y-intercept of the graph,

when dV/dI is extrapolated as a linear function around $1/I \rightarrow 0$ range. The series

resistance for the measured solar cells are around 5-7Ω.
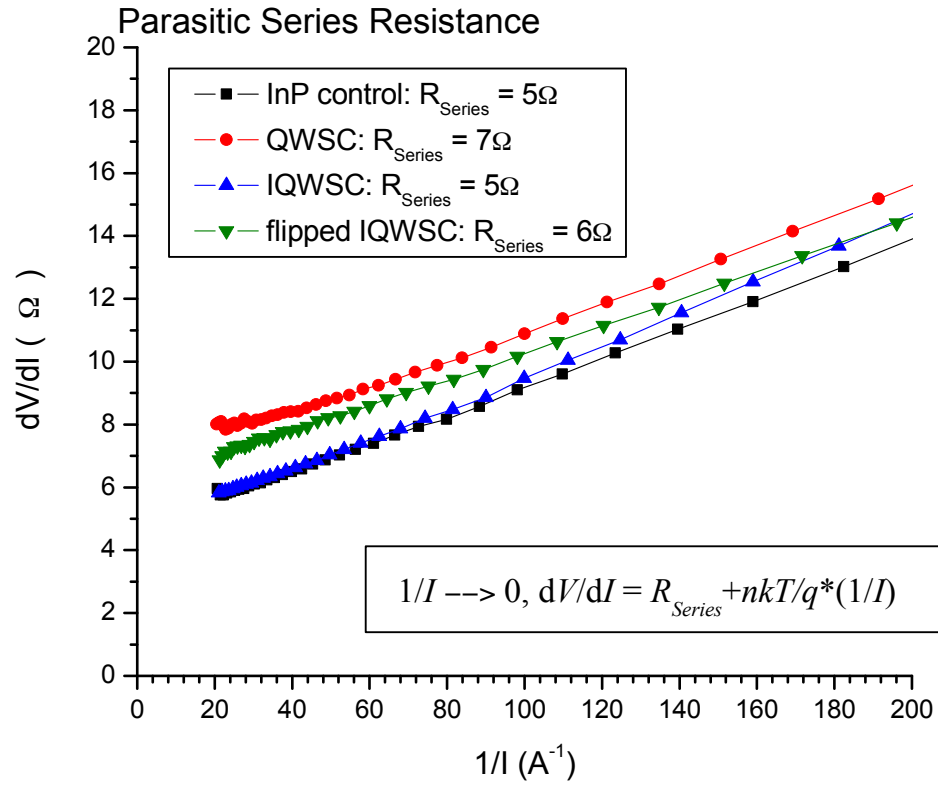
Figure 4-10   Extraction of series resistance from dark *I-V* data.   For the measurement the current was limited to 50mA, so $1/I$ ends at 20A^{-1}.

On the other hand, shunt resistance becomes measureable when the applied

voltage *V* is a very small positive, so that the diode in the circuit in Figure 4-9 is

almost off, so that I_{diode} is almost zero. In this case, the current going through R_{shunt}

can be assumed to be equal to *I*, so that

$$V = I \cdot (R_{Series} + R_{Shunt})$$ Eqn. 4-4

and taking the derivative with respect to *I* on each side,

$$\frac{\mathrm{d}V}{\mathrm{d}I} = R_{Series} + R_{Shunt} \qquad \text{Eqn. 4-5}$$

for *I*→0+, or 1/*I*→+∞. The same dark *I-V* data for each solar cell is plotted as d*V*/d*I* versus 1/*I*, but in the range where 1/*I* is very large, as shown in Figure 4-11. From this analysis the series and shunt resistances of the measured solar cells are extracted and listed in Table 4-3, along with the figures of merit discussed earlier.
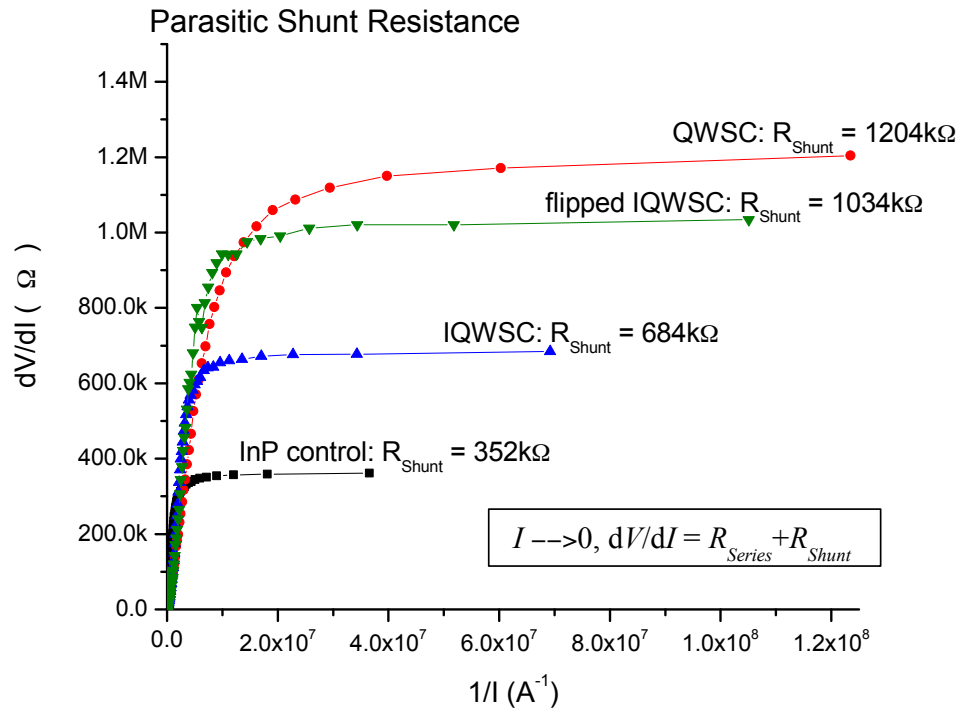
Figure 4-11   Extraction of shunt resistance from dark *I-V* data.

Table 4-3   Solar cell parasitic resistances from measured dark *I-V* results and figures of merit from measured illuminated *I-V* results.

	InP control	QWSC3	IQWSC3	Flip3
R_{Series}	5Ω	7Ω	5Ω	6Ω
R_{Shunt}	352kΩ	1204kΩ	684kΩ	1034kΩ
V_{oc} (V)	0.58	0.57	0.58	0.60
I_{sc} (μA)	31.5	34.0	36.9	34.8
P_{max} (μW)	11.5	12.0	14.2	13.4
FF	0.63	0.62	0.67	0.64
Efficiency η	1.6%	1.7%	2.0%	1.9%

The parasitic resistances, as discussed in Chapter 2, can affect the efficiency η of a solar cell. From the simulation results in Figures 2-12, 13, and 14, it can be seen that the *FF*, V_{oc}, and I_{sc} may be reduced due to parasitic resistances. The measured R_{Series} for the four solar cells are close, around 5-7Ω. However, the R_{Shunt} vary greatly. The InP control cell had the smallest R_{Shunt} of 352kΩ, which is about 3 times smaller than the flipped IQW cell with 1034kΩ, which may explain why the V_{oc} of the InP control cell is lower than that of the flipped IQW cell.

The measured *I-V* results for the four solar cells, InP control, regular QWSC, IQWSC, and flipped IQWSC, show that there is improvement of efficiency due to QWs and IQWs in the solar cell absorption region. The design goal of the QWSCs, to increase photocurrent without decreasing voltage, is achieved by all three cells with QWs or IQWs, compared to the InP control cell. The design goal of the IQWSC, to

increase efficiency by increasing the optical transition probability and by decreasing the barrier height for the holes, is achieved by the IQWSC compared to the regular QWSC and the flipped IQWSC. The anomaly of the flipped IQWSC having a higher V_{oc} compared to the InP control cell is explained in the above discussion by the relative parasitic resistances.

4.3.3   Spectral photocurrent measurements

The spectral photocurrent measurement results discussed in this subsection are useful for confirming the effect of quantum wells by determining the electrical current response to different photon wavelengths. While the InP control cell responds to light with wavelength up to the bandgap wavelength λ_g of InP, approximately 920nm, by

$$\lambda_g \text{ [nm]} = 1240/E_g \text{ [eV]} \qquad\qquad \text{Eq. 4-6}$$

the solar cells containing quantum wells should respond to light of wavelength up to the lowest optical transition allowed in the wells, longer than 920nm. The spectral photocurrent can be measured for different applied biases, which may give clues about the absorption and electron and hole wavefunction overlaps due to band bending.

The physical setup for the spectral photocurrent measurement is similar to that of the *I-V* measurement as shown in Figure 4-5, except the illumination is monochromatic light, using a white light source that passes through a monochromator,

which contains mechanical components that rotate gratings and mirrors to select very small wavelength ranges (on the order of a few nanometers) at a time to illuminate the solar cell. Similar to the *I-V* measurement, current is measured through the electrical probes connected to the *p* and *n* metals of the solar cell chip, but the bias *V* is held constant while the illumination wavelength λ is varied from 350nm to 1100nm with 2nm step size, and the spectral photocurrent *I(λ)* was measured for each of the four solar cells at short-circuit (or *V*=0) and at +0.4V, close to V_{max} (see Figure 4-7).

A calibration measurement was done each time one of the solar cells was measured to eliminate changes in the white light spectrum and environmental factors between measurements. In the calibration measurement, the spectral photocurrent of a commercial photodetector $I_o(\lambda)$ with a known spectral external quantum efficiency $EQE_o(\lambda)$ (given by the manufacturer) was measured. The quantum efficiency is the ratio of the number of electrons collected by the photodetector and the number of photons incident on the photodetector. The external quantum efficiency of the solar cell *EQE(λ)*, is related to its measured photocurrent *I(λ)* by the equation

$$EQE(\lambda) = \frac{EQE_o(\lambda)}{I_o(\lambda)} \cdot I(\lambda)$$
<div align="right">Eq. 4-6</div>

where the subscript *o* refers to the calibration photodetector. Figures 4-12 and 13 show the *EQE(λ)* for the wavelength range between 350nm and 1100nm of the four solar cells at *V*=0 and *V*=+0.4V, respectively.
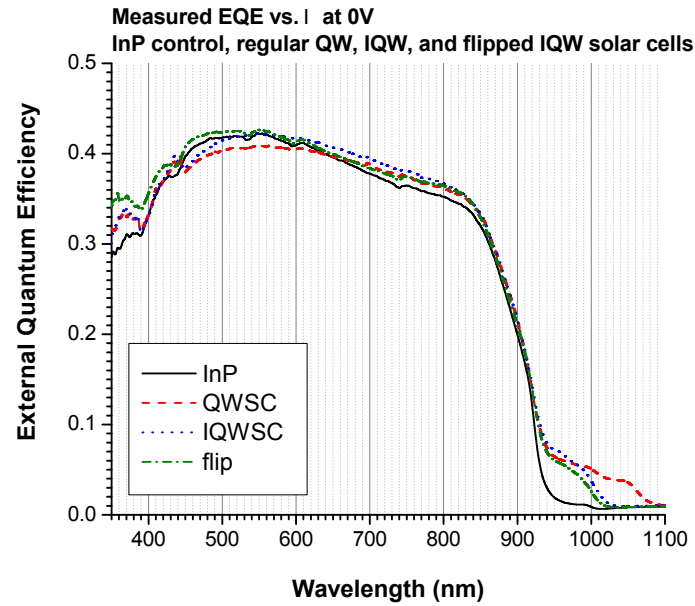
Figure 4-12   Measured external quantum efficiency versus wavelength for InP
control, regular QW, IQW, and flipped IQW solar cells at short-circuit (*V*=0).
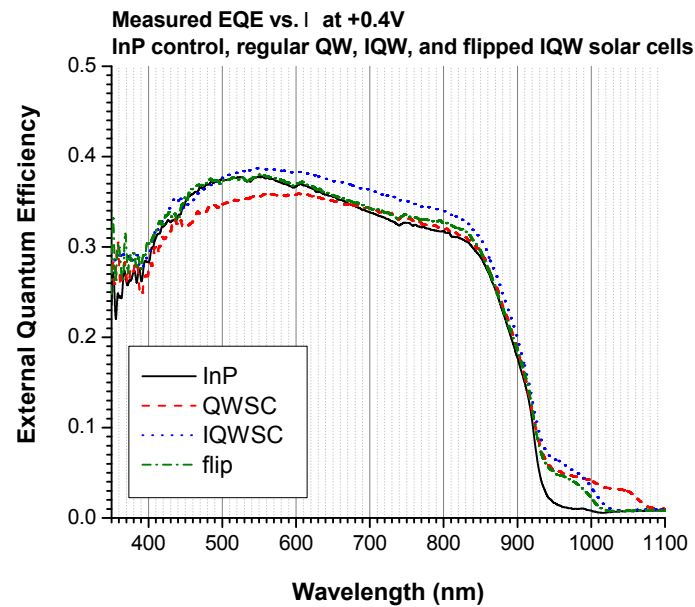
Figure 4-13   Measured external quantum efficiency versus wavelength for InP
control, regular QW, IQW, and flipped IQW solar cells at applied bias *V*=+0.4V.

In Figures 4-12 and 13 for $\lambda > \lambda_{InP} = 920$nm the *EQE* of the InP control cell drops to zero, while the *EQE* of the solar cells with quantum wells extend out to longer wavelengths, proving that additional current can be produced by photons absorbed in the QWs. The regular QW has a deeper well than the IQW or flipped IQW, as confirmed by the *EQE* measurement. In the range 350nm $< \lambda <$ 920nm the *EQE*(λ) curves for all four solar cells follow the same trend. From about 500nm to shorter wavelengths the *EQE* for all of the solar cells decrease because the shorter the incident photon wavelength, the more likely they are absorbed closer to the top surface (in the *p*-region) of the device where they are likely to recombine before being able to contribute to the total current [1]. For 500nm $< \lambda <$ 850nm the *EQE* for all four solar cells range around 0.3 to 0.4, meaning that about 30-40% of the photons incident within that wavelength range contribute to current, an indication that the 100nm *i*-layer of the solar cell is perhaps too thin to be completely opaque, or to absorb every photon with energy larger than the bandgap. Ideally, if all of these photons in this range are absorbed, main cause of loss would be low diffusion length [2]. The difference between Figures 4-12 and 13 is the bias voltage, where *EQE* is larger (thus the photocurrent *I* is larger) for *V*=0, since there is zero diode current at short-circuit, whereas at +0.4V, the diode is forward-biased, so that there is non-zero diode current in the opposite direction of the photocurrent, causing the *EQE* overall to be lower.

Figure 4-14 shows the *EQE* data for λ range 900-1100nm for the four solar cells separately, comparing the *EQE* at the two biases. The *EQE* for $\lambda > \lambda_{InP}$ of the IQWSC for +0.4V does not drop as much as it does for the flipped IQWSC or the

QWSC. This may suggest that the IQWSC is better able to produce photocurrent at the solar cell's operating bias because of its large electron and hole wavefunction overlap and small hole barrier height at forward bias (Figures 3-13, 16).
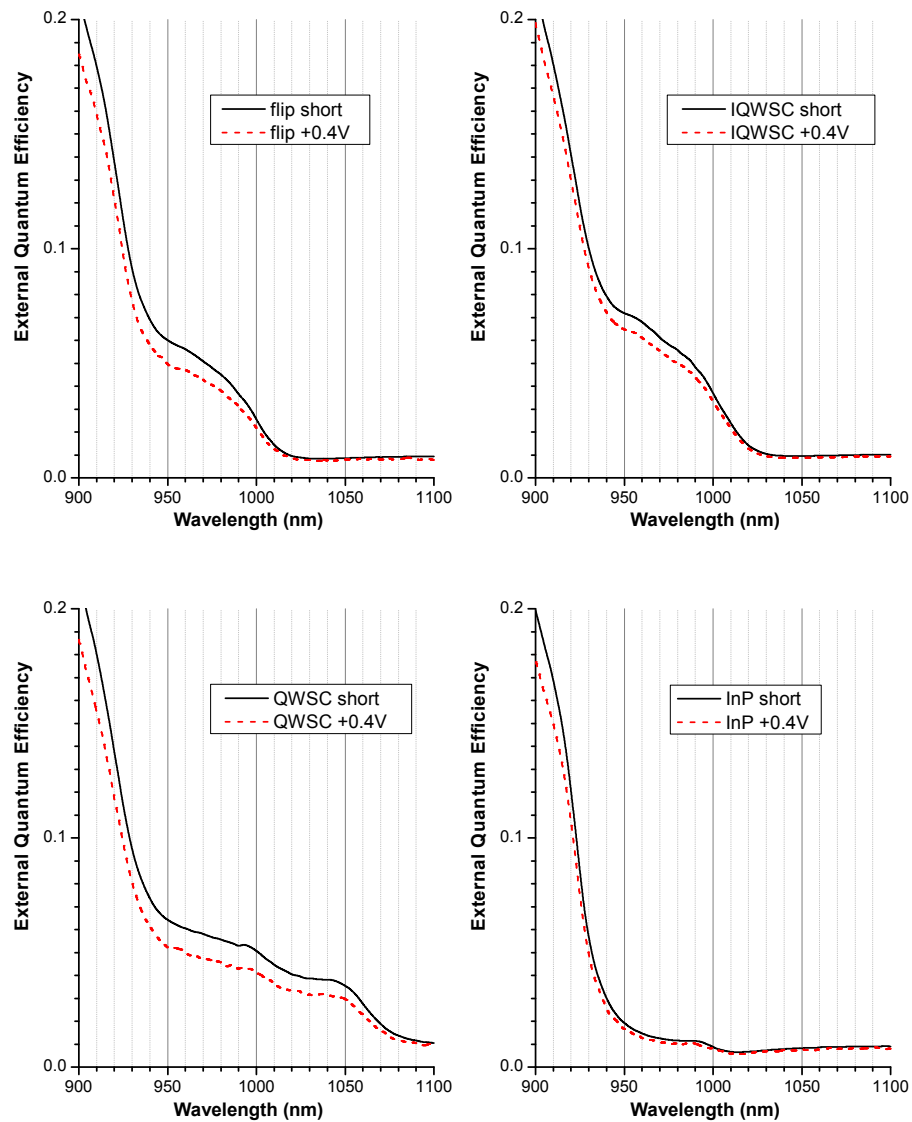
Figure 4-14   Measured external quantum efficiency for wavelength range between 900nm and 1100nm, separated by device, for bias voltages 0V and +0.4V.

4.4   Summary of IQWSC experiment

The *EQE* measurements confirm that the solar cells with QWs respond to photons with longer wavelengths than the InP bandgap wavelength, and this additional photocurrent can increase the solar cell efficiency. The *EQE* at different bias voltage for different QWs suggest that the electric field, and thus bending of bands, changes the photocurrent. Thus in the solar cell current from the analysis in Chapter 2,

$$I = I_{diode} - I_L = I_S(e^{\frac{qV}{kT}} - 1) - I_L \qquad \text{Eq. 4-7}$$

the photocurrent I_L, which is often taken to be dependent of the illumination power and independent of V, may be dependent on V for solar cells with IQWs.

The *I-V* and spectral photocurrent measurements for the InP control, regular QW, IQW, and flipped IQW solar cells show that there is an increase in solar cell efficiency due to QWs, and that the structure of the QW makes a difference. The IQWSC, which was designed to optimize the electron and hole wavefunction overlap and decrease the hole barrier height, showed to have the greatest efficiency of all four tested solar cells.

4.5   References

[1] S. M. Sze, <u>Physics of Semiconductor Devices</u>, third edition, John Wiley & Sons, Inc., pp. 729-30 (2007).

[2] http://pveducation.org/pvcdrom/solar-cell-operation/quantum-efficiency

Chapter 5

Solar Spectral Condenser Theory

5.1   Introduction

Converting solar light into electrical current is not the only way to harvest energy from the sun. In fact, there can be other more effective ways to convert sunlight into usable energy. In Chapter 2 the three intrinsic losses of a solar cell were discussed: (1) photons with energy less than the material bandgap, (2) thermalization of photons with energy greater than the material bandgap, and (3) radiative recombination. The loss due to radiative recombination is an intrinsic loss due to the nature of photovoltaic cells: the photons are converted into electron and hole pairs that can recombine before contributing to current. This is the fundamental reason why the work done per collected photon is always less than the bandgap energy of the material. Perhaps one solution in overcoming loss #(3) is not to convert photons into electrical current but to concentrated light beams, which can be used as energy. Since the output of such a device is photons instead of electrons, loss #(3) may be avoided. The main focus of this chapter is the solar spectral condenser, a device that converts broad-spectrum light from the sun into coherent single-wavelength light which can be

collected and distributed via optical fibers. The light output from the solar spectral condenser device can be used immediately as a light source for indoor lighting and farming, the input for a photovoltaic solar cell with high efficiency (since the input light is of a single wavelength), or for heating. Figure 5-1 shows an artist's rendition of the solar spectral condenser in everyday use.
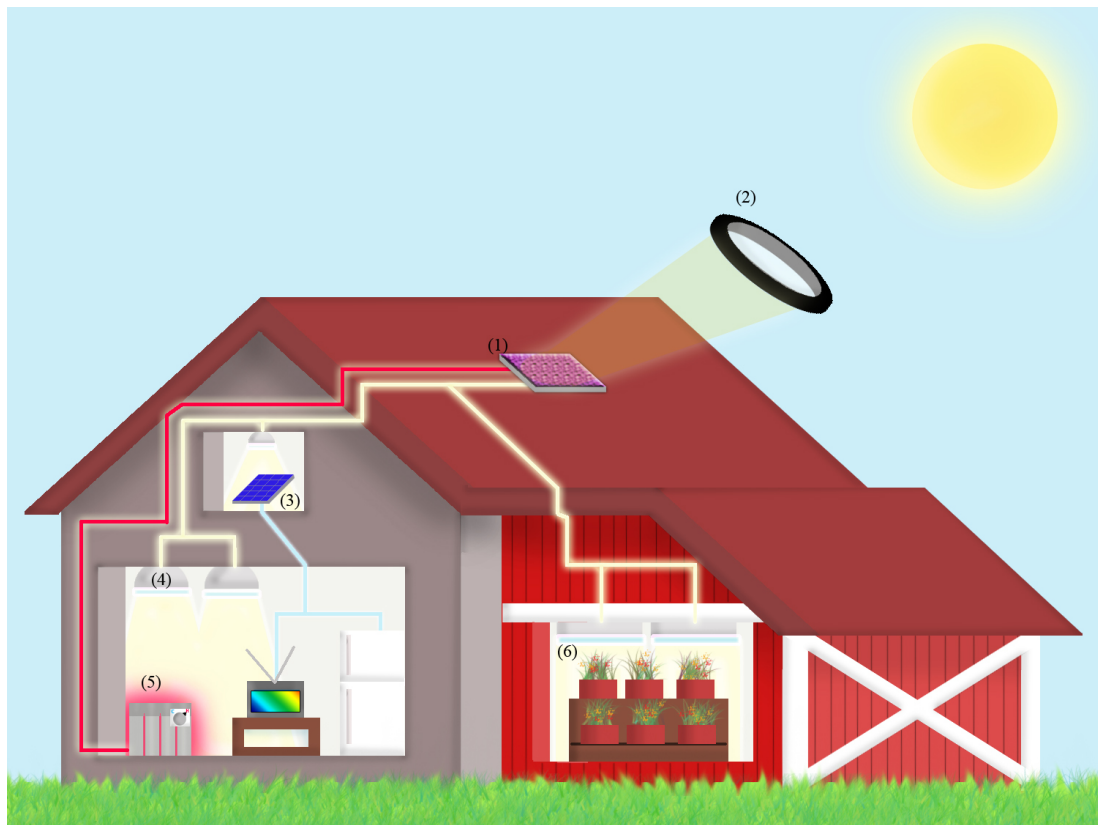
Figure 5-1   Artist's rendering of the solar spectral condenser in everyday use. The solar spectral condenser module (1) is illuminated with sunlight via a concentrating lens system (2). Energy in the form of coherent light output from the solar spectral condenser is transported via optical fibers to be used for the input of a photovoltaic module (3), directly as indoor lighting (4), heating (5), and indoor farming (6). Credit: Daniel Estrada.

5.2   Theoretical analysis of the solar spectral condenser

The solar spectral condenser device, shown in Figure 5-2, is a semiconductor structure with a slab waveguide having a gain medium with gain coefficient $\gamma(v)$, where v is the wavelength of the light (1). It has two inputs: the first is the solar illumination from above I_o (2), which can be first concentrated using a lens system (not shown), and the second is a seed laser signal I_{in} (3) coupled into the waveguide from one facet. From the opposite facet the output I_{output} (4), energy in the form of an amplified signal with the same wavelength as the seed laser, can be collected.

(1) Gain medium $\gamma(v)$ & waveguide
(2) Solar illumination I_o : high power, random
(3) Seed laser signal I_{in} : low power, highly ordered
(4) Output I_{output} : amplified seed laser power, highly ordered
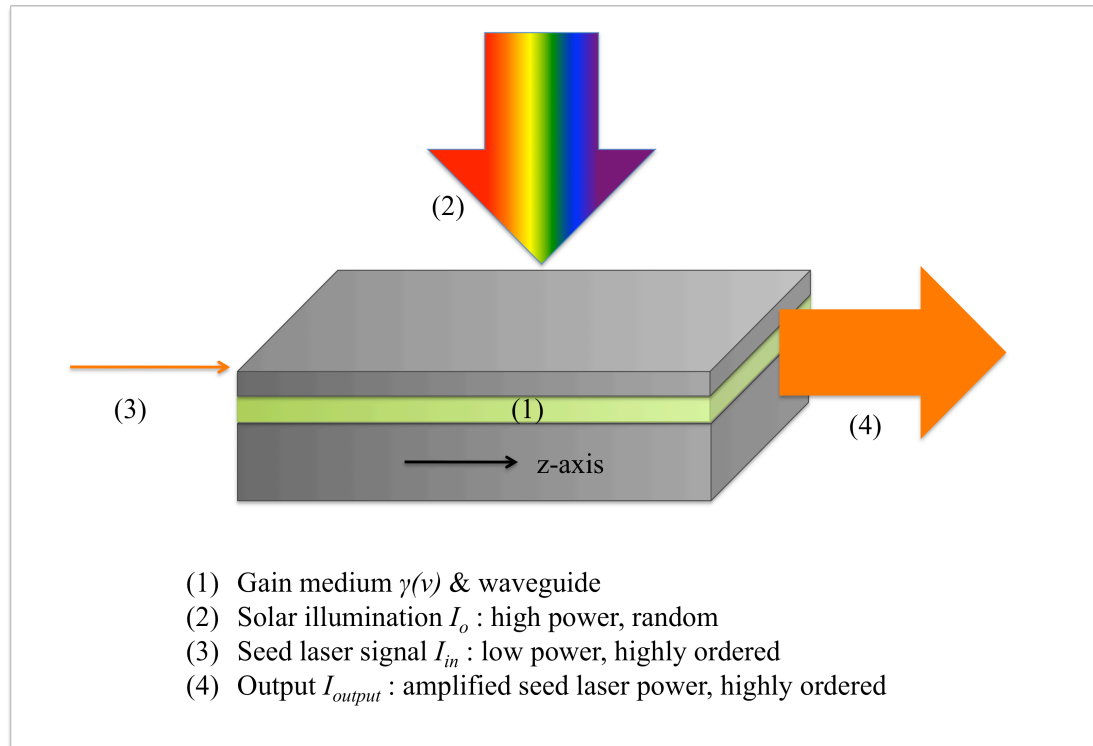
Figure 5-2   Schematic of the basic structure of the solar spectral condenser.

In the presence of incident radiation by solar illumination, at steady state and prior to the onset of radiative recombination, the carriers generated via the absorption is proportional to the incident radiation, and is approximately given by,

$$n = \alpha I_o \tau_{sp}$$
Eq. 5-1

where n is the carrier density per unit volume in the quantum well region, α is the absorption coefficient of the quantum wells, I_o is the incident light intensity per unit time per unit area, τ_{sp} is the spontaneous carrier lifetime. This n is responsible for the optical gain $\gamma(v)$ which amplifies the seed light at frequency v with a linewidth $g(v)$ [1]:

$$\gamma(v) \quad = \quad n \frac{c^2}{8\pi\mu^2 v^2 \tau_{sp}} g(v) = \frac{\alpha I_o c^2}{8\pi\mu^2 v^2} g(v)$$
Eq. 5-2

where μ is the optical index. Note that Eq. 5-2 describes the small signal gain which saturates at high optical intensity. The unsaturated output is given by [2]

$$I_{output} \quad = \quad I_{in} e^{\gamma(v)z}$$
Eqn. 5-3

where I_{in} is the seed laser output intensity, z is along the waveguide toward the optical output coupler. Eq. 5-3 provides an estimate of the intrinsic efficiency, i.e, I_{output} divided by the input I_o integrated over the z-dimension of the gain region.

However, in reality, the unsaturated gain only occurs near the beginning of the waveguide where the amplified optical intensity is low. The gain will saturate at high optical intensity, that is, the optical intensity will not grow exponentially. Rather it will pick up the additional stimulated emitted photons along the way where the gain is saturated, just like that in an optical amplifier. For homogeneously broadened medium, the saturated gain is modeled by [3],

$$\gamma_{sat}(\nu, z) = \frac{\gamma(\nu)}{1 + \dfrac{I(z)}{I_{sat}}} \qquad \text{Eq. 5-4}$$

where I_{sat} is the saturating intensity which can be determined experimentally, $I(z)$ is the optical intensity at z. The gain expression in Eq. 5-4 replaces the unsaturated gain $\gamma(\nu)$ in the exponent on the right side of Eq. 5-3 in the output calculation:

$$\frac{\Delta I(z)}{\Delta z} = I(z)\gamma_{sat}(\nu, z) \qquad \text{Eq. 5-5}$$

with the initial boundary condition that $I(0) = I_{in}$. In the intrinsic efficiency estimation, the output intensity is calculated via Eq. 5-5 via an integration over z, then to obtain intrinsic efficiency, it is divided by (I_o multiplied by z). A more accurate calculation will involve a better estimate of n in Eq. 5-1 which gives:

$$n \quad = \quad I_o \tau_{sp} \frac{(1 - e^{-\alpha d})}{d} \qquad \qquad \text{Eq. 5-6}$$

where d is the thickness of the quantum well region.

Once the intrinsic efficiency is obtained, one can straightforwardly estimate the extrinsic efficiency by multiplying it with the input coupling factor, the residual waveguide loss factor, the output coupler's coupling efficiency and the loss in the fiber. This can be done easily in the dB scale (via addition in dB). Typical values for coupling loss between fiber and waveguide are 1-3dB depending on the geometries, and waveguide loss depends on the confinement factor.

5.3 Gain layer: absorbing IQWs and waveguide

In this section the gain layer, composed of two sublayers, the absorbing multiple intrastep quantum wells (IQWs) and waveguide, as shown in Figure 5-3, is explained in detail. First the reason for using a seed laser and waveguide geometry is discussed. Then in the subsections of this section the analysis of the two sublayers are presented. In particular, for the multiple-IQW absorbing layer the calculation for transparency condition, and for the waveguide the simulation of propagation and optical power distribution between the layers, are presented and discussed.
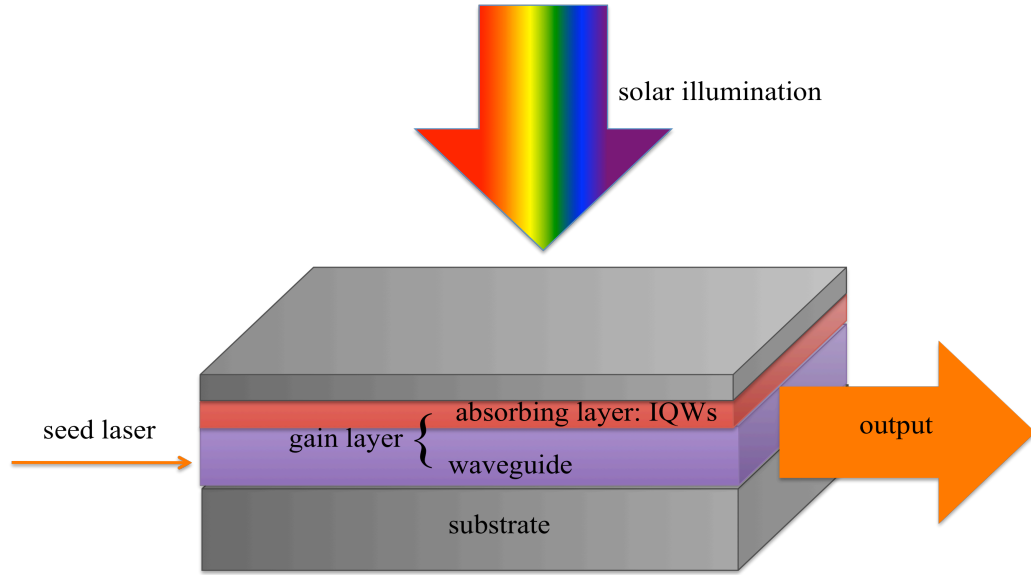
Figure 5-3   Illustration of the solar spectral condenser device showing the IQW and waveguide layers.

From the last section the solar spectral condenser converts broad spectrum sunlight into a narrow spectrum around wavelength λ_o (or frequency $v_o=c/\lambda_o$) output after undergoing two optical transitions shown in Figure 5-4: (1) an absorbing material with bandgap $E_g =hv_o$ absorb the photons with energy equal to or greater than E_g from the sun and convert them into electrons and holes that quickly lose their excess energy through thermalization and (2) these electrons and holes, which now are at E_c and E_v, respectively, recombine to make photons of wavelength λ_o that travel in the same spatial direction such that they can be collected by an optical fiber at the output. In order to realize these two optical transitions, the absorbing layer in Figure 5-3 is made of intrastep quantum wells (IQWs) of a certain energy band structure whose details are discussed later in 5.3.2. However, without a particular structure design the recombination in (2) is spontaneous recombination in which the photons

travel in all directions. In order to facilitate the photons created by optical transition (2) to travel in the same spatial direction, a seed laser is used.
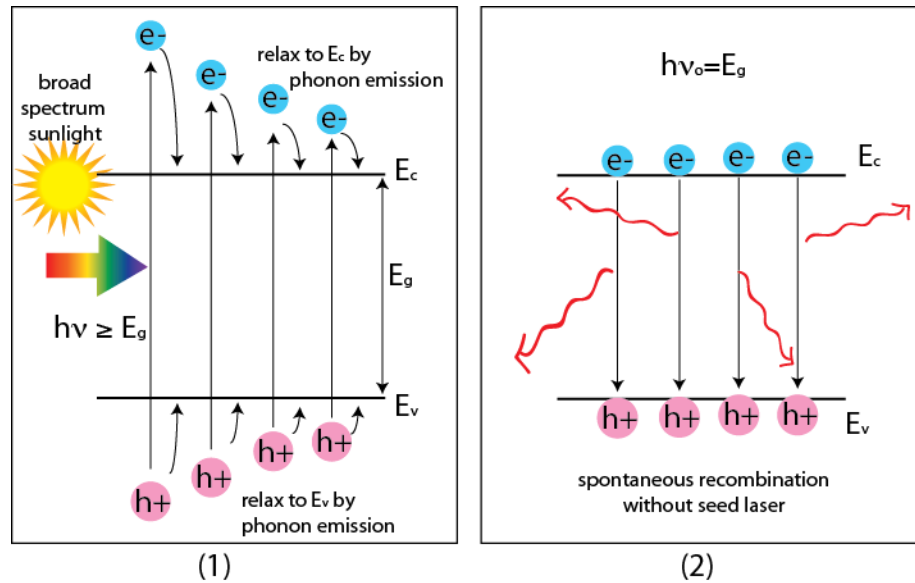
Figure 5-4   Optical transitions in solar spectral condenser.

5.3.1   Seed laser and waveguide

In principle, if the geometry of the device were a resonator, the device could behave as a laser, where the stimulated photons, having the same phase and momentum, resonate in the cavity until some escape from a small facet opening on one end of the device. The threshold for lasing of a resonator is dependent on the cavity length, reflection coefficients, number of wells, and geometry. However, pumping such a laser cavity with sunlight and wait for a few photons with the correct momentum to resonate is not the goal of the solar spectral condenser device. Rather, the goal is to harvest the solar power by collecting it out of the device as soon as it is

converted into the stimulated wavelength. If an external seed laser that is launched in the desired direction through the solar spectral condenser device, then once transparency is achieved any additional sunlight collected by generation of electron-hole pairs can be collected through stimulated emission. The seed laser then eliminates the need to optimize the device as a laser, but rather allows freedom to optimize as a solar power harvesting device.

The solar spectral condenser process can be jump-started in a straight-forward manner with an external seed source of coherent, unidirectional light, such as a laser signal launched from a fiber into a waveguide. This seed laser would have the same wavelength as the wavelength to be stimulated (i.e. the IQW optical transition wavelength). The "pumping" is done by concentrating the normally incident sunlight to greater than 16 suns (calculated later in Section 5.3.2) which inversely populates the energy levels in the IQW layer with electrons and holes, and when the mode of the guided optical wave of the seed laser overlaps with the IQW region, all of the photons generated by stimulated emission will also readily travel in the same direction without need for a resonating cavity. Thus the energy from the sun will be immediately collected out of the waveguide structure.

For this reason, the structure of the gain layer of the solar spectral condenser device must include a waveguide in close proximity with the multiple-IQW layer so that when photons from the seed laser are travelling through the waveguide, the electrons and holes in the IQWs can "see" the seed laser, thus emitting light by

stimulated emission process, and be guided out of the device, as shown in Figure 5-3. The combination of these two layers is the key to achieving gain. If a seed laser is launched into the waveguide without the solar illumination, its power will be coupled between the waveguide and IQW layers as it propagates across the device until it reaches the output with little loss with a waveguide properly designed. With solar illumination, and if transparency is achieved, the same seed laser passing through the IQW layer picks up the stimulated emission as it propagates through the waveguide. The result is an amplified version of the seed laser collected at the output.

5.3.2   Optical gain using intrastep quantum wells

As discussed above, solar spectral condenser contains a waveguide region and a gain region. In this subsection design of the gain medium using intrastep quantum wells (IQWs) is discussed. First, the band structure of IQWs is used to calculate the electron and hole wavefunctions to determine the optical transition energies as well as the overlap between electrons and holes. Then the optical gain threshold, in number of suns (assuming sunlight is concentrated) is calculated.

Since optical fibers are used to collect the energy from the solar spectral condenser device, a seed laser wavelength of 1310nm was selected for consideration, as it is a wavelength compatible with current optical fiber technology. The IQWs are designed with the following considerations:

- First-order optical transition should be around 1310nm.

- Overlap between electrons and holes is moderate such that the spontaneous recombination time is long and the stimulated recombination can occur within the time of recombination.

- The total thickness of the multiple-IQW layer is such that

  o There is sufficient volume for significant absorption of the incident sunlight.

  o An electric field via bias voltage can tune the IQWs for optimizing stimulated emission.

Figures 5-5 and 5-6 show the IQW structure designed to fulfill the requirements above. The Schrodinger equation was used to calculate the electron and hole energy levels and envelope wavefunctions.

Figure 5-5   Physical structure of intrastep quantum wells (IQWs) inside the solar spectral condenser as the gain layer. Figure shows one IQW with bandgap energies and optical index *n* at 1310nm for each layer. The full gain layer contains ten IQWs.

Flat band $\Delta E = E_{e1} - E_{hh1}$ 0.9599eV --> 1.292μm
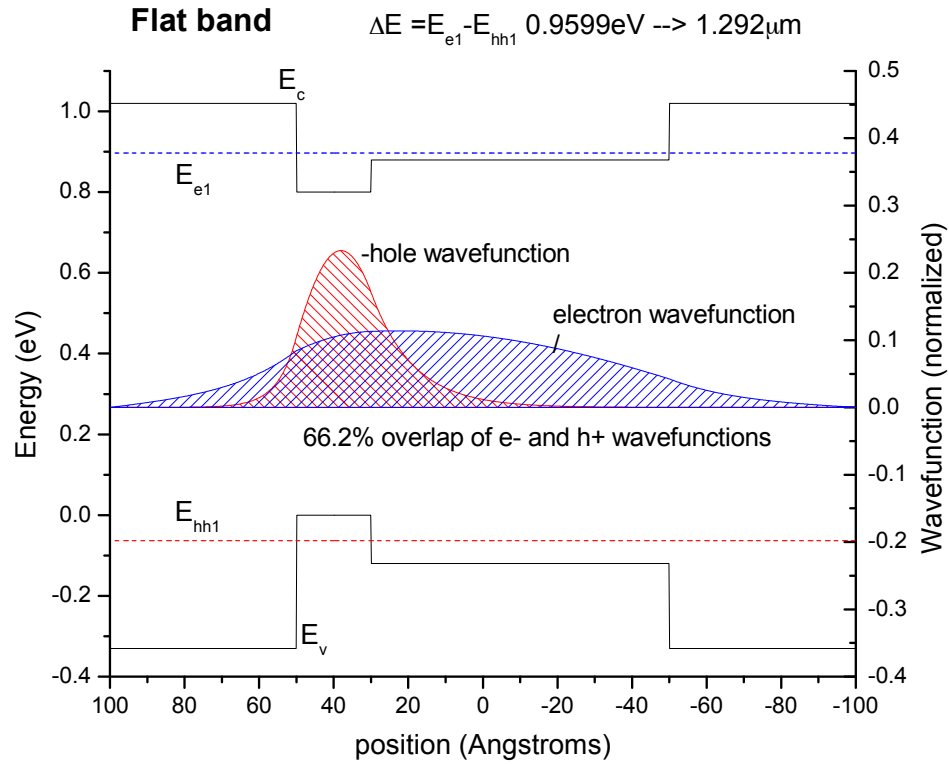
Figure 5-6   Flat band energy band diagram of IQW inside the solar spectral condenser gain layer. Calculated energy band diagram (versus space in Angstroms) of one IQW with conduction band E_c, valence band E_v, first electron level E_{e1}, first heavy hole level E_{hh1}, and their respective envelope wavefunctions shaded in to show overlap at flat band (i.e., forward bias in a *p-i-n* structure).

The overlap between the envelope wavefunctions was used to calculate the absorption spectrum of a single IQW. Appendix A contains the MATLAB code used to calculate the wavefunctions of the IQW structures. The calculations were based on a *p-i-n* structure where the *p-* and *n-* regions are heavily doped InP and the IQW is contained in the 200nm thick *i-*region, and for simplicity, the built-in voltage of the *p-i-n* structure is assumed to be 1.0V. The orientation of the IQW is such that the deeper well faces the *p*-region and the intra, or shallower well, faces the *n-* region, much like

the "flipped IQWSC" in Chapters 3 and 4, so that there can be "moderate" overlap. In this configuration, an applied bias voltage of +1.0V cancels out the 1.0V built-in voltage, resulting in zero E-field, or flat band, as in Figure 5-6. With a bias of zero there is 1.0V built-in voltage dropped on the 200nm *i*-layer, bending the IQW in Figure 5-6 such that the left side is raised. A bias voltage of -1.0V adds to the 1.0V built-in voltage, resulting in a large reverse E-field, bending the IQW even more. Figure 5-7 shows the absorption profile for one IQW with different applied voltages. It is assumed that this absorption is the same for all ten IQWs in the 200nm *i*-layer.
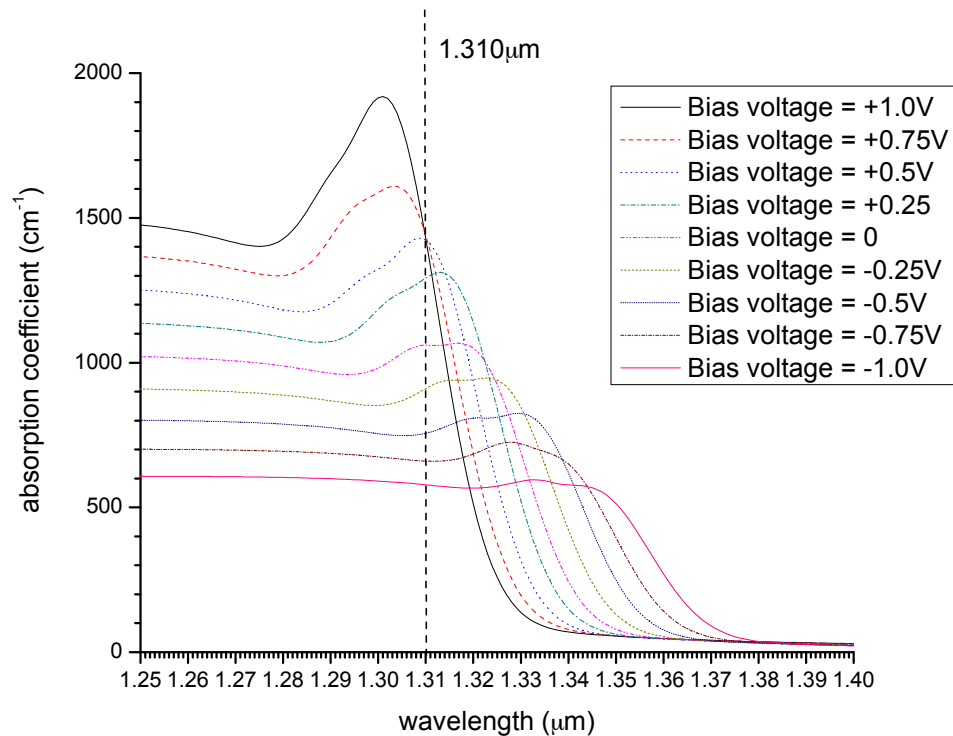
Figure 5-7   Calculated absorption spectrum of solar spectral condenser IQW. Absorption coefficient (cm^{-1}) of one of the IQWs versus wavelength (um) for different bias voltages, assuming a *p-i-n* structure were the 200nm *i*-layer containing the IQWs (as in Figures 5-5 and 5-6) and the *p* and *n* layers are heavily doped such that all of the electric field falls on the *i*-layer.

5.3.3   Optical transparency condition for IQW gain layer

In this subsection the condition for optical transparency, or population inversion, of a semiconductor material is calculated in detail using both Boltzmann and Fermi-Dirac distributions for modeling the carrier densities. The transparency condition by means of optical generation of carriers is calculated. Finally, this analysis is applied to the solar concentrator device to find the requirement for transparency in the multiple-IQW gain layer for the seed laser wavelength of 1310nm.

For a photon whose energy is greater than the bandgap of a material, the material is opaque to it, because it can be readily absorbed. However, if the electron states in the conduction band are completely occupied, then the photon cannot be absorbed, and the material is considered transparent to this photon. Transparency can be described by the following statement: The probability of an electron at state j to transition to state i is greater than the probability of an electron at state i to transition to state j, where state j is higher than state i, as shown in Figure 5-8.
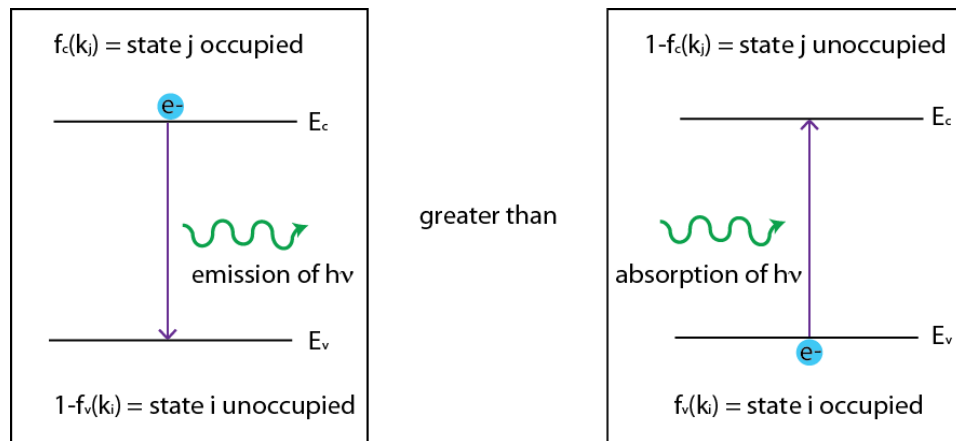
Figure 5-8   Illustration of the definition of transparency.

The requirement for transparency can be written as the following inequality:

$$f_c(k_j) \cdot [1 - f_v(k_i)] > f_v(k_i) \cdot [1 - f_c(k_j)]$$
Eq. 5-7

where $f_c(k) = \dfrac{1}{1 + e^{\frac{E(k) - E_{fn}}{k_B T}}}$ and $f_v(k) = \dfrac{1}{1 + e^{\frac{E(k) - E_{fp}}{k_B T}}}$
Eq. 5-8

where f_c and f_v are the probabilities of an electron occupying a state in the conduction and valence bands, respectively (and therefore $(1-f(k))$ can be described as an unoccupied state), and k_i and k_j are the wavenumbers associated with states i and j, as shown in Figure 5-8, describing the definition of transparency as the probability of photon emission is greater than the probability of absorption. Evaluating Eq. 5-7,

$$f_c(k_j) - f_c(k_j) \cdot f_v(k_i) > f_v(k_i) - f_v(k_i) \cdot f_c(k_j)$$
$$\Rightarrow f_c(k_j) > f_v(k_i)$$
Eq. 5-9

Substituting Eq. 5-8 into Eq. 5-9 and evaluating,

$$\frac{1}{1 + e^{\frac{E(k_j) - E_{fn}}{k_B T}}} > \frac{1}{1 + e^{\frac{E(k_i) - E_{fp}}{k_B T}}}$$

$$1 + e^{\frac{E(k_i) - E_{fp}}{k_B T}} > 1 + e^{\frac{E(k_j) - E_{fn}}{k_B T}}$$

$$e^{\frac{E(k_i) - E_{fp}}{k_B T}} > e^{\frac{E(k_j) - E_{fn}}{k_B T}}$$

$$e^{\frac{E(k_i) - E_{fp}}{k_B T}} \cdot e^{-\frac{E(k_j) - E_{fn}}{k_B T}} > 1$$

$$e^{\frac{E_{fn}-E_{fp}-(E(k_j)-E(k_i))}{k_B T}} > 1 \qquad\qquad \text{Eq. 5-10}$$

For light with energy $hv = E_c - E_v = E(k_j) - E(k_i)$, Eq. 5-10 becomes

$$e^{\frac{(E_{fn}-E_{fp})-hv}{k_B T}} > 1 \qquad\qquad \text{Eq. 5-11}$$

For the inequality in Eq. 5-11 to hold, the transparency condition is

$$E_{fn} - E_{fp} > hv \qquad\qquad \text{Eq. 5-12}$$

that is, the difference between the quasi-Fermi levels of the electrons and holes must be greater than the photon energy.

To evaluate the quasi-Fermi levels of electrons and holes, one could use either Boltzmann statistics or Fermi-Dirac statistics for the distribution of electrons and holes. Both calculations are done in this section, but it should be noted that the Fermi-Dirac distribution is more accurate in the case of degeneracy (i.e., non-degenerate case is when the Fermi level is at least a few kT (thermal energy) lower than the conduction or valence band) or high injection. In this case, the very nature of transparency is that the quasi-Fermi levels are greater than the conduction and valence levels (inferred from Eq. 5-12), so the Boltzmann distribution is not a reliable estimation.

Boltzman distribution

In Boltzmann statistics, the electron density n and the hole density p are

$$n = n_i e^{\frac{E_{fn} - E_i}{kT}} \quad \text{and} \quad p = n_i e^{\frac{E_i - E_{fp}}{kT}} \qquad \text{Eq. 5-13}$$

from which the quasi-Fermi levels E_{fn} and E_{fp} can then be evaluated as

$$E_{fn} = E_i + kT \ln(\frac{n}{n_i}) \quad \text{and} \quad E_{fp} = E_i - kT \ln(\frac{p}{n_i}) \qquad \text{Eq. 5-14}$$

Applying the transparency condition inequality Eq. 5-12,

$$E_{fn} - E_{fp} = kT \ln(\frac{np}{n_i^2}) > h\nu \qquad \text{Eq. 5-15}$$

The intrinsic carrier concentration n_i can be expressed as

$$n_i^2 = N_c N_v e^{-\frac{E_g}{kT}} \qquad \text{Eq. 5-16}$$

where N_c and N_v are the conduction and valence density of states, respectively, and E_g is the material energy band gap. Combining Eq. 5-15 and Eq. 5-16,

$$kT \ln\left(\frac{np}{N_c N_v e^{-\frac{E_g}{kT}}}\right) > h\nu \qquad\qquad \text{Eq. 5-17}$$

Further evaluating Eq. 5-17,

$$kT\left[\ln\left(\frac{np}{N_c N_v}\right) + \frac{E_g}{kT}\right] > h\nu$$

$$kT \ln\left(\frac{np}{N_c N_v}\right) > h\nu - E_g$$

$$np > N_c N_v e^{\frac{h\nu - E_g}{kT}} \qquad\qquad \text{Eq. 5-18}$$

For photons energy $h\nu$ equal to the material bandgap E_g, Eq. 5-18 becomes

$$np > N_c N_v \qquad\qquad \text{Eq. 5-19}$$

In other words, to achieve transparency (according to Eq. 5-12), using the Boltzmann distribution, the product of the number of carriers n and p must be greater than the product of the density of states N_c and N_v. For optical transitions, each photon generates one electron and one hole, so $n=p$. Therefore, required number of carriers generated to meet the transparency condition, n_{tr}, consistent with [3] can be written as:

$$n_{tr} = \sqrt{N_c N_v} \qquad\qquad \text{Eq. 5-20}$$

Fermi-Dirac distribution

An analytical expression using the Fermi-Dirac distribution is more complicated than the Boltzmann distribution. In Fermi-Dirac distribution the quasi-Fermi levels are related to the number of electrons and holes by the product of the density of states $\rho(E)$ and Fermi function $f(E)$,

$$n,p = \int \rho_{c,v} f_{c,v}(E, E_{fn,fp}) dE \qquad \text{Eq. 5-21}$$

where the 2D density of states (for quantum wells) goes as the Heaveside function H,

$$\rho_{c,v} = \frac{m_{c,v}}{\pi \hbar^2 L_z} \sum_i H(E - E_{ci, vi}) \qquad \text{Eq. 5-22}$$

for the first electron energy level e_1 and first heavy hold energy level hh_1,

$$\rho_c = \frac{m_e^*}{\pi \hbar^2 L_z} \qquad \text{Eq. 5-23}$$

$$\rho_v = \frac{m_{hh}^*}{\pi \hbar^2 L_z} \qquad \text{Eq. 5-24}$$

and the Fermi function is

$$f_{c,v} = \frac{1}{1 + e^{\frac{E - E_{fn,fp}}{kT}}}$$

Eq. 5-25

The Fermi-Dirac distribution in Eq. 5-21 is evaluated as follows:

$$n = \frac{m_e^*}{\pi\hbar^2 L_z} \int_{E_{e1}}^{\infty} \frac{1}{1 + e^{\frac{E - E_{fn}}{kT}}} dE$$

$$n = \frac{m_e^*}{\pi\hbar^2 L_z} \int_{E_{e1}}^{\infty} \frac{1}{1 + e^{\frac{E - E_{fn}}{kT}}} \cdot \frac{e^{-\frac{E - E_{fn}}{kT}}}{e^{-\frac{E - E_{fn}}{kT}}} dE$$

$$n = \frac{m_e^*}{\pi\hbar^2 L_z} \int_{E_{e1}}^{\infty} \frac{e^{-\frac{E - E_{fn}}{kT}}}{1 + e^{-\frac{E - E_{fn}}{kT}}} dE$$

Eq. 5-26

Using the following substitution,

$$u = 1 + e^{-\frac{E - E_{fn}}{kT}}$$

$$-kTdu = e^{-\frac{E - E_{fn}}{kT}} dE$$

Eq. 5-27

the integral in Eq. 5-26 can be evaluated:

$$n = \frac{m_e^*}{\pi\hbar^2 L_z} \int\limits_{E_{e1}}^{\infty} \frac{-kTdu}{u}$$

$$n = -\frac{m_e^* kT}{\pi\hbar^2 L_z} \ln u \Big|_{E_{e1}}^{\infty}$$

$$n = -\frac{m_e^* kT}{\pi\hbar^2 L_z} \ln(1 + e^{-\frac{E - E_{fn}}{kT}}) \Bigg|_{E_{e1}}^{\infty}$$

$$n = -\frac{m_e^* kT}{\pi\hbar^2 L_z} [\ln(1 + e^{-\frac{\infty - E_{fn}}{kT}}) - \ln(1 + e^{-\frac{E_{e1} - E_{fn}}{kT}})]$$

$$n = \frac{m_e^* kT}{\pi\hbar^2 L_z} \ln(1 + e^{\frac{E_{fn} - E_{e1}}{kT}})$$

Since $N_c = \frac{m_e^* kT}{\pi\hbar^2 L_z}$, an expression for n is

$$n = N_c \ln(1 + e^{\frac{E_{fn} - E_{e1}}{kT}}) \qquad\qquad \text{Eq. 5-28}$$

A similar analysis could be done for p,

$$p = N_v \ln(1 + e^{\frac{E_{hh1} - E_{fp}}{kT}}) \qquad\qquad \text{Eq. 5-29}$$

Next Eq. 5-28 and 29 are each evaluated to isolate E_{fn} and E_{fp}.

$$n = N_c \ln(1 + e^{\frac{E_{fn} - E_{e1}}{kT}})$$

$$\frac{n}{N_c} = \ln(1 + e^{\frac{E_{fn} - E_{e1}}{kT}})$$

$$e^{n/N_c} = 1 + e^{\frac{E_{fn} - E_{e1}}{kT}}$$

$$e^{n/N_c} - 1 = e^{\frac{E_{fn} - E_{e1}}{kT}}$$

$$\ln(e^{n/N_c} - 1) = \frac{E_{fn} - E_{e1}}{kT}$$

$$kT \ln(e^{n/N_c} - 1) = E_{fn} - E_{e1}$$

$$E_{fn} = E_{e1} + kT \ln(e^{n/N_c} - 1) \qquad\qquad \text{Eq. 5-30}$$

And similarly for E_{fp},

$$E_{fp} = E_{hh1} - kT \ln(e^{p/N_v} - 1) \qquad\qquad \text{Eq. 5-31}$$

Now Eq. 5-30 and 31 can be substituted in the transparency requirement of Eq. 5-12,

$$E_{fn} - E_{fp} > h\nu$$

$$E_{e1} + kT \ln(e^{n/N_c} - 1) - E_{hh1} + kT \ln(e^{p/N_v} - 1) > h\nu$$

$$kT[\ln(e^{n/N_c} - 1) + \ln(e^{p/N_v} - 1)] > h\nu - (E_{e1} - E_{hh1})$$

For $h\nu = (E_{e1} - E_{hh1})$,

$$\ln(e^{n/N_c} - 1) + \ln(e^{p/N_v} - 1) > 0$$

$$\ln(e^{n/N_c} - 1) > -\ln(e^{p/N_v} - 1)$$

$$\ln(e^{n/N_c} - 1) > \ln(\frac{1}{e^{p/N_v} - 1})$$

So that the requirement for transparency becomes

$$(e^{n/N_c} - 1)(e^{p/N_v} - 1) > 1 \qquad \text{Eq. 5-32}$$

For charge neutrality, $n = p$, therefore, Eq. 5-32 becomes

$$(e^{n/N_c} - 1)(e^{n/N_v} - 1) > 1 \qquad \text{Eq. 5-33}$$

which can be further evaluated,

$$e^{n/N_c} e^{n/N_v} - e^{n/N_c} - e^{n/N_v} + 1 > 1$$

$$e^{n/N_c} e^{n/N_v} > e^{n/N_c} + e^{n/N_v}$$

$$1 > e^{-n/N_c} + e^{-n/N_v} \qquad \text{Eq. 5-34}$$

The relationship between the density of states can be used

$$N_v = \frac{m^*_{hh}}{m^*_e} N_c \qquad \text{Eq. 5-35}$$

Finally, the transparency requirement,

$$1 > e^{-n/N_c} + e^{-n \cdot m_e^* / m_{hh}^* \cdot N_c}$$

Eq. 5-36

can be solved graphically as in Figure 5-9.

$$y - \text{axis}: \ e^{-n/N_c} + e^{-nm_e^*/m_{hh}^*N_c}$$
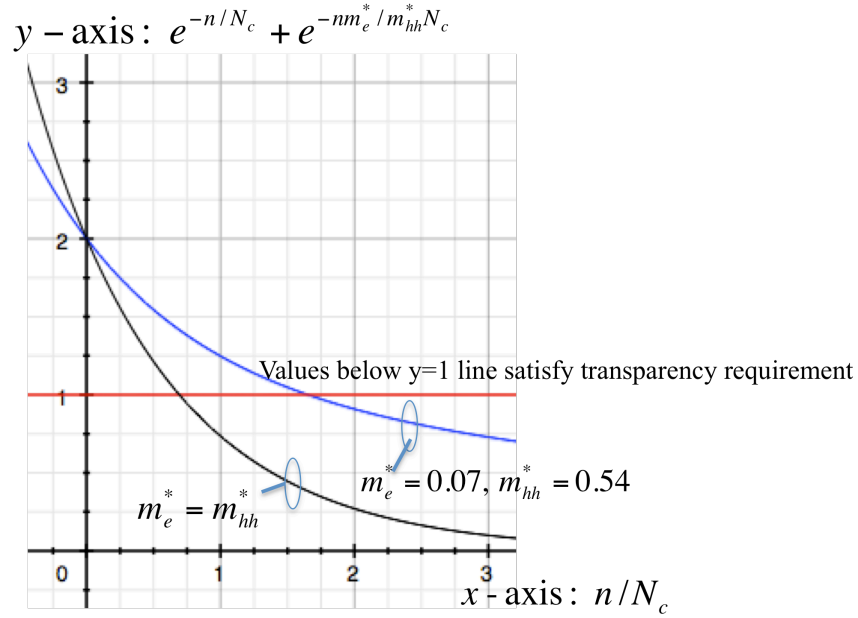
Figure 5-9   Graphical solution of transparency requirement using Fermi-Dirac distribution. The y-axis is the RHS of the inequality in Eq. 5-36, plotted against the x-axis, n/N_c, a term in the exponential part of the expression. Two lines for different effective masses m_e^* and m_{hh}^* are shown. The line $y=1$ represents the LHS of Eq. 5-36. The x-value at which the lines cross $y=1$ is the transparency requirement n_{tr}. I.e., for $m_e^*=0.07$ and $m_{hh}^*= 0.54$, $n_{tr} = 1.65N_c$, and for $m_e^* = m_{hh}^*$, $n_{tr}=0.7N_c$.

From the detailed derivation above, which are consistent with [5] and [6], if Fermi-Dirac statistics are used for the calculation, the transparency condition from Figure 5-9 for $m_e^*=0.07$ and $m_{hh}^*= 0.54$ is

$$n_{tr} = 1.65 N_c \qquad\qquad \text{Eq. 5-37}$$

where n_{tr} is the number of carriers required for transparency and N_c is the effective density of states in the conduction band.

Given the solar spectrum of AM1.5g (shown in Chapter 2), and the absorption spectrum of the IQW layer, similar to Eq. 5-6, the number of carriers generated by absorption of one sun n_{1sun} is

$$n_{1sun} = \int_{930nm}^{1310nm} I_{1sun}(\lambda)\tau_{sp} \frac{(1 - e^{-\alpha(\lambda)d})}{d} d\lambda \qquad\qquad \text{Eq. 5-38}$$

where $I_{1sun}(\lambda)$ is the intensity from one sun, τ_{sp} is the spontaneous recombination time, $\alpha(\lambda)$ is the absorption coefficient, and d is the thickness of the absorbing material. The integral is done for wavelengths from 930nm to 1310nm, because most of the sunlight with wavelength shorter than 930nm are absorbed by the p-InP cap layer, and the wavelengths longer than 1310nm cannot be absorbed by the IQWs. At 1 sun illumination, transparency has not been reached for 1310nm, so it is assumed that all light with wavelengths shorter than 1310nm are absorbed. Using τ_{sp} = 1 ns and d = 200nm, then $n_{1sun} = 7.736 \times 10^{22} \text{m}^{-3}$. Figure 5-10 shows the number of carriers generated per wavelength, i.e., Eq. 5-38 before integrating.
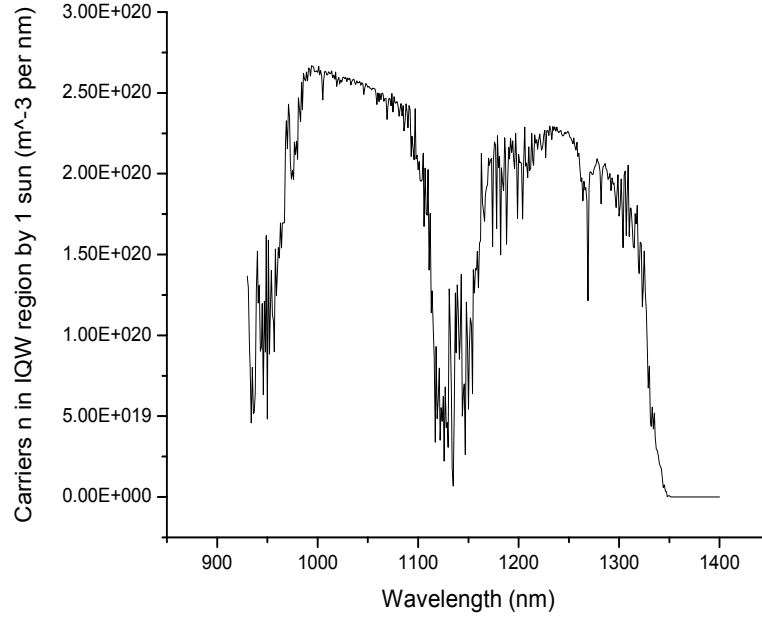
Figure 5-10   Calculated carriers generated by absorption of solar energy from 1 sun (AM1.5g) in IQW layer.   Assumes 200nm IQW layer and 1ns spontaneous recombination time. Integrating the curve gives the total number of generated carriers.

Assuming that for concentration of sunlight just below transparency level the IQWs are fully absorbing the light with wavelengths between 930nm and 1310nm, and the number of carriers generated is proportional to the number of photons, then the number of suns S required for transparency can be approximated as

$$S = \frac{n_{tr}}{n_{1sun}}$$

Eq. 5-39

Therefore, from Eq. 5-37, 38, and 39, and the parameters mentioned above, the number of suns required for transparency for the multiple-IQW layer is 16 suns.

5.3.4   Simulation of propagation through a slab waveguide

In the previous section the requirements of one of the two inputs of the solar spectral condenser device, the solar illumination from above the device, were found by calculating that the condition for transparency or population inversion in the IQWs can be achieved by pumping optically with about 16 suns. In this subsection the second input of the solar spectral condenser, the seed laser, is discussed with the simulation of the seed laser beam propagating through the slab waveguide underneath the absorbing multiple-IQW layer.

The index of refraction and thickness of the waveguide structure were designed to optimize the coupling between the multiple-IQW layers and the waveguide. Simulations were done in Beamprop to determine the optimal specifications. Figure 5-11 shows (a) the cross-section of the waveguide structure and (b) the top-view (x-z plane) of the beam propagation through the waveguide and the power in each layer normalized to the input power. The input light is a 1.31um wavelength Gaussian beam with a ~9um mode field diameter, which is approximately the mode of light coming out of a cleaved single-mode fiber immediately before being coupled into the slab waveguide, and its center is placed at the middle of the waveguide layer.
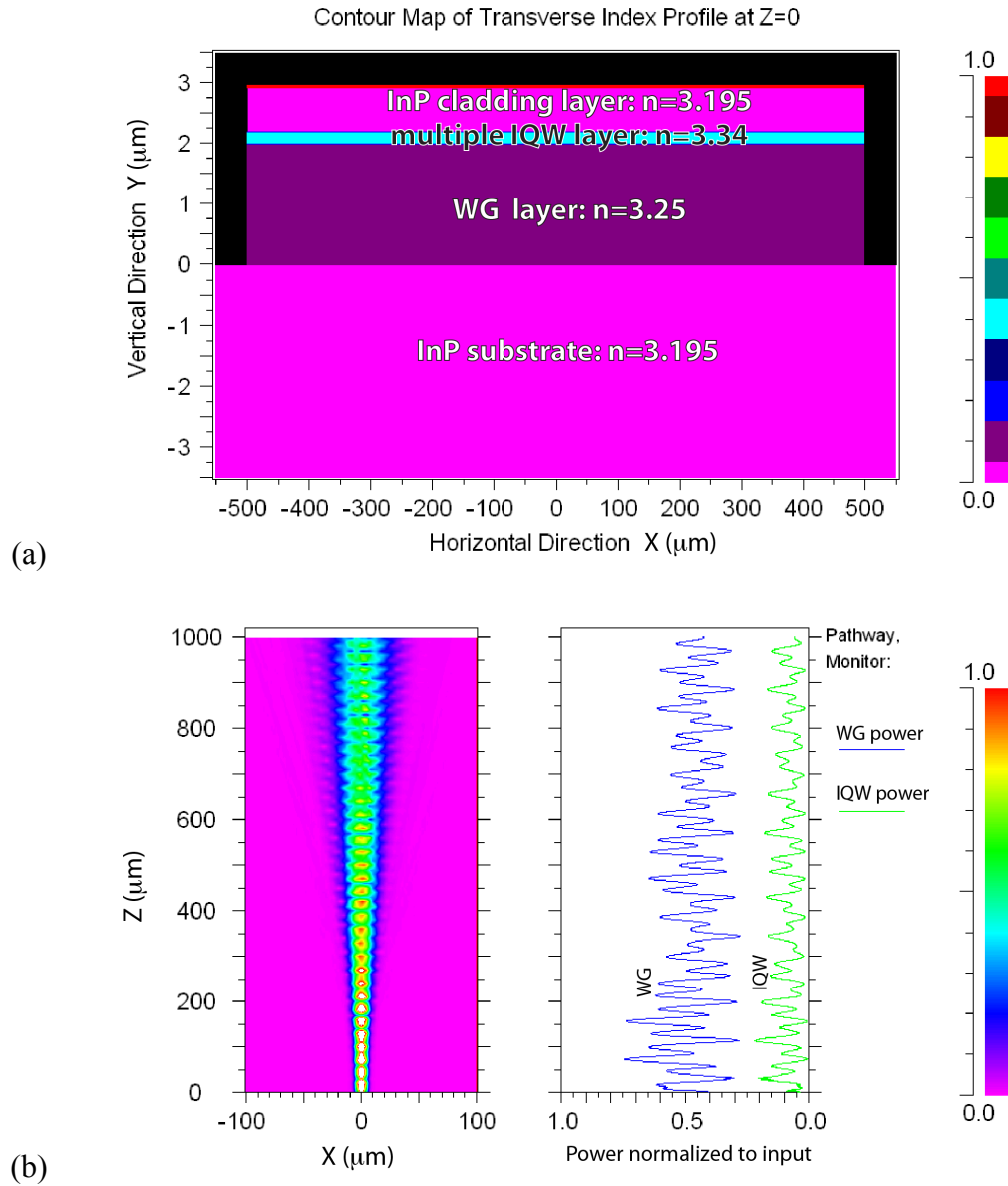
Figure 5-11   Beamprop simulation results of solar spectral condenser waveguide and IQW layers. (a) Waveguide structure cross-section and (b) propagation simulation with 9um diameter Gaussian input showing the lateral mode spreading (left) and power in each layer (right).

From Figure 5-11 (b), the coupling between the two layers is good, because there is a periodic exchange of power between the two layers. On average, about 50% of the input power is in the waveguide, and about 10% of the input power is in the

IQW layer. However, about 40% of the power is no coupled, mostly because the input beam, 9um in diameter, is very large compared to the 2um thick waveguide.

Figure 5-12 shows another simulation made using an input beam as a circular 2um diameter Gaussian beam, which is the beam coming out of a conically lensed single-mode fiber. It can be seen in this case that the seed beam spreads out very quickly laterally in the waveguide, because the beam started out as a very small point. This can be detrimental to the solar spectral condenser device, because (1) the output power cannot be fully coupled to any fiber due to the angle of spread, and (2) for the purpose of the proof-of-concept measurement, allowing the power to spread out too much could result in less amplification.
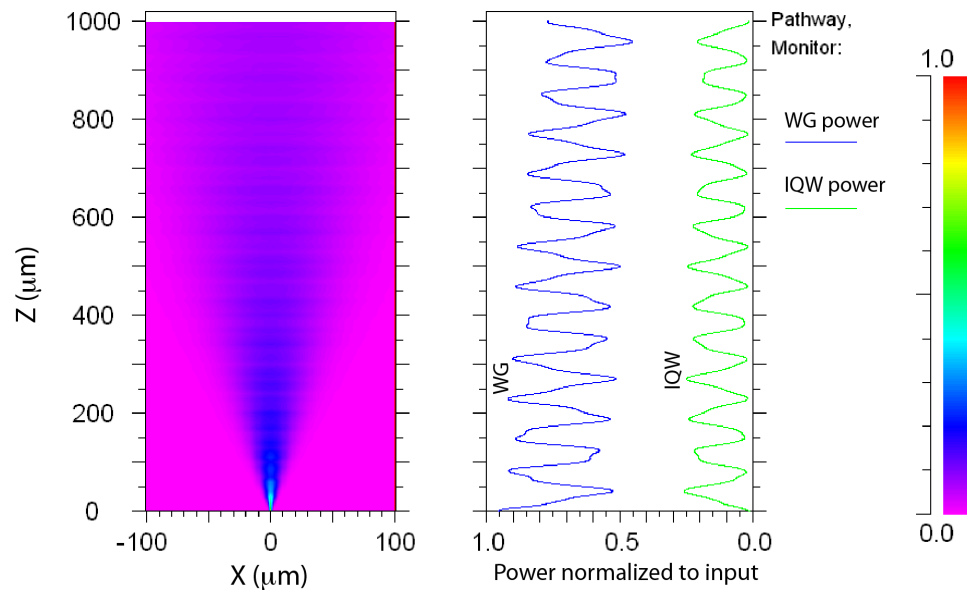
Figure 5-12   Beamprop simulation results of solar spectral condenser with circular 2um diameter Gaussian input (representing a conically lensed fiber input), showing the lateral mode spreading (left) and power in each layer (right).

5.4   Summary of solar spectral condenser theory

From the calculation of the transparency condition and the simulation of beam propagation in the waveguide structure some conclusions can be drawn in consideration for the design and fabrication of the device and required measurement setup. First, an estimation of approximately 16 suns incident on the IQW device is required for transparency at 1310nm. This is an estimation that includes the loss from absorption of the top InP layer, but it does not take into account losses due to reflections and absorption of any other layers of the device such as the passivation layer (usually SiO_2 or SiN_x) and the mostly transparent indium-tin-oxide (ITO) conducting layer (which will be discussed in the next chapter on experimental details). Therefore, it is very possible that the absorbing multiple-IQW layer requires more than 16 suns for transparency, so a strong concentration system of lenses would be necessary for the measurement of the device.

The second conclusion from this chapter is that the coupling of the seed laser is very much dependent on the type of optical fiber at the input. For a cleaved single mode fiber, which is modeled by a Gaussian beam with 9μm diameter, much of the power is not coupled due to the fact that 9μm is much larger than the waveguide thickness of 2μm. For a conically lensed fiber whose output beam is approximately 2μm diameter Gaussian beam, the power spreads out laterally due to the small beam waist. In the next chapter a wedge or cylindrical lensed fiber is used during the actual experiment for better coupling into the solar spectral condenser device.

5.5 References

[1]   W. S. C. Chang, <u>Principles of Lasers and Optics</u>, Cambridge University Press, p. 203 (2005).

[2]   W. S. C. Chang, <u>Principles of Lasers and Optics</u>, Cambridge University Press, p. 198 (2005).

[3]   W. S. C. Chang, <u>Principles of Lasers and Optics</u>, Cambridge University Press, p. 172 (2005).

[4]   T. Numai, <u>Fundamentals of Semiconductor Lasers</u>, Springer, pp. 191-2 (2004).

[5]   P. Zory, <u>Quantum Well Lasers</u>, Academic Press, pp. 192-6 (1993).

[6]   S. L. Chuang, <u>Physics of Optoelectronic Devices</u>, Wiley, pp. 428-30 (1995).

Chapter 6

Experimental Results for Solar Spectral Condenser

6.1 Introduction

The solar spectral condenser device, designed according to the considerations in Chapter 5, was grown by MOCVD by a commercial vendor and fabricated in the Nano3 cleanroom facilities at UCSD. Individual devices were then cleaved and mounted on a copper submount for measurement. The solar spectral condenser was measured by coupling a constant laser source into one facet of the waveguide as the seed laser and by illuminating the chip area from above with a solar simulator and concentrating lens while measuring the output end of the waveguide. The output was measured for different bias voltages and different solar concentrations.

6.2 Wafer structure

The solar spectral condenser material structure was grown on a 2-inch n-InP wafers by MOCVD by a commercial vendor called TEC-Well (Taiwan), as shown in

Figure 6-1(a) with the layer details including thicknesses, materials, bandgaps, and dopings. Figure 6-1(b) shows the optical index profile n at 1.32um wavelength of the layers lined up with the layers in 6-1(a). For instance, n=3.195, 3.25, 3.34 for InP, the waveguide InGaAsP layer, and IQW layer, respectively. The n for the IQW layer was calculated by weight-averaging the three different materials within the IQW layer. InGaAs absorbs 1.32um wavelength light.

(a)

(b)
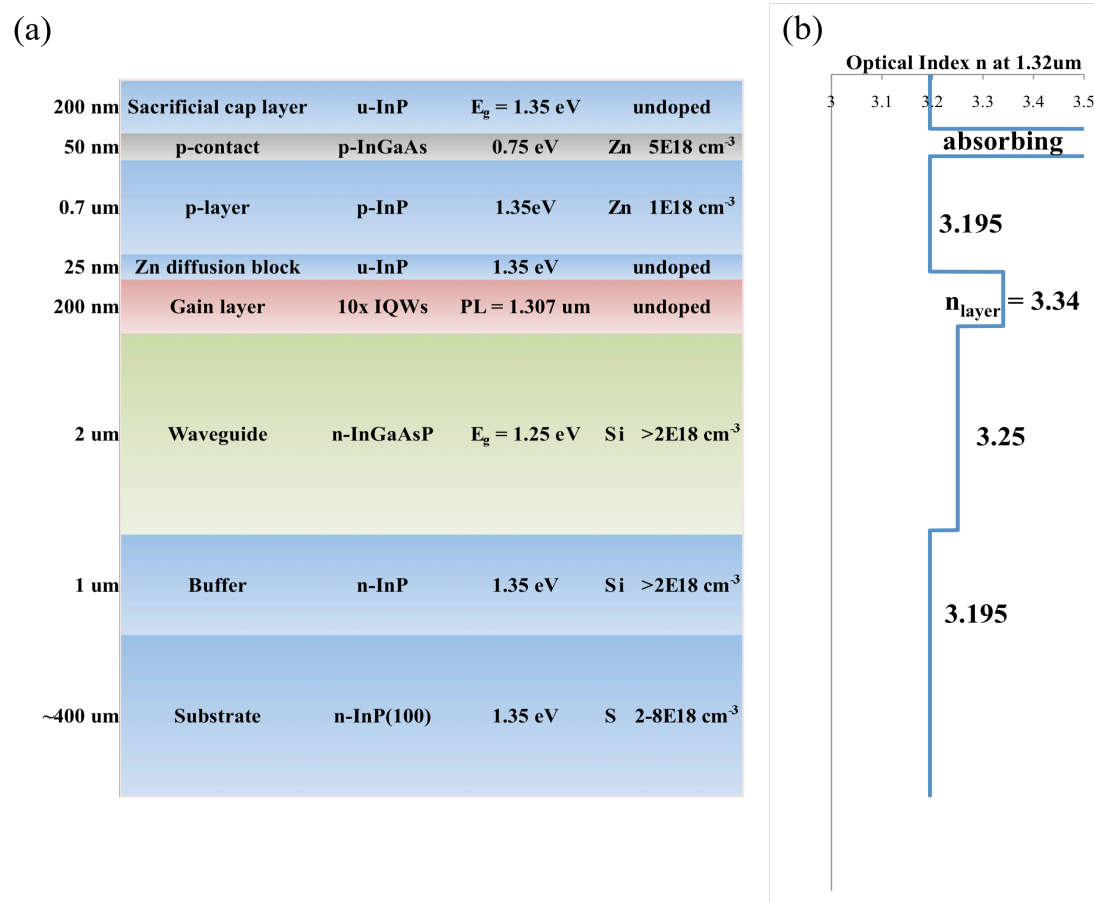
Figure 6-1   Solar spectral condenser layer structure and optical index profile. (a) Solar spectral condenser layer structure on n-InP(100) substrate as grown by MOCVD at TEC-Well. n=n-type, p=p-type, u=undoped. Energies in eV specify the energy bandgap of the quaternary $In_{1-x}Ga_xAs_yP_{1-y}$ alloy lattice matched to InP. The 200nm Gain layer contains 10 IQWs described in the previous section. (b) Optical index n at 1.32um refers to the optical index of the layer at 1.32um wavelength.

The top 200nm sacrifical cap layer of undoped InP is to prevent diffusion of Zn (*p*-dopant) in the contact layers back into the lower *i*-layers during cooling down of the MOCVD reactor at the end of the growth (which usually occurs around 650°C) as well as to protect the entire surface of the wafer during shipping and handling prior to processing. The 50nm *p*+InGaAs is for better Ohmic contact with the metal to be deposited on the top. It is designed to be as thin as possible such that the InGaAs would not absorb too much of the solar spectrum or the seed laser of 1.32um. The 700nm *p*-InP layer acts as a cladding layer for the slab waveguide, and the 25nm undoped InP is a buffer for Zn diffusion into the deeper *i*-layers during growth (growth was done from bottom to top).

The 200nm gain (and absorbing) layer contains ten undoped IQWs whose overall bandgap wavelength, measured by PL, is 1.307um, which is near 1.31-1.32um. The total *i*-layer, including the Zn diffusion block, is about 225nm thick such that a bias voltage applied (if necessary for tuning the bandgap wavelength of the IQWs by the Quantum-confined Stark effect) on the *p* and *n* terminals applies most of the electric field on this region (as described previously in Figure 5-7). Without applying any bias, the *p-i-n* structure has a built-in electric field, but applying a bias will change both the amount of overlap of electron and hole wavefunctions as well as the peak wavelength. In addition to applying a bias, the *p* and *n* terminals are used to monitor the photocurrent during the optical measurement.

The 2um slab waveguide underneath contains *n*-InGaAsP lattice-matched to InP with E_g=1.25eV and optical index n=3.25 at 1.32um, which was selected for optimal optical coupling between the waveguide and gain layers when the seed laser signal propagates through the slab waveguide. Underneath, the 1um *n*-InP buffer layer, the first layer grown on the *n*-InP substrate, acts as the bottom cladding. X-ray diffraction (XRD) and room-temperature photoluminescence (PL) measurements were done by TEC-well to verify the growth within the specifications.

6.2.1   X-ray diffraction assessment of wafer structure

The rocking curve XRD measurement (Figure 6-2) in which high resolution XRD is measured around the substrate peak for a range a few degrees ($1^o = 3600$" or 3600 arcseconds) can be used to determine superlattice period thickness Λ, by the Fourier transform of the X-ray spectrum:

$$\Lambda = \frac{\frac{1}{2}\lambda_{xray}}{\sin(\theta_{sub}) - \sin(\theta_{sub} - \Delta\omega_{avg})}$$

Eq. 6-1

where λ_{xray} is the x-ray wavelength, θ_{sub} is the substrate peak angle, $\Delta\omega_{avg}$ is the average angular separation between satellite peaks. The InP (004) substrate peak is 31.668^o and the Cu K-α x-ray wavelength is 1.518Å. In Figure 6-2, $\Delta\omega_{avg}$=914.5", corresponding to Λ=200.9Å, very close to the expected period of the IQW layer is 20nm, from the design and analysis for the IQWs in Chapter 5 (Figure 5-5).

XRD rocking curve for Tec-well

7.2"/step, 4s/step

$\lambda_{xray} = 1.518\overset{\circ}{A}$

$\theta_{InP} = 31.668^{\circ}$
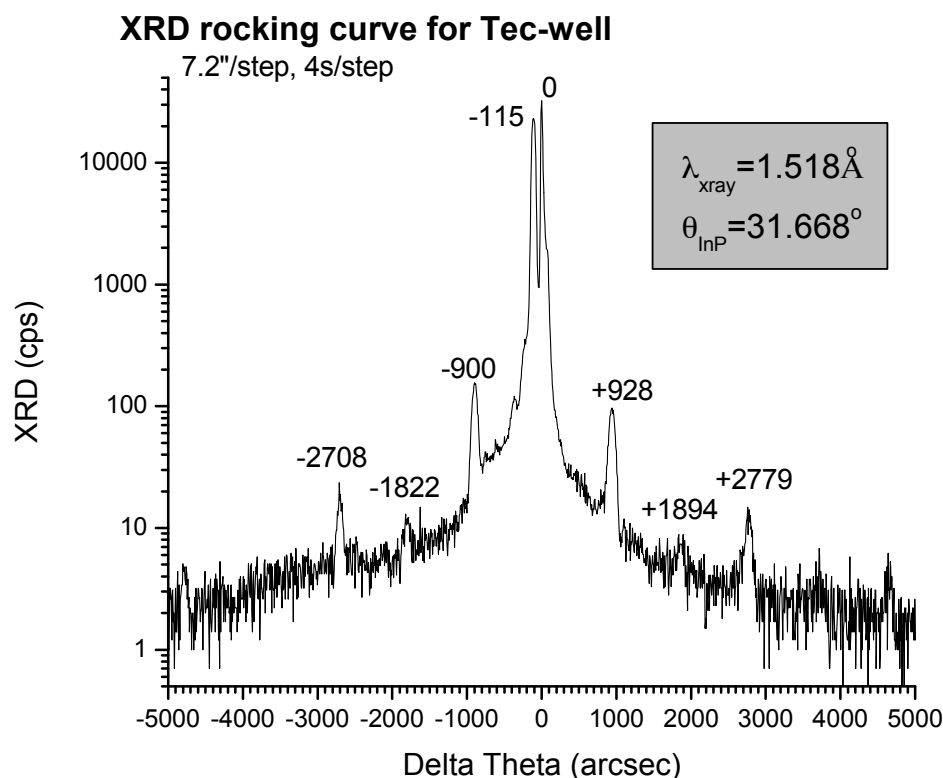
Figure 6-2   XRD rocking curve data for TEC-Well wafer.

6.2.2   Photoluminescence assessment of wafer structure

The room temperature PL measurement (Figure 6-3), in which a chopped-signal medium-intensity laser with wavelength greater than that of the material's bandgap wavelength (in this case, a 10mW 532nm green laser) is illuminated on and absorbed by the sample to create electron-hole pairs which spontaneously recombine and emit photons isotropically with energy distributed around the bandgap energy of the material.   These emitted photons are collected through optical lenses and their spectrum is measured by a system containing a monochromator, broad-band

photodetector (in this case, an InGaAs photodetector), and amplifier locked-in to the chopping frequency. The monochromator scans through a certain wavelength range, in this case, from 894nm to 1526nm, while a signal is measured by the photodetector. Usually the strongest signals from a PL measurement come from the lowest bandgap layers in the structure. In this case, if the top p+InGaAs layer is etched away, the IQWs have the lowest E_g. Thus the measured PL peak shown in Figure 6-3, 1307.7nm, is the overall bandgap of the multi-IQW layer. The somewhat large bandwidth of 133.2nm is most likely due to smearing of the quantum levels from having multiple quantum wells and intra-levels inside the wells.
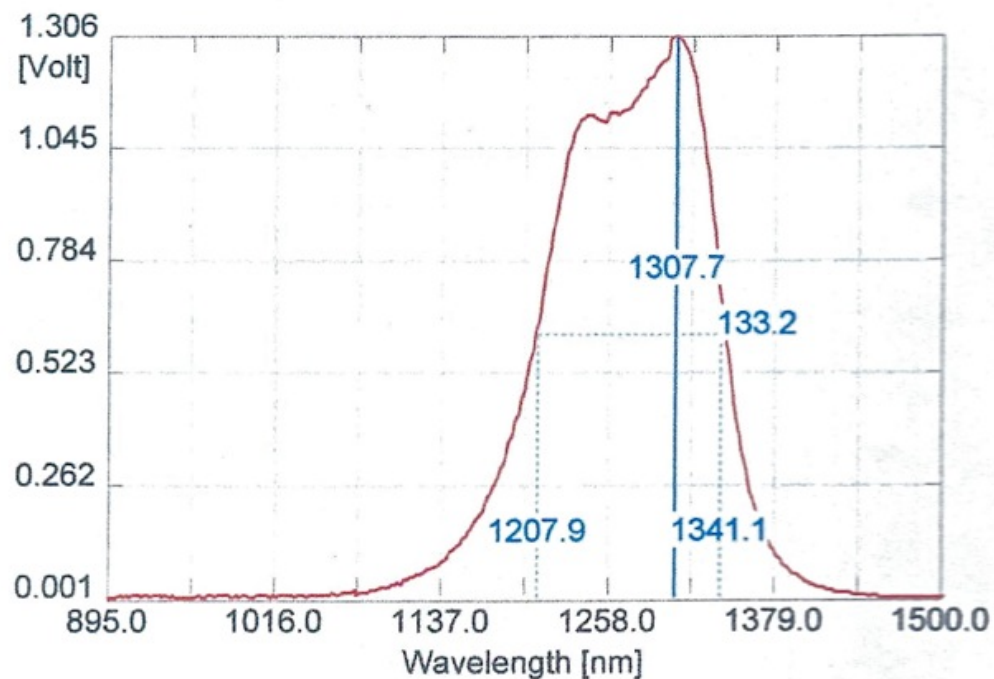
Figure 6-3   Measured room-temperature photoluminescence (PL) spectrum of solar spectral condenser wafer as-grown. PL peak = 1307.7nm, which is attributed to the IQW layer.

6.3   Solar spectral condenser device fabrication

The 2-inch wafers with MOCVD-grown layers were cleaved into approximately 12mm by 12mm pieces and then fabricated into devices by applying metal contacts and etching isolation mesas in the UCSD Nano3 cleanroom facility. Figure 6-4 shows the fabrication flowchart.

First the 12mm by 12mm pieces were cleaned with solvents and then rinsed with D.I. water. Then the top sacrificial 200nm InP layer was etched with $HCl:H_3PO_4$ 1:2 solution for 5s, exposing the p+InGaAs layer, indicated by an observable change in surface color. Next Ti/Pd/Au n-metal (100um squares with 2um mesh connecting six of the squares, shown in later figures) was patterned by photolithography, e-beam evaporation, and lift-off in acetone. Then 100nm of optically transparent, electrically conductive indium-tin-oxide (ITO) was sputtered and 1mm square mesas were formed by photolithography and wet etching with buffered oxide etch (BOE). Then another photolithography step was done to pattern 1mm squares for wet etching of the top p-layers (p+InGaAs and p-InP) for electrical isolation of the mesa. Then the wafers were taken outside of the cleanroom to be mechanically lapped down with silica powder from approximately 450um to 150um thickness, and roughly polished on lapped backside. Finally, the wafers were taken back into the cleanroom for backside n-metal deposition by e-beam evaporation of Ti/Pd/Au over the entire back surface.

1. Wafer is cleaned with acetone, methanol, isoproanol, and DI water. Then InP sacrifical layer is etched with 1HCl:2H₃PO₄ solution for 5s.

50nm p+InGaAs

200nm InP sacrificial layer

Other layers, substrate ~400um total thickness

wafer from vendor

2. Top p-metal Ti/Pd/Au is patterned by photolithography, e-beam evapora-tion, and metal lift-off.

Metal (Ti/Pd/Au)

3. 100nm ITO (indium-tin-oxide) is sputtered over entire surface of the wafer. ITO was patterned into 1mm by 1mm squares by photolithography and wet etching with BOE for 10s.

ITO

1mm ITO mesa

4. Photolithography and wet etching of 50nm p+InGaAs (1H₃PO₄:1H₂O₂:38H₂O) and 725nm InP (1HCl:2H₃PO₄) were done to create 1mm by 1mm square mesas.

1mm mesa

5. Wafer is lapped down to ~150um thickness with abrasive silica powder, then roughly polished.

6. Ti/Pd/Au n-metal is deposited on entire backside by e-beam evaporation.

Metal (Ti/Pd/Au)

Figure 6-4   Solar spectral condenser fabrication steps.

Next, the input and output facets for the slab waveguides were cleaved. In order to obtain smooth, flat facets, the wafer was scribed on the front side very slightly

(<1mm long scribe) and close to the edge of the wafer. The scribing was done by the Disco Automatic Dicing Saw (DAD) 3220 with a rotating diamond saw with a 30um blade used to achieve ~50um wide cut (Figure 6-5). The wafer was secured on an adhesive sheet and mounted in the DAD 3220 to be scribed. Since the rotating diamond saw is very large compared to the sample, and a very short scribe of <1mm is required, the cut was made at about 5mm away from the wafer. In this way the diamond saw was able to achieve a V-groove shaped scribe mark at the edge of the wafer. One scribe mark was done at each device mesa on one edge of the fabricated wafer so that "bars" of one row of mesas would result from cleaving (Figure 6-6).
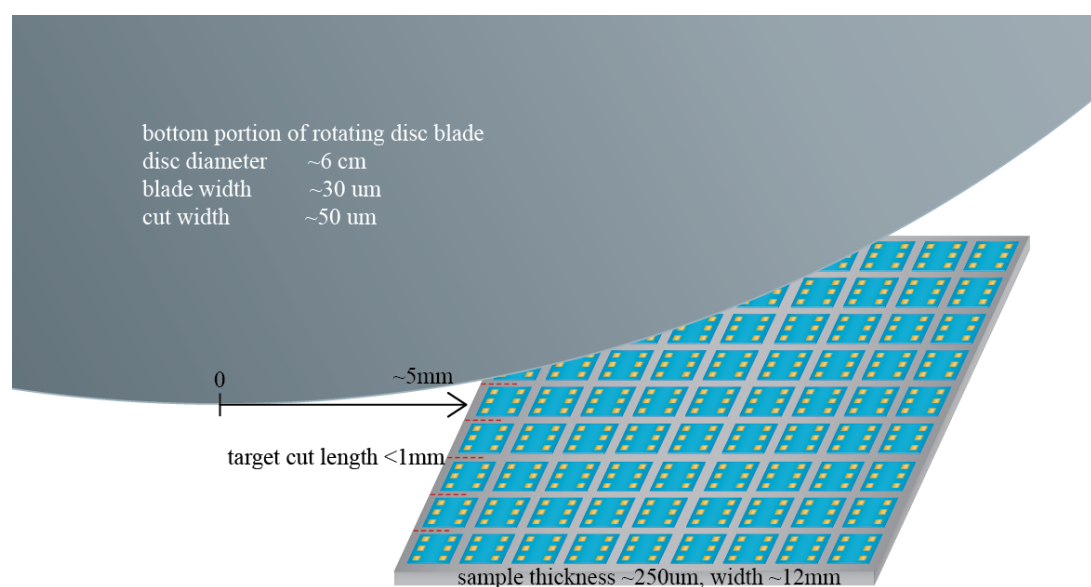
Figure 6-5   Schematic drawing rotating diamond saw used to scribe solar spectral condenser sample after fabrication. Drawing helps to visualize the relative size of the blade and sample. Since the disc is so large (6cm in diameter) compared to the target cut length of <1mm, for a sample with 250um thickness, the blade cuts the sample when the center bottom of the disc is at about 5mm away from the edge of the sample where the cut is made.

The scribed wafers were still attached to the adhesive sheet during cleaving, which was done by hand under a 50x microscope using a triangular shaped (for high

precision) No. 11 surgical scalpel. The wafers on the adhesive sheet was placed under the microscope face down on a cleanroom paper. The dicing marks were visible through the transparent adhesive sheet, because during dicing the blade also touched the adhesive sheet. The scalpel blade was carefully placed along the line of the dicing marks and on the back of the wafer, at the precise position where on the front side of the wafer there was a cleave mark. A gentle and steady force was applied on the scalpel at that point until a click sound was heard, indicating that the cleave had been made. This process was done to each wafer along the edge where the scribe marks were made. Finally, the wafer was cleaved into several "bars" of devices, each containing one row of several 1mm by 1mm solar spectral condenser devices. Figure 6-6 shows the (a) top and (b) side view of the cleaved bar. In (b) the edge where the blade cut the wafer a tapered grove scribe mark can be seen, matching the curve of the rotating blade. Directly under this scribe mark the facet is jagged and damaged, but far away from this edge (about >1mm away from the edge of the wafer), the facet looks very smooth and clean. A smooth facet is important for efficient coupling to and from fiber modes.
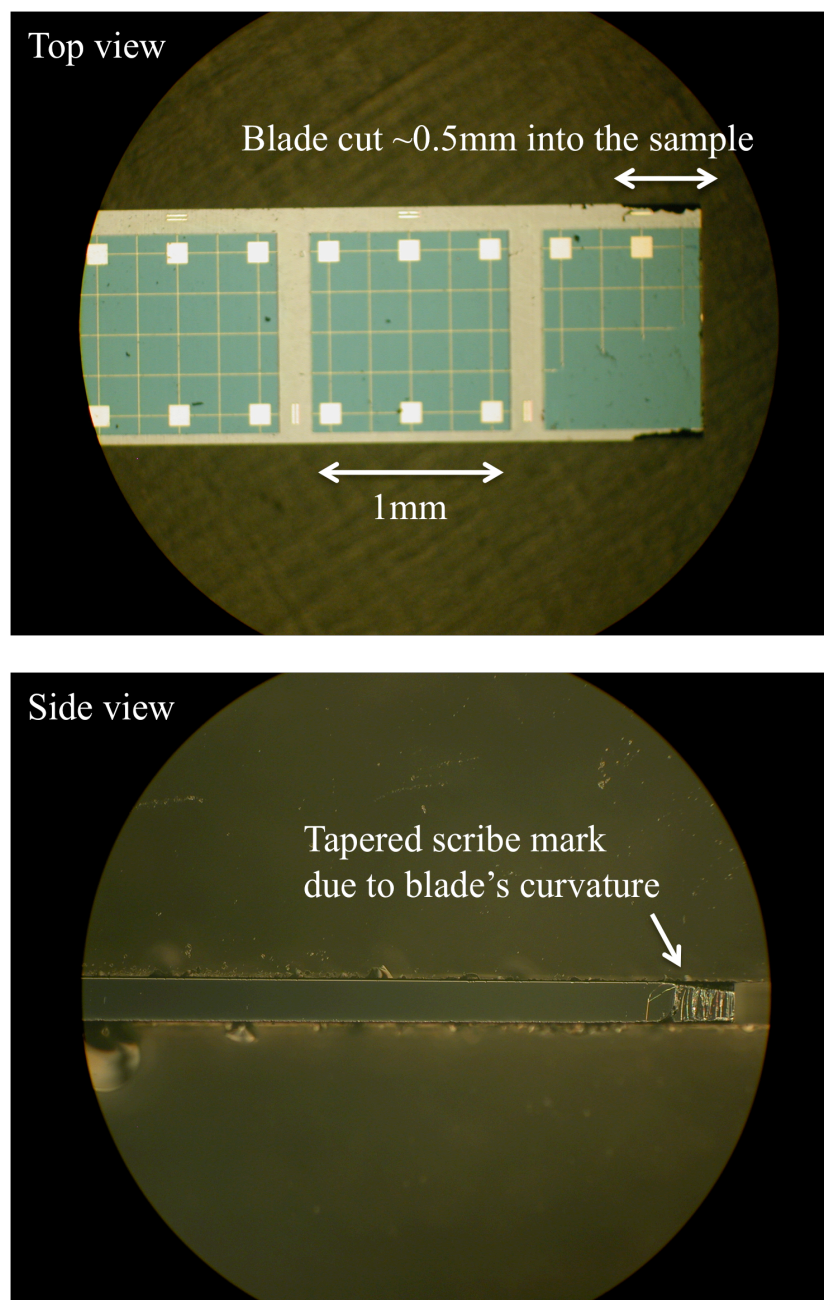
Figure 6-6   Cleaved solar spectral condenser devices (top and side views). Optical microscope images of cleaved sample, top and side views in the same magnification. In the top view the scribe marks of ~0.5mm can be seen. In the side view the scribe mark is obviously tapered, which matches the dicing blade curvature. Close to the scribe there are many cracks, but away from the scribe the cleave appears smooth. Roughness above and below the figure are from the glass slide used to sandwich the sample to stay upright for a side view in the optical microscope.

6.4   Wedge lensed fiber for improved coupling into waveguide

In order to make full use of the active area illuminated by sunlight, it would be ideal for the seed laser to be coupled into the entire slab waveguide by, for example, a "fiber" whose mode is the same dimensions as the cross-section of the slab waveguide (i.e., 2um by 1000um) and to use a similar "fiber" on the output end to fully collect the output light would be necessary.   However, such optical fibers are not readily available.   For this experimental study, it is possible to improve the coupling into the slab waveguide of the solar spectral condenser compared to a cleaved fiber or a conically lensed fiber by using a wedge lensed fiber, whose output is an elliptically shaped beam.   A detailed analysis of a Gaussian beam coming out of a conically lensed SMF-28 fiber is outlined in Appendix B.   Similar calculations can be done for a wedge lensed fiber.   In this section the working distance, spot size, and angular spread are estimated for different tapering angles and radii of the wedge lens.
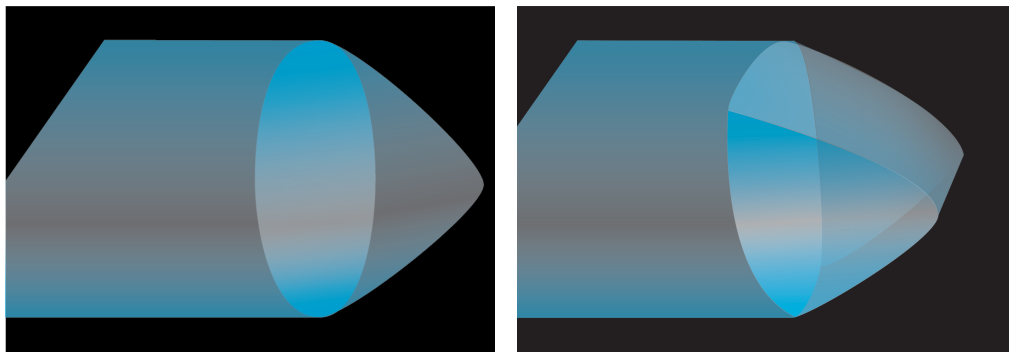
Figure 6-7   Illustration of conical and wedge lensed fiber tips.   Conical fiber (left) is a fiber whose end is tapered in a cone shape so that the tip is a spherical lens. Wedge fiber (right) is a fiber whose end is tapered like a wedge or chisel so that the tip is a cylindrical lens.   Not drawn to scale.   For visualization purposes only.

In Gaussian beam approximation, a Gaussian beam is characterized by the complex beam parameter by

$$\frac{1}{q(z)} = \frac{1}{R(z)} - i\frac{\lambda}{\pi n \omega^2(z)}$$

Eq. 6-2

where $q(z)$ is the complex beam parameter, $R(z)$ is the radius of curvature of the phase front, λ is the wavelength in vacuum, n is the index of refraction, and ω is the beam radius at $1/e^2$ intensity at point z in space in the line of propagation in the z-axis.

For any medium or optical element through which a Gaussian beam propagates, the final complex beam parameter $q_f(z)$ is related to the initial $q_i(z)$ by

$$q_f(z) = \frac{A \times q_i(z) + B}{C \times q_i(z) + D}$$

Eq. 6-3

where A, B, C, and D are the ray transfer matrix elements specific to the type of optical element such as a medium with finite distance, a lens, or an interface. A, B, C, and D can also be written as a matrix

$$\begin{bmatrix} A & B \\ C & D \end{bmatrix}$$

When there are multiple optical elements through which the beam passes, the *ABCD* matrix of each optical element can be cascaded by matrix multiplication. Appendix B shows an example which applies the optical transfer matrix multiplication for calculating the optical beam through cascaded media.
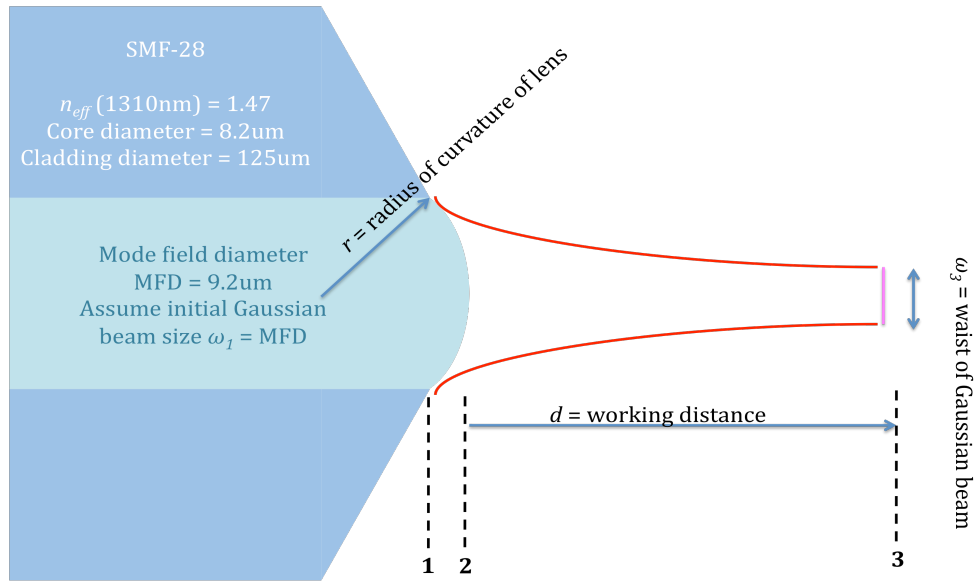
Figure 6-8   Gaussian beam approximation for conical lensed fiber. Diagram of optical beam coming out of a single-mode fiber with a conical lens tip, approximated by a Gaussian beam evaluated at points **1** (initial beam with same size as the mode field diameter of industry standard SMF-28 mode, immediately before the lens), **2** (immediately after the lens), and **3** (the beam at its waist ω_3, after travelling distance d in air). Figure not drawn to scale.

Figure 6-8 above illustrates a Gaussian beam travelling through a conically lensed industry standard SMF-28 fiber with lens radius of curvature r. The Gaussian beam at each point **1**, **2**, and **3** can be characterized by a complex beam parameter, $q_1(z)$, $q_1(z)$, and $q_3(z)$, respectively. Using the *ABCD* transfer matrix for each

propagation medium, i.e., the lens between **1** and **2**, and the space of distance *d*

between **2** and **3** (detailed analysis shown in Appendix B), a relationship between the

lens radius *r* and the beam waist ω_3 (subscript 3 indicates that it is the beam diameter

at point **3** of Figure 6-8), and between the lens radius *r* and the working distance *d* for

realistic lens radii (i.e. several micrometers) are found, shown in Figure 6-9.
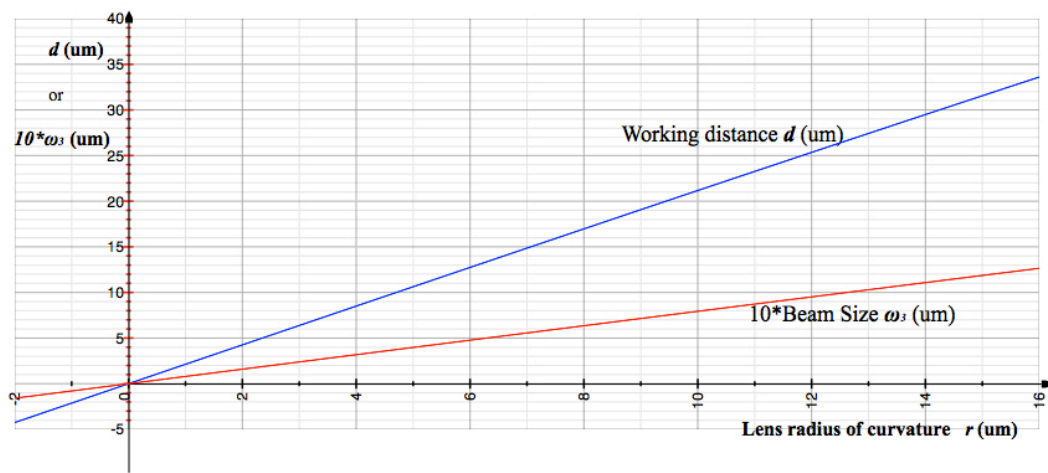
Figure 6-9   Working distance and spot size of Gaussian beam versus lens radius of conical lens. For visual purposes in this graph ω_3 is amplified by 10 (i.e. the value on the graph at *r* = 6um reads $10\omega_3 \approx 5$um, so $\omega_3 \approx 0.5$um). Subscript 3 in ω_3 indicates that it is the beam diameter at point **3** of Figure 6-8. Detailed analysis can be found in Appendix B.

A wedge lensed fiber tip is essentially a cylindrical lens instead of a spherical

lens as in the conical fiber. In the case of the conical lens, the Gaussian beam

converges to a beam spot at distance *d* and has a spot size or waist of ω_3 in all

directions in the plane of the beam, perpendicular to the direction of propagation (i.e.,

the beam is circular). For a wedge lens, since the lens is curved cylindrically, the

Gaussian beam starts out with a circular shape from inside the fiber, but when it travels out of the lens over a distance *d* it becomes an ellipse, where the major axis matches the direction where there is no curve in the lens, and the minor axis matches the direction where the lens is curved. Figure 6-10 shows a diagram of the beam when viewed from the two extreme directions. In Figure 6-10 (a), in one direction *y*, perpendicular to the direction of propagation *z*, the beam is being focused the same way as the conical lens. In Figure 6-10 (b), in the *x* direction, the beam is not focused at all, so it diverges as it propagates in the *z*-direction.

(a)   (b)
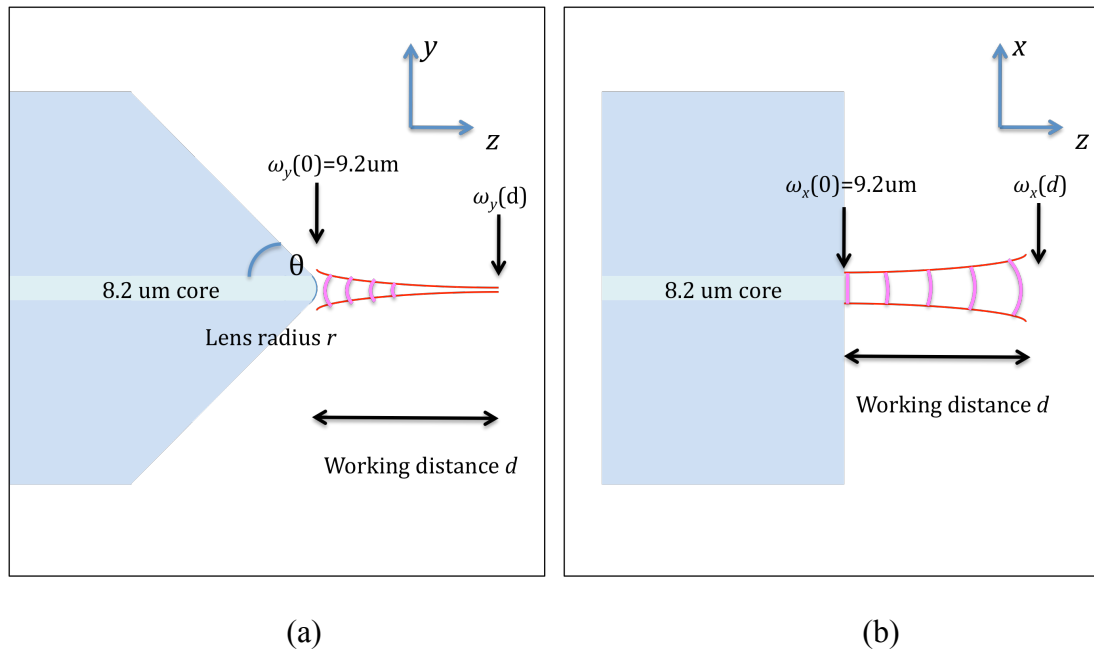
Figure 6-10   Gaussian beam approximation for wedge lensed fiber. (a) Illustration of the wedge lensed fiber in the *y-z* plane and the Gaussian beam size in the *y-*direction as it travels in the *z*-direction. The working distance *d* is the point in *z* at which the beam in the *y*-direction is at its waist waist $\omega_y(d) < \omega_y(0)$. (b) Illustration of the wedge lensed fiber in the *x-z* plane and the Gaussian beam size in the *x*-direction as it travels in the *z*-direction. Since the fiber is not lensed in the *x*-direction, the beam spreads out to a size $\omega_x(d) > \omega_x(0)$.

In the curved direction, the *y*-direction, of the lens, as in Figure 6-10 (a), the solution for the Gaussian beam is the same as that of the conical lens, in that the beam size shrinks because it is focused by the lens. But in the other direction, the *x*-direction, as in Figure 6-10 (b), the beam essentially passes through a flat surface with a change in optical index without being focused. The result is an elliptical shape at *z=d*, the point at which in the *y*-direction the beam is at its waist. Snapshots of the Gaussian beam in the *x-y* plane at *z=0* and *z=d* are shown in Figure 6-11 (a) and (b), respectively. The beam starts out circular in shape at *z=0*, but because of the wedge or cylindrical lens, at *z=d* it is focused in the *y*-direction and diverges in the *x*-direction.

(a)   (b)
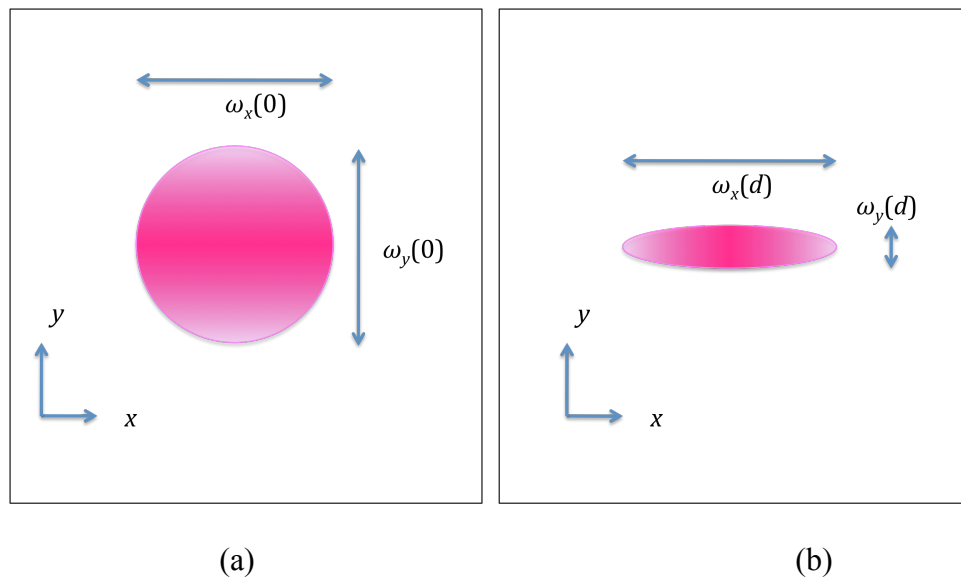
Figure 6-11   Illustration of Gaussian beam shape immediately after wedge lens and at its waist. (a) Gaussian beam shape immediately after the wedge lens (*z=0*). At this point the beam is approximately circular, that is, $\omega_x = \omega_y$. The phase front in the *x*-direction is flat (i.e., $R_x(0)$ is infinity) but in the *y*-direction it is curved (i.e., $R_y(0)$ is finite). (b) Gaussian beam shape after travelling the working distance *d* in the *z*-direction. At this point ω_y is minimized and the phase front in the *y*-direction is flat, and ω_x has spread out and its phase front is curved. The gradient of shading of the color in the figure is a visual indication of the phase front shape.

The working distance d is defined as the location of minimum ω_y, which from the analysis of the conical lens fiber is determined by r, the lens radius of curvature. For the y-direction, the same analysis can be done as the previous section with the conical lens. Using the working distance d, the divergence of the beam in the x-direction can then be calculated also using the $ABCD$ ray transfer matrix, where only one optical element, the distance d in air, is used.

$$\begin{bmatrix} A_x & B_x \\ C_x & D_x \end{bmatrix} = \begin{bmatrix} 1 & d \\ 0 & 1 \end{bmatrix}$$

Eq. 6-4

Using this ray transfer matrix the complex beam parameter in the x-direction q_x can be obtained. First, $q_x(z=0)$ in the x-direction is assumed to be a beam with a flat phase front since it essentially did not pass through a lens (or curved surface),

$$q_x(0) = i\frac{\pi n \omega_x^2(0)}{\lambda}$$

Eq. 6-5

Applying the ray transfer analysis using the $ABCD$ matrix in Eq. 6-4,

$$q_x(d) = i\frac{\pi n \omega_x^2(0)}{\lambda} + d$$

Eq. 6-6

Then, $q_x(d)$ can be written in the form $1/q_x(d)$, which is useful for separating out the terms for the radius of curvature $R_x(d)$ and the beam size $\omega_x(d)$,

$$\frac{1}{q_x(d)} = \frac{d - i\frac{\pi n \omega_x^2(0)}{\lambda}}{d^2 + \left(\frac{\pi n \omega_x^2(0)}{\lambda}\right)^2}$$

$$\frac{1}{q_x(d)} = \frac{d}{d^2 + \left(\frac{\pi n \omega_x^2(0)}{\lambda}\right)^2} - i\frac{\frac{\pi n \omega_x^2(0)}{\lambda}}{d^2 + \left(\frac{\pi n \omega_x^2(0)}{\lambda}\right)^2} \equiv \frac{1}{R_x(d)} - i\frac{\lambda}{\pi n \omega_x^2(d)} \qquad \text{Eq. 6-7}$$

The beam size $\omega_x(d)$ from Eq. 6-7 is plotted versus working distance d in Figure 6-12. Another consequence of the wedge lens is that the phase front at d in the y-direction is flat, but in the x-direction it is curved, since $1/R_y(d)$ is zero and $1/R_x(d)$ is nonzero.
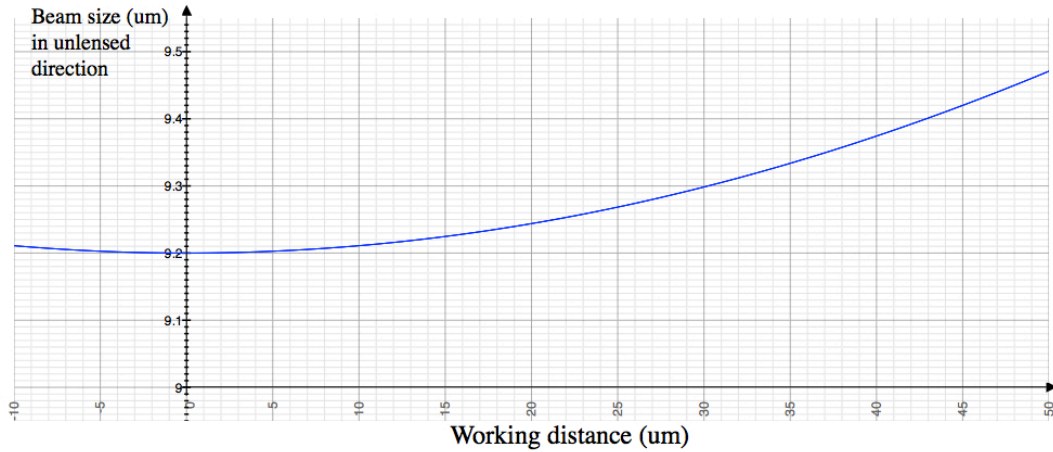
Figure 6-12   Beam size in x-direction versus working distance d. Gaussian beam spreads out in the x-direction as it travels in the z-direction since there was effectively no lens in the x-direction from the wedge lensed fiber.

One final consideration for the wedge lensed fiber dimensions is the angular spread of the beam. The wedge lensed fiber allows good coupling into a slab waveguide when the major axis of the elliptical beam, the *x*-axis, is aligned with the direction lateral to the waveguide layers, and the minor axis of the elliptical beam, the *y*-axis, is aligned with the direction transverse to the waveguide layers. In the *x*-direction, the beam is able to cover more of the waveguide while not spreading out too much as it propagates. In the *y*-direction, however, the Gaussian beam can easily spread out because of its small waist size. The angle of spread of the Gaussian beam in the *y*-direction Θ_y shown in Figure 6-13(b) is given by

$$\tan\Theta_y = \frac{\lambda}{\pi\omega_y n_{core}}$$

Eq. 6-8

where λ is the wavelength of the light, $\omega_y(d)$ is the spot size in the *y*-direction at *d*, and n_{core} is the waveguide core optical index.

For a slab waveguide with a core and a cladding with indices of refraction n_{core} and n_{clad}, respectively, the critical angle for total internal reflection θ_c is given by Snell's Law, where

$$\sin\theta_c = \frac{n_{clad}}{n_{core}}$$

Eq. 6-9

In the case of the solar spectral condenser, n_{core}=3.25 and n_{clad}=3.195 for λ=1.31um.

Applying Snell's Law in Eq. 6-9, the critical angle $\theta_c = 79.4°$. Using simple geometry

the angle of spread of the Gaussian beam Θ_y should be less than 90°-θ_c = 10.6° so that

the beam does not spread beyond the critical angle for total internal reflection.
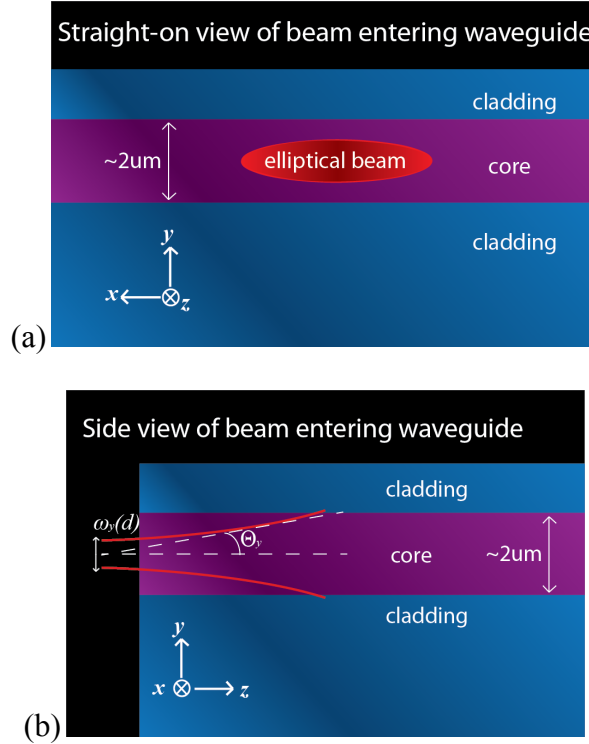
Figure 6-13   Illustration of elliptical beam entering the facet of a slab waveguide. (a) Straight-on view of the beam, and (b) side view. Angular spread of Gaussian beam in slab waveguide structure. The beam, outlined by the solid red lines, is assumed to couple into the waveguide at z=d, at the beam waist in the y-direction, $\omega_y(d)$. The slab waveguide has a core layer index $n_{core} = 3.25$ and cladding layer index $n_{clad} = 3.195$ on either side of the core, an approximation of the solar spectral condenser structure (excluding the thin IQW layer). The angular spread of the Gaussian beam, Θ_y, depicted by the black dotted lines, relative to the slab waveguide structure, is not shown to scale.

In summary, Table 6-1 shows the calculated beam waist $\omega_y(d)$, working distance d, divergence $\omega_x(d)$, and angular beam spread Θ_y for different curvature radii r_y. The beam waist in the y direction, $\omega_y(d)$, is related to the lens curvature r_y (Figure 6-10), which determines the beam spread Θ_y from Eq. 6-8. The divergence in the x-direction, $\omega_x(d)$, is related to the distance d (Eq. 6-7 and Figure 6-12). In Table 6-1 there is a tradeoff between having a small $\omega_y(d)$, for the beam to fit within the ~2um waveguide thickness, and a small Θ_y. Also, d should be reasonable for ease of physically coupling the input fiber to the waveguide. The divergence in the x-direction is least critical of these parameters (as well as least varying) since the waveguide is a slab and thus very long in the x-direction. A custom-made wedge lensed fiber with lens radius of curvature r_y = 15um from a commercial vendor, O/E Land, Inc. in Canada, was used for the solar spectral condenser measurement.

Table 6-1   Summary of wedge lensed fiber radii and calculated Gaussian beam dimensions for coupling into the solar spectral condenser. List of different radii of curvature r_y of wedge lensed fiber and resulting beam waist in y-direction $\omega_y(d)$, working distance d, divergence in x-direction $\omega_x(d)$, and angular beam spread in y-direction Θ_y.

Lens radius of curvature r_y (y-direction)	Waist $\omega_y(d)$ (y-direction)	Angular beam spread in y-direction Θ_y	Working distance d	Divergence $\omega_x(d)$ (x-direction)
6um	0.48 um	15°	12.8 um	9.22 um
8 um	0.63 um	11.5°	17.0 um	9.23 um
10 um	0.80 um	9.3°	21.0 um	9.25 um
12 um	0.95 um	7.7°	25.3 um	9.27 um
14 um	1.10um	6.7°	29.5 um	9.30 um
16 um	1.26um	5.8°	33.6 um	9.32 um

The results from a Beamprop simulation using the same waveguide structure as Section 5.3.3 (Figure 5-11a) with the input as an elliptical beam with major axis of 9.31um and minor axis of 1.2um is shown in Figure 6-14. This simulation confirms the effect of the wedge lensed fiber: compared to Figure 5-11 (b) and Figure 5-12, this elliptical input is an effective solution for keeping the seed laser propagation in the active region of the solar spectral condenser without spreading out too much laterally after propagating through 1000um length of the device.
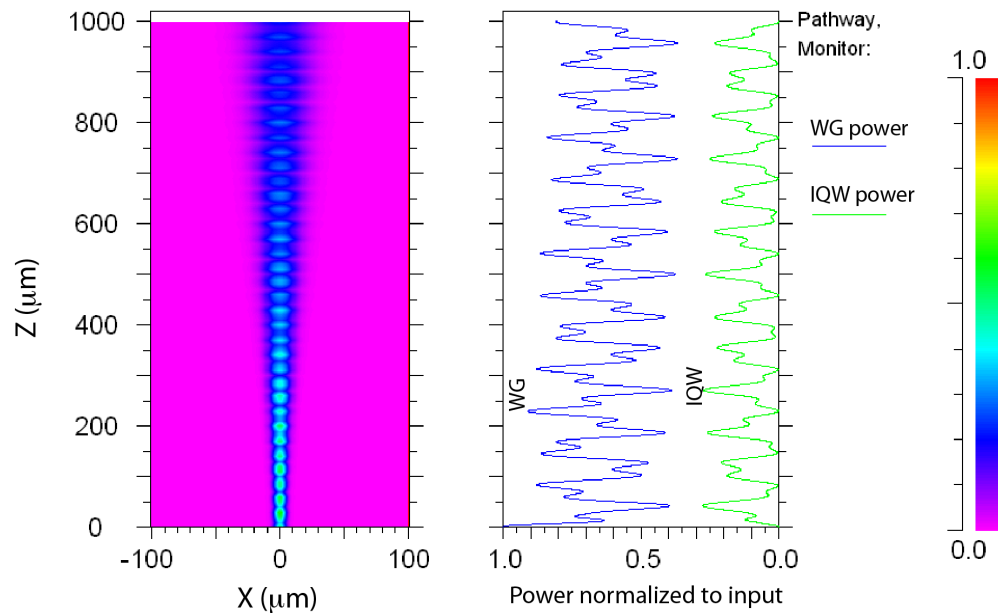
Figure 6-14   Beamprop simulation of solar spectral condenser structure with 9.31um (horizontal major axis) 1.2um (vertical minor axis) elliptical Gaussian beam input (representing a wedge lensed fiber input), showing the lateral mode spreading (left) and power in each layer (right).

6.5   Measurement setup

The solar spectral condenser devices were measured to determine the amount of solar energy that was converted to a concentrated, narrow spectrum, coherent, unidirectionally travelling signal.   Figure 6-15 shows an illustration of the measurement setup. There are two inputs: one is a small seed laser signal coupled into the waveguide region from the side via single mode fiber (SMF) with wedge lensed tip (left), and the other is the solar simulator light, concentrated with a lens, from directly above the device. The output light, coming out of the end of the device opposite the input was coupled into a multi-mode fiber (MMF) with 200um core diameter. The seed laser is a JDSU model 400A continuous wave at 1310nm whose signal was coupled into the waveguide via wedge lensed fiber. The solar simulator is a Newport 150W Low Cost Solar Simulator with 150W Xenon UV-enhanced arc lamp and AM1.5g filter, which has a built-in lens system, but to achieve even higher concentration of solar power an external lens was used. The solar simulator was placed on a stationary platform, but the external lens was mounted on a kinetic platform. The solar simulator and external lens were placed at positions so that the device under test was at the focal point of the combined lenses, to achieve highest concentration of light on the sample. The intensity of solar illumination, measured indirectly by the photocurrent through electrical probes connected to the p and n terminals of the device, was mainly tuned by moving the external lens. The output fiber coupled the output signal via cleaved multi-mode fiber into an optical power meter or an optical spectrum analyzer (OSA) Agilent model 86142B.
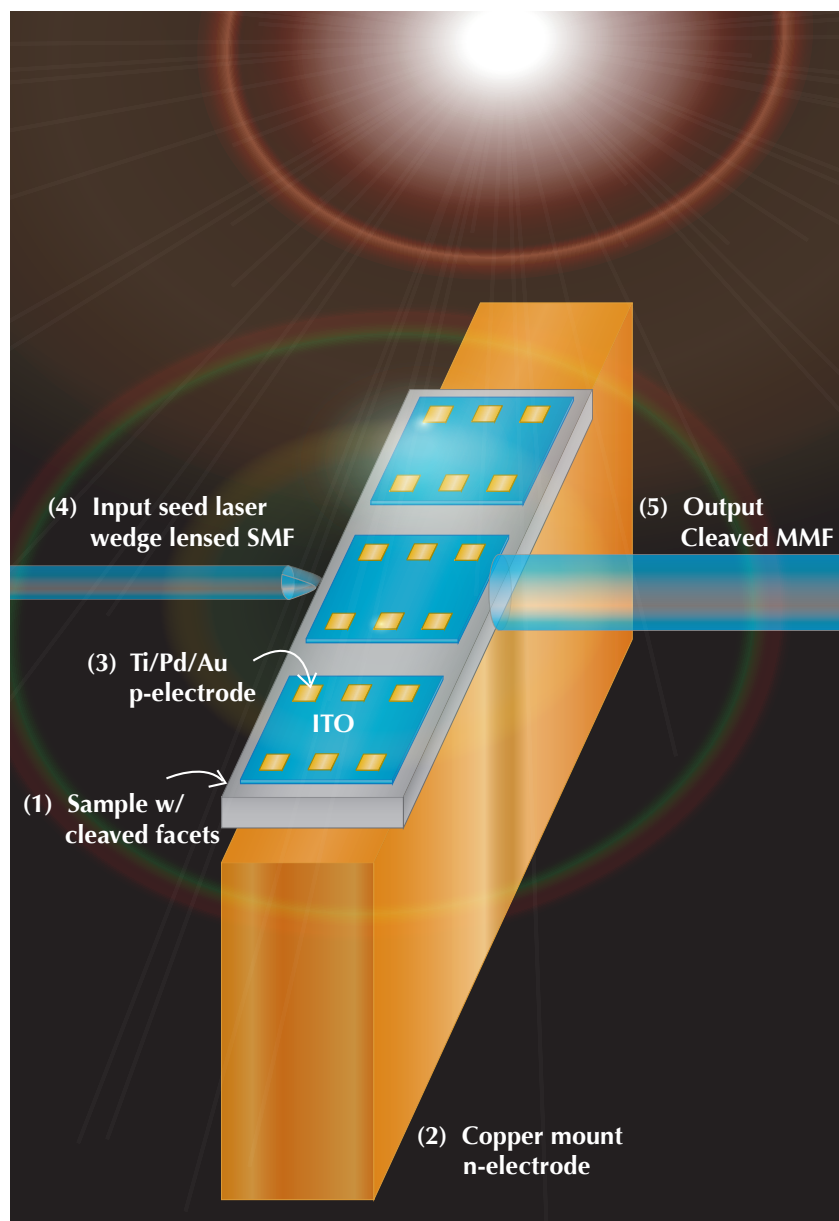
Figure 6-15   Illustration   of   solar   spectral   condenser   measurement   setup.
IQW/waveguide on InP substrate sample (1) with two cleaved facets (left and right
edges) were mounted with Epotek H20E conductive epoxy on a copper submount as
the *n*-electrode (2), which was mounted on a 2-axis stage (not pictured). The ITO
layer and Ti/Pd/Au contacts served as *p*-electrodes (3). Seed laser from JDSU 1310
nm CW laser (model 400A) was coupled into waveguide with a wedge lensed single
mode fiber (4), which was mounted on a 5-axis stage (not pictured) for alignment.
The output, measured using a handheld optical power meter or optical spectrum
analyzer, from waveguide was collected by a cleaved multi-mode fiber (5), also
mounted on a 5-axis stage, opposite the input. Solar simulator light, concentrated with
a lens, was normally incident on the top surface of the device.

6.5.1   Input and output fiber alignment

The input fiber and output fibers were both mounted on 5-axis (x, y, z, tilt, yaw) positioners, and the devices were mounted on a 2-axis position, which allowed for precision alignment.   The steps for obtaining proper alignment are outlined in Appendix D. The input wedge-lensed fiber is rotated such that the major axis of the elliptical beam is in line with the horizontal slab waveguide. Proper alignment of the input fiber was determined by monitoring two parameters while moving the fiber with the micro positioners: first, the optical power collected by the output MMF, measured at position (5) of Figure 6-15, and second, the photocurrent with only the seed laser (without solar illumination), measured by probing one of the *p*-metal pads, (3) in Figure 6-15, and the copper mount, (2) in Figure 6-15, which is in electrical contact with the backside *n*-contact metal of the device.

Without illuminating the device with the solar simulator, there is photocurrent due to the seed laser when it is properly aligned to the waveguide, because the IQWs immediately above the waveguide region can absorb some of the seed photons and create photocurrent if the device is short-circuited. The reason for this absorption is that the seed laser is not monochromatic (Figure 6-16) and there are some photons that are within the absorption range of the IQWs. When the fibers are improperly aligned, the photocurrent quickly drops to zero since there is no light in the IQWs. Table 6-2 lists measured photocurrent in uA corresponding to four different seed laser powers (measured at the output of the waveguide, position (5) in Figure 6-15).

Table 6-2   Measurements confirming optical fiber alignment. With the seed laser only when fibers are properly aligned, this table shows the measured optical output power (uW) at position (5) in Figure 6-15 and corresponding short-circuit photocurrent (uA). These photocurrents are much smaller than the photocurrent after the solar simulator is turned on.

Seed laser output (uW)	Photocurrent (uA)
3.5	5.2
10	40.3
15	54.2
19	68.6
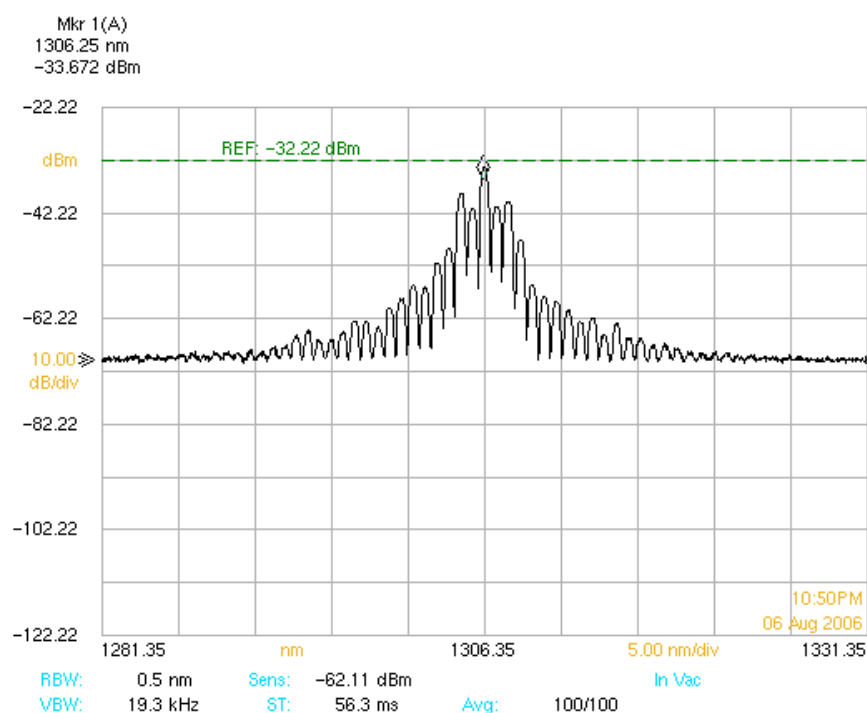
Figure 6-16   Optical spectrum analyzer (OSA) measurement of the seed laser spectrum. This measurement was done with the input fiber, (4) in Figure 6-15 coupled directly into the output fiber, (5) in Figure 6-15, without the device in between. The total laser power measured by a handheld power meter with a large detector area was -3.3dBm, but the power measured by the OSA is much smaller in magnitude because the input for the OSA is matched with a single-mode fiber, while the output fiber used in this measurement was a multi-mode fiber. Thus there is a large coupling loss at the input of the OSA. The date at the bottom right of this figure is incorrect (the measurement was done in 2010).

6.5.2 Active area versus total area

The volume illuminated by the seed laser is the nearly triangular area (approximately 25um by 1000um as shown in Figure 6-17), approximated from the Beamprop simulation in Figure 6-14, times the thickness of the multiple IQW layer, 200nm. Prior to turning on the solar simulator, the photocurrent due to the seed laser, as shown in Table 6-2, comes from this volume. When the solar simulator is turned on, the volume that contributes to photocurrent is the entire 1mm by 1mm (or 1000um by 1000um) mesa, times the 200nm thick IQW layer, shown by the area enclosed by the dotted line in Figure 6-17. Comparing the two volumes in Figure 6-17 represented by the areas from a top-down view of the measurement setup, the active area, which is the area illuminated by both the seed laser and the solar simulator during the measurement, is about 2.5% of the total area illuminated by the solar simulator.

output fiber

Dotted line:
1000um x 1000um,
total area of
p-i-n structure
illuminated by
solar simulator

Narrow triangular area:
approx. 25um x 1000um,
"active area" illuminated
by both the seed laser
and the solar simulator
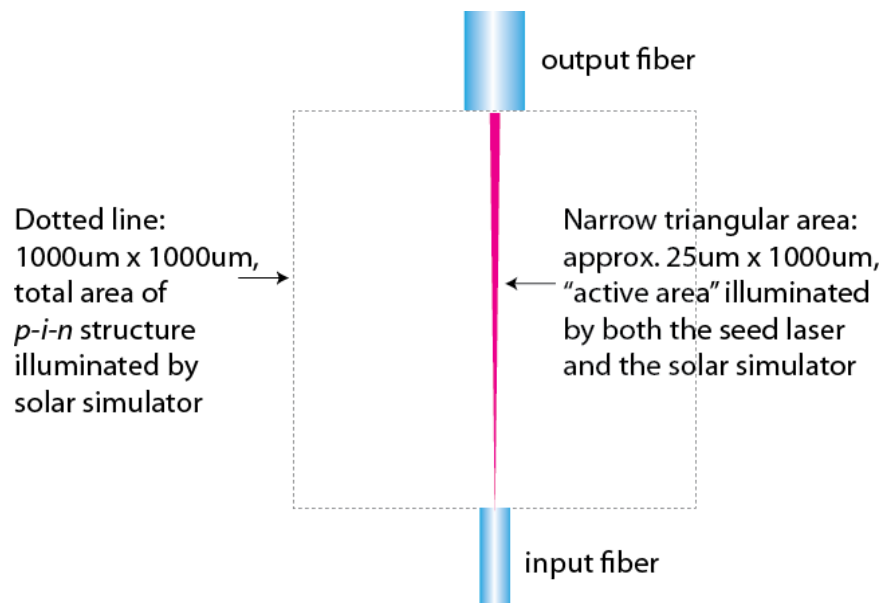
input fiber

Figure 6-17   Diagram of the active area vs. total area of solar spectral condenser.

6.5.3 Thermal issues

After the input and output fibers are aligned, before the solar simulator is turned on, a measurement is made of the optical power output and recorded as the baseline power. Then the solar simulator is turned on and the output measured again and compared to the baseline to determine the amplification. However, before taking each measurement with the illumination, the device was first illuminated for about one hour. Figure 6-18 shows the output optical power measured in uW versus time for 40 minutes after illuminating with the solar simulator with concentration such that the photocurrent with solar illumination of the active area was 2.51mA. It is clear that the output power gradually increased over time until it reached a steady state, in this case, about 9.7uW, more than 30min after the solar simulator was turned on. In general, it was observed that the higher the solar intensity, the longer it took to arrive at steady output optical power.

Since this change happened over a time in the scale of minutes, this effect is attributed to thermal changes after the solar simulator is turned on. The measurement setup had no external heat sinking devices. During the time the device under test heated up under the intense solar illumination, there is a decrease in the energy bandgap, which goes as

$$E_g(T) = E_g(0) - \frac{\alpha T^2}{T + \beta} \qquad \text{Eq. 6-10}$$

where $E_g(0)$ is the energy bandgap at zero degrees Kelvin, T is the temperature in degrees Kelvin, α and β are empirically determined [1,2]. Table 6-3 lists some of the values of α and β for relevant materials for this experiment.
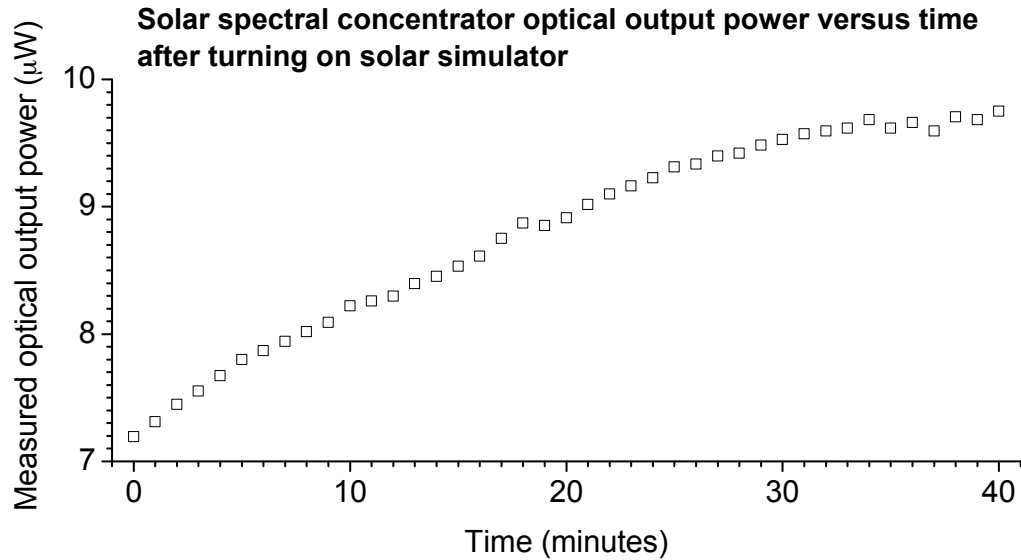
Figure 6-18   Output optical power versus time after solar simulator illuminated the solar spectral condenser device. For this instance the seed laser input power was 3.5uW (-25dBm) and the photocurrent corresponding to the solar intensity was 2.51mA, much larger than 5.2uA with only the seed laser input (Table 6-2).

Table 6-3   Bandgap temperature dependence parameters (published empirical values) for InP and InGaAsP.

Material	$E_g(0)$ [eV]	α [eV/K]	β [K]
InP [1]	1.42	4.1E-4	136
InGaAsP [2]	1.00	4.3E-4	224

In general, the bandgap of all of the layers in the device could shrink at about 0.3-0.4 meV per degree C in temperature increase, according to the numbers in Table 6-3. The decrease in bandgap of the IQW layers would result in higher absorption in longer wavelengths. If the temperature increase were purely from heating and not a result of high intensity light, then the seed laser power would be more readily absorbed by the IQWs, resulting in a decrease in power rather than an increase in power with time. However, from Figure 6-18 it can be seen that there is an increase in optical power at the output of the device, exactly opposite to what is expected when the bandgaps shrink. The increase in optical power at the output can only be a result of amplification of the seed by the photons from the solar illumination. A possible explanation is that the gradual heating (and thus gradual bandgap shrinking) indeed increases the absorption of longer wavelengths from the solar spectrum, which also causes the longer wavelengths of the non-monochromatic seed laser photons to be amplified.

6.6   Dependence on incident solar intensity by power measurement

An important experiment for the solar spectral condenser device is to measure how much of the solar power it can convert as the number of suns is increased. In Chapter 5, in Section 5.3.3 a calculation was done to determine that a minimum of 16 suns was required to make the IQWs transparent to 1310nm wavelength. On the other

hand, there is also a point at which the solar illumination intensity is so high that the output power saturates as discussed in Section 5.2.

The solar spectral condenser device was measured in the configuration shown in Figure 6-15. Optical power at the output was measured using a handheld power meter with the detector tuned to 1310nm while varying the solar intensity. The solar intensity, adjusted by changing the position of the external lens, was measured in-situ and indirectly by measuring the photocurrent of the 1mm x 1mm mesa using a digital multimeter in series with the device, and ranged between 0.5mA and 2.7mA. The photocurrent in the active area as discussed in Section 6.3.2 was estimated by taking 2.5% of the total mesa current. The photocurrent was measured first, and then the circuit was broken by disconnecting one of the electrical wires to the multimeter, and the output optical power was measured in open circuit mode. Opening the circuit ensures that the electrons and holes generated by the solar illumination are not converted into electrical current, but are rather reserved for the stimulated emission. A secondary variable, the seed laser power, was adjusted with an attenuator. The seed laser powers (measured by a handheld optical power meter at the output of the waveguide without solar illumination) used in this measurement were 3.5uW, 10uW, 15uW, and 19uW, the same as in Table 6-2. Figure 6-19 shows the raw data from this measurement with the output power, in uW, versus photocurrent (total and scaled) for each seed laser power. This data is then used to find the amplification of the 1310nm wavelength optical signal and the total solar power converted.
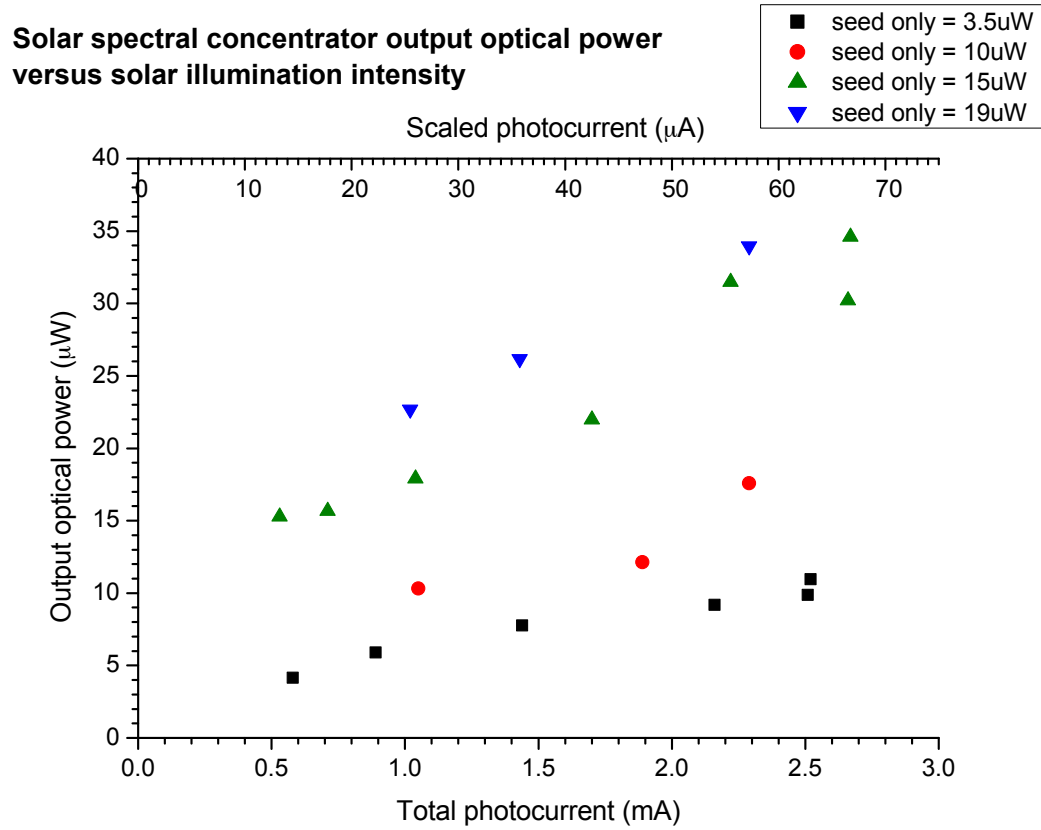
 Figure 6-19   Solar spectral condenser output dependence on solar intensity at open circuit at four different seed laser power levels.   The photocurrent (x-axis) is an indication of the solar intensity concentration.   The bottom x-axis is the total photocurrent measured for the 1mm by 1mm mesa; the top x-axis is the photocurrent scaled to the active area (Section 6.3.2).

The amplification is the ratio between the output optical power under illumination in uW and the output optical power with only the seed laser on in uW,

$$Amplification = \frac{P^{out}_{seed+solar}}{P^{out}_{seed\ only}}$$ Eq. 6-11

The number of solar photons converted to 1310nm wavelength photons per seed laser photon can be viewed as *Amplification* minus one. Thus an *Amplification* of 2 means that each seed photon was able to pick up one solar photon converted to 1310nm wavelength. The *Amplification* for each point in Figure 6-19 is plotted in Figure 6-20, in which the largest *Amplification* occurred at the lowest seed laser power (3.5uW, black squares). The *Amplification* generally increased as the solar intensity increased.
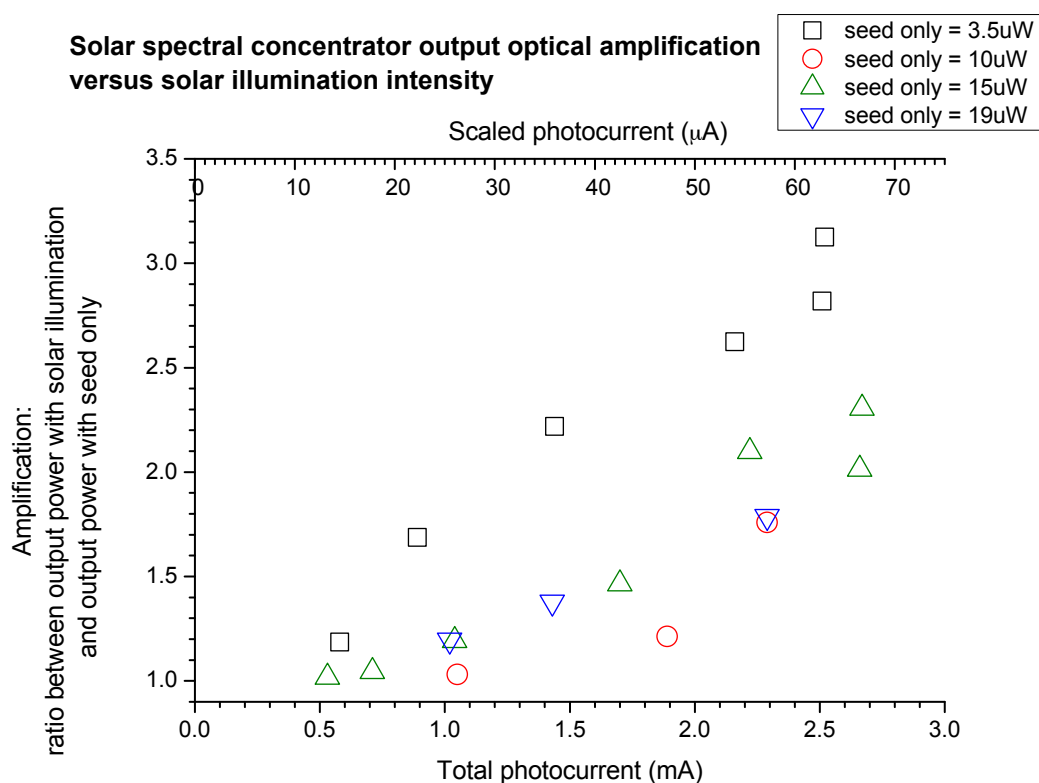
Figure 6-20   Solar spectral condenser amplification dependence on solar intensity at open circuit for four different seed laser powers. Ratio between the output power with solar illumination and the output power with seed laser only.

From this measurement of output optical power with varying solar illumination intensity for different seed laser powers it can be clearly seen that there is indeed amplification of the seed laser due to the solar illumination. The solar intensity could not be measured exactly in number of suns, but the measured photocurrent due to solar illumination was a good indicator of the amount of illumination concentration. For these particular seed laser and solar intensities, the *Amplification*, which is the ratio between the output with and without illumination, increases with increasing solar illumination. However, given the same solar illumination (photocurrent), the largest *Amplification* occurred with small seed laser input, meaning that the number of solar photons converted into 1.31um photons per seed photon is largest for the small seed laser power. Thus in terms of number of seed photons, the conversion from solar photons to 1.31um is more efficient for smaller number of seed photons.

Whereas *Amplification* is the ratio between the output power with and without illumination, another interesting figure to look at is the difference of the output optical powers between the output with and without illumination (uW), plotted in Figure 6-21,

$$Difference = P^{out}_{seed+solar} - P^{out}_{seed\ only} \qquad \text{Eq. 6-12}$$

This *Difference* in uW gives the additional power due to the solar illumination. In this case the greatest additional power due to illumination corresponds to the higher seed laser powers (15mW and 19mW, green up-triangles and blue down-triangles, respectively).
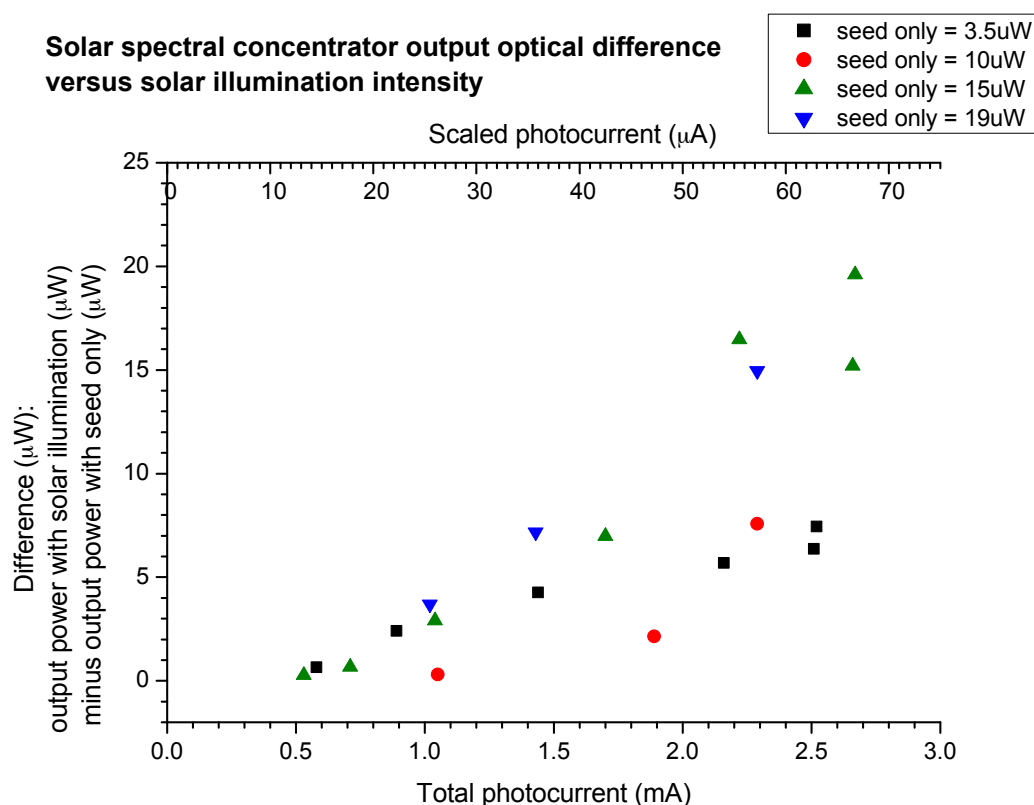
Figure 6-21   Solar spectral condenser power difference dependence on solar intensity at open circuit for four different seed laser powers. Difference between the output power illuminated and the output power in the dark.

The amount of power converted by the solar spectral condenser, indicated by the *Difference* in power under illumination and in the dark, increased with increasing solar power as well as with increasing seed laser input power. This means that in general, given the same solar illumination (photocurrent), the total number of solar photons converted into 1.31um photons is largest for large seed laser power. Thus the total conversion efficiency, the ratio between the output optical power and the input solar power, is larger for large seed laser power. This measurement was done for a

device with slab waveguide length of 1mm. In principle, if there are no other losses, the longer the device, the larger the volume there is for amplification until it reaches a saturation point discussed in Section 5.2. Thus for an infinitely long device the total conversion efficiency would be independent of the seed laser power, implying that only a very small seed laser is required.

The efficiency of the device is estimated by taking the "inverse response," which is the output optical power *Difference* divided by the scaled photocurrent,

$$Inverse\ response = \frac{P_{seed+solar}^{out} - P_{seed\ only}^{out}}{I_{seed+solar}^{scaled}} \qquad \text{Eq. 6-13}$$

where the numerator is in uW and the denominator is in uA. The *Inverse response* gives the ratio between converted optical power to converted electrical power. If the device were operated as a photovoltaic solar cell, the photocurrent would be *I*, and there would be an efficiency η_{PV} related to this *I* that is the photovoltaic efficiency. In this case, the scaled photocurrent is taken. Then the device is operated and measured as a solar spectral condenser in open-circuit and has a converted optical output power (*Difference*), which converts a portion of the carriers which would have been converted into current if the circuit were shorted, into optical power at 1310nm wavelength. This portion of carriers is the *Inverse response* term. The *Inverse response*, then, is proportional to the ratio between the efficiency of the solar spectral condenser η_{SSC} and the photovoltaic efficiency η_{PV},

$$Inverse\ response \propto \frac{\eta_{SSC}}{\eta_{PV}} \qquad\qquad \text{Eq. 6-14}$$

The *Inverse response* for each seed laser power is plotted in Figure 6-22. For 3.5uW seed (black squares) the *Inverse response* seems to saturate around 0.11, but for the other seed powers it seems to increase with increasing solar illumination intensity.
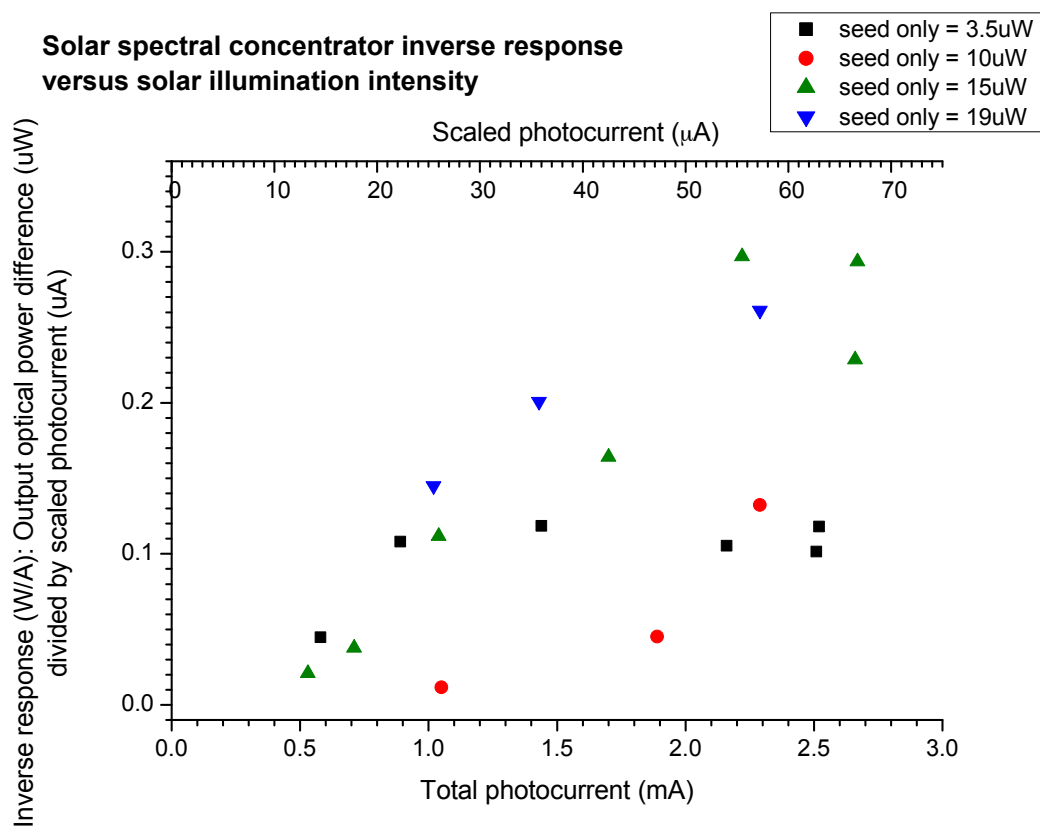
Figure 6-22   Inverse response of solar spectral condenser dependence on solar intensity at open circuit for four different seed laser powers. The inverse response is proportional to the efficiency of the device.

I-V measurements of the solar spectral condenser were done in a separate experiment to find the efficiency as a photovoltaic cell, η_{PV}. The intensity of the solar illumination was measured with an optical power meter for low solar illumination intensities, 0.69, 1.22, and 2.35 suns, compared to those used in the solar spectral condenser measurments. The reason that the optical power measurement could be done in this case is that the optical power meter has a relatively large area (about 2.5cm^2) compared to the device, for which a small number of suns the power distribution is relatively uniform. Thus it is accurate to divide the total optical power measured in the area to obtain the average intensity. However, for a large number of suns the lens concentrates the power to a small area, which is nonuniform over the 2.5cm^2 power meter. The η_{PV} for the solar spectral condenser is listed in Table 6-4, showing that on average, η_{PV} is about 10%. Assuming that η_{PV} is about 10% for any number of suns, and if the photocurrent scales linearly with the number of suns, then an estimatation of the efficiency of the solar spectral condenser η_{SSC} is η_{PV} multiplied by the *Inverse response*. Thus from Figure 6-22 the maximum efficiency achieved is about 3% for 15uW seed with 2.6mA total area photocurrent.

Table 6-4   Photovoltaic properties of the solar spectral condenser.

From *I-V*		From optical power meter		Efficiency η_{PV} (%)
Photocurrent (mA/mm^2)	P_{max} (mW/mm^2)	Intensity (mW/mm^2)	Number of suns	
0.204	0.072	0.69	0.69	10.4
0.292	0.117	1.22	1.22	9.6
0.488	0.215	2.35	2.35	9.2

From this measurement some conclusions can be drawn. First, there is amplification of the seed laser signal in the device due to the solar illumination, and this amplification increases as the concentration of solar illumination increases. Second, the total amount of optical power able to be extracted from the solar illumination, the *Difference*, also increases with more solar illumination, but it also increases as the seed laser intensity increases, evidence that the seed laser is important in the operation of the device. Third, it is possible to extract a figure called the *Inverse response*, which is proportional to the efficiency of the device. It is evident from this analysis that the efficiency of the device depends on the seed laser intensity, because the efficiency saturates for the low seed laser intensity, but continues to increase for higher seed laser intensities. However, the measurement does not show the ultimate efficiency of the device because the concentration of solar illumination was limited.

6.7 Dependence on bias voltage by spectral measurement

Next the bias voltage dependence of the solar spectral condenser was measured. Since the device contains IQWs that have carrier wavefunctions and energy levels that can be adjusted by changing the bias voltage, there should also be different amplification due to the bias. In this experiment the solar simulator was concentrated so that the photocurrent measured at short circuit was 1.9mA and the seed laser input was fixed. Then the bias voltage was varied using a voltage source, and the current was monitored using an ammeter. The spectral output optical power

measured by optical spectrum analyzer (OSA) for wavelength range from 1303nm to 1312nm. The spectral measurements were taken for bias voltages from -1.0V to +1.0V in 0.1V increments. Since the OSA measurement was done using a system that scanned through the wavelength range and sampled the power at individual wavelength steps, the measured power in Watts is not the actual power but a result of signal amplification and sampling; thus using the same sampling settings for each measurement the power curve within the measured range was normalized. Rather than looking at the absolute values of the powers, the optical powers are normalized to a constant value such that the relative powers can be compared. The "1310nm" seed laser measured with the OSA is not a monochromic laser but has many peaks within a range of about 20nm about 1310nm.

The measurement was first done in the dark with the device in short circuit. The solar simulator was turned on, heating up the sample for about one hour, before the spectral measurements were taken for the different applied bias voltages, using the average of 100 sweeps of the wavelength range for each bias. Figure 6-23 shows the optical power versus wavelength spectral measurement at short circuit and open circuit. Figure 6-24 shows the spectral measurement at -1.0V, 0V, and +1.0V. There are four peaks from the spectral measurements at 1305.4nm, 1307.7nm, 1308.5nm, and 1310.1nm. It is clear that for all of the peaks except at 1308.5nm there is an increase in detected power with illumination compared to that in the dark. There is a decrease in power under illumination for the 1308.5nm peak. On the other hand, there is a very large gain for the 1310.1nm peak.
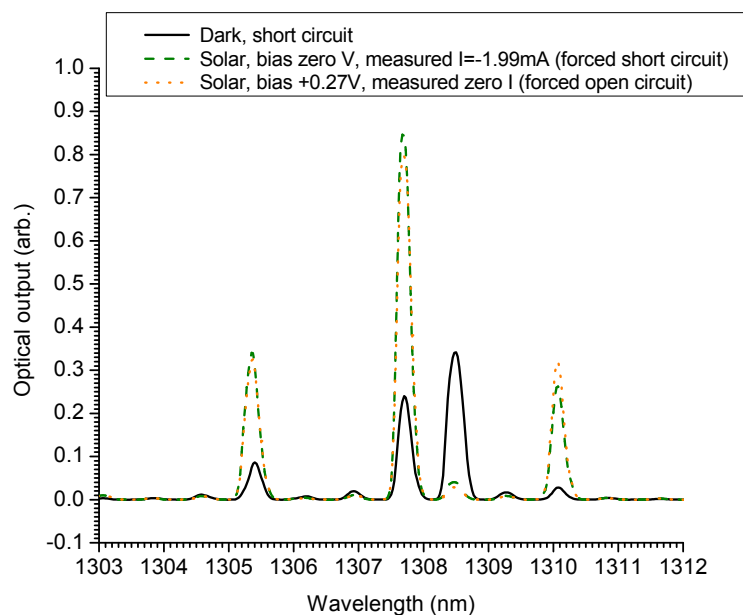
Figure 6-23   Solar spectral condenser output as measured by OSA comparing illuminated device in short-circuit and open-circuit with unilluminated device.
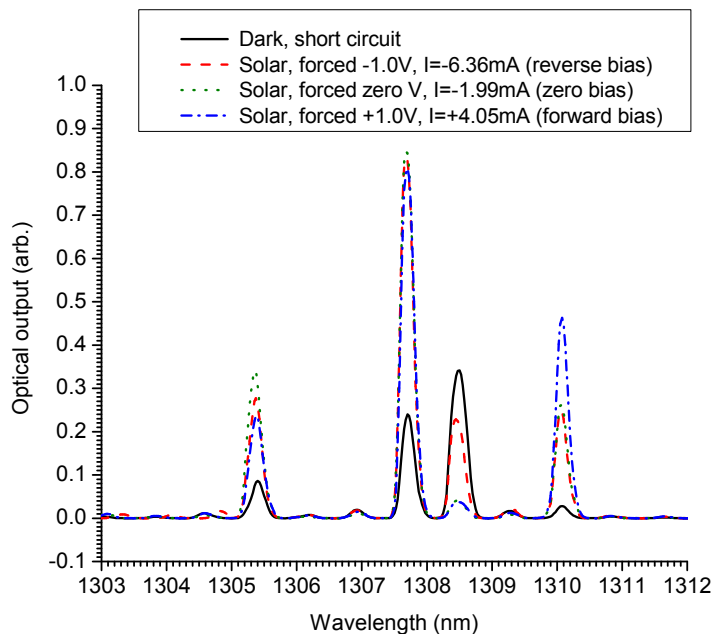
Figure 6-24   Solar spectral condenser output as measured by OSA comparing illuminated device at -1.0V, 0V, and +1.0V bias with unilluminated device.

A possible explanation for the suppression of the 1308.5nm peak is that with high solar illumination the gain spectrum is narrowing around 1310.1nm, depleting the gain for the 1308.5nm peak. Figure 6-25 shows the peak values versus bias voltage (from -1.0V to +1.0V with 0.1V steps) for the four peaks in four graphs.
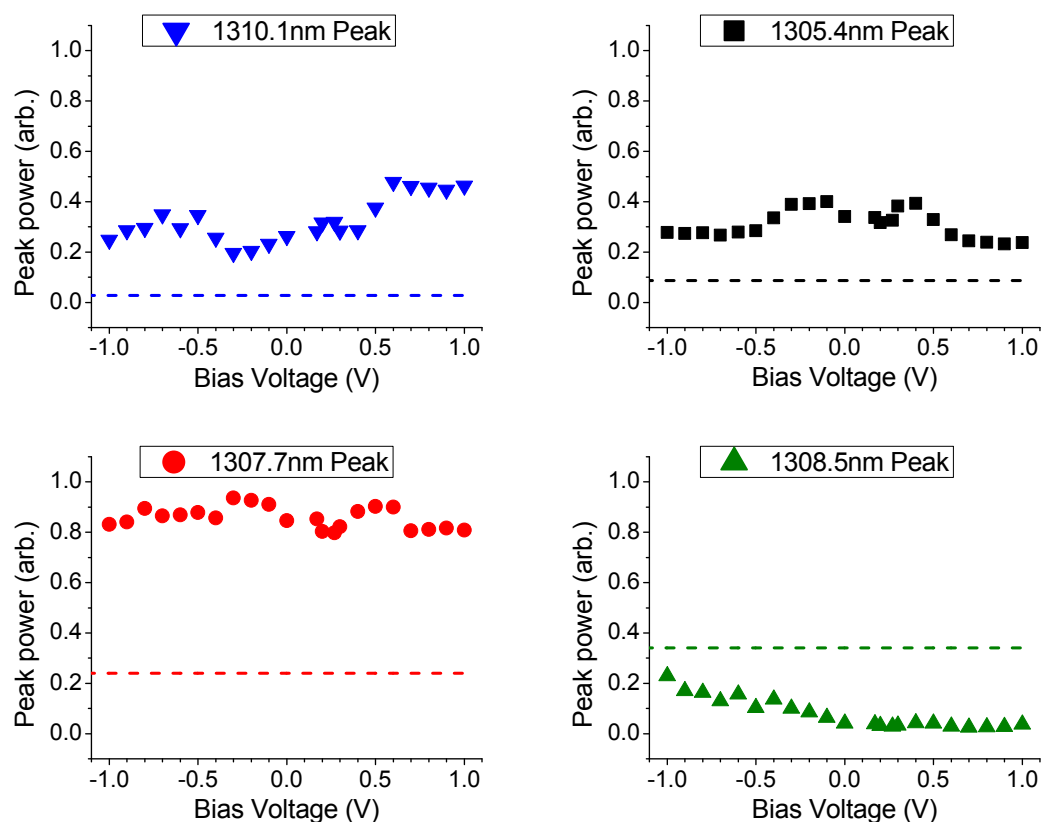
Figure 6-25   Peak optical power versus bias voltage for the four peak from Figures 6-23 and 24. The values each peak measured in the dark in short-circuit (zero bias), are plotted on the graphs as dotted lines.

For 1310.1nm the peak value increases as the bias moves from reverse to forward, whereas for 1308.5nm the peak value decreases, and are all lower than the peak measured in the dark. The fact that the two peaks, 1310.1nm and 1308.5nm are

trending in the opposite direction with bias is strong indication of gain, which is

narrowing the spetral gain region around 1310.1nm so that the 1308.5nm peak

decreases. For 1305.4nm and 1307.7nm the peak values versus bias voltage have

similar trends, being relatively unresponsive to the bias.
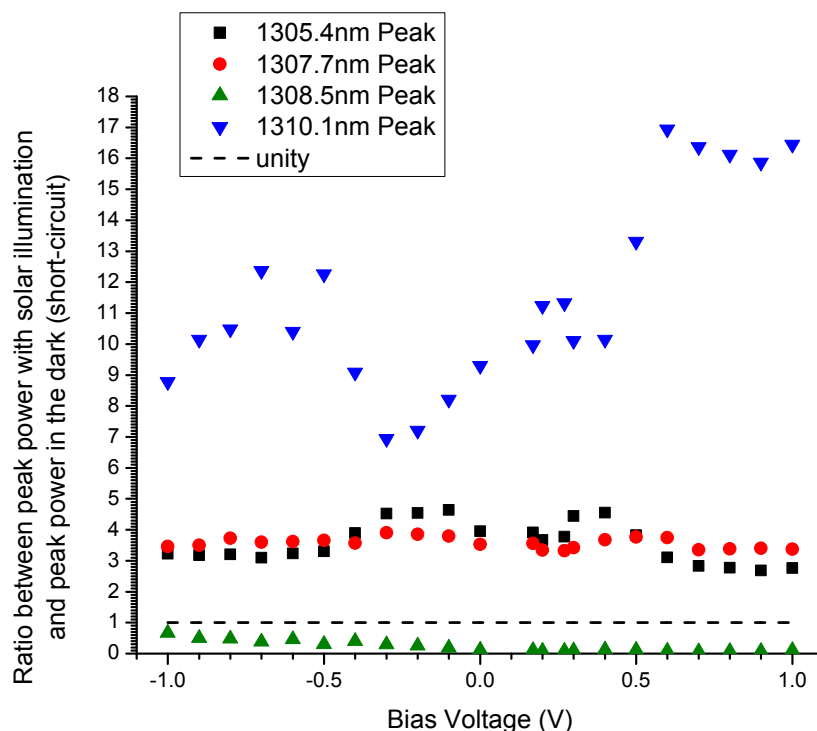
Figure 6-26   Peak optical power amplification versus bias voltage for the four peaks
from Figures 6-23 and 24. Unity amplification is shown in the figure as a dotted line.

Figure 6-26 shows the amplification of the peak power, that is, the ratio

between the peak values with solar illumination and the peak values in the dark. The

greatest amplification occurred at 1310.1nm, where the power was amplified more

than 16 times with forward bias of +0.6V and greater. This phenomenon may be the

result of a sharper optical resonance when the band bending is closer to flat band

(which is the case with forward bias), consistent with the simulation result in Figure 5-7. Except for the 1308.5nm peak, the amplification was generally larger for the longer wavelength peak (1310.1nm) than the shorter wavelength peaks (1307.7nm and 1305.4nm), an indication that transparency was achieved for 1310.1nm first.

6.8   Summary of solar spectral condenser experiment

It is evident in the output power and spectral power measurements from Sections 6.6 and 6.7 that there is amplification of the seed laser due to solar illumination on the solar spectral condenser device. In Section 6.6 it is clear that the output power as well as the amplification increased with the increase of the primary variable, the solar intensity, which was varied by a concentrating lens and measured indirectly by the short-circuit photocurrent. The point of saturation for the solar intensity was not achieved in this experiment since it was not possible to concentrate the solar illumination intensity any further with the experimental setup available. Varying the secondary variable in this measurement, the seed laser input power, showed that the amount of seed laser power input makes a difference for the 1mm long device. However, calculating the amplification (i.e., ratio between photons out with solar illumination and photons in the dark) in this measurement, it was found that the amplification was highest for the low seed laser input, so that with longer devices the seed laser input can be very small and still convert a significant amount of the solar power to narrow bandwidth optical power.

In addition to amplification, the total power converted, called *Difference* in Section 6.6, was extracted from the measurement. The actual number of suns incident on the device during each measurement could not be measured, but an estimation was made by measuring the photocurrent. The efficiency of the device measured as a photovoltaic cell was used to estimate that the efficiency of the device as a solar spectral condenser is about 3% for the largest solar illumination intensity.

In Section 6.7 the spectral output power measurement with varying the bias on the *p-n* junction of the solar spectral condenser device shows important evidence of the effect of band bending on the optical transitions in the IQWs, which was described in Section 5.3.2 and shown in Figure 5-7. The spectral measurement also shows evidence of stimulated emission because each of the laser peaks is amplified differently with the solar illumination. If the device were below the transparency threshold there would be no amplification detected in the spectral measurement. If the device were at the transparency threshold and not above it, then only the lower wavelengths would show amplification. In addition, if the device were at or below the transparency threshold there would be a broad, spontaneous emission, which is not detected. In this measurement there is indeed amplification of more than one of the laser peaks, evidence that there is stimulated emission. This experiment has achieved its purpose as a proof-of-concept, but many improvements can be done in the design and measurement setup of this experiment to show the complete saturation of gain.

6.9   References

[1]   S. Adachi, <u>Handbook on Physical Properties of Semiconductors</u>, Volumes 1-3, Springer-Verlag, p. 537 (2004).

[2]   K. Satzke, "Absorption and electroabsorption spectra of an In1-xGaxP1-yAsy/InP double heterostructure," J. Appl. Phys., 63 (11), pp. 5485-5490 (1988).

Chapter 7

Conclusion and Future Work

The goal of this study was to introduce two innovative ideas for improving the efficiency of solar cells by developing the theory for each idea and verifying them experimentally. In Chapter 1 the development in solar cells from the past 50 years was described. Today there are many branches of solar cell technologies (Figure 1-1), each of which began with an innovative idea that was improved upon in subsequent years. Chapter 2 described the theoretical efficiency of solar cells, and the operation and model of photovoltaic solar cells. In Chapters 3, 4, 5, and 6 descibe the design, fabrication, and measurement results of two solar power harvesting devices: the intrastep quantum well solar cell and the solar spectral condenser. Both devices are based on InGaAsP compound semiconductor materials and consist of IQWs in the *i*-region of a *p-i-n* structure. Both devices absorbed photons from the solar spectrum and converted them into electron-hole pairs through optical transitions. However, the IQWSC is a photovoltaic solar cell that converts photons into electrical current that can be transported via electrical wires while the solar spectral condenser is a device that converts photons from an unordered, broad spectrum into a narrow, unidirectional-travelling beam that can be transported via optical fibers.

7.1   Summary of results

In the photovoltaic IQWSC the IQWs, as described in Chapter 3, were designed to increase the efficiency of the solar cell compared to a bulk InP solar cell or a regular QW solar cell by (1) increasing the spatial overlap of electrons and holes inside of the QW region and (2) creating a smaller step for holes to overcome the QW barrier. The theory was tested in Chapter 4 by fabricating and measuring four solar cells which differed only in their *i*-layer composition: InP only, regular QW, IQW, and flipped IQW. The *I-V* and spectral photocurrent measurements confirmed that there is an improvement in solar energy conversion efficiency due to the presence of IQWs. From the *I-V* results the solar cell figures of merit as well as parasitic resistances were extracted, analyzed, and used to explain the data. The spectral photocurrent measurements were also analyzed. The conclusion was that the efficiency of the IQW solar cell was better than that of the flipped IQW, which was better than that of the regular QW, and also better than that of the bulk InP cell.

The theory for the solar spectral condenser described in Chapter 5 was that a structure with a gain layer on top of a waveguiding layer could be used to convert broad-spectrum solar power into narrow-spectrum, unidirectional optical power. The solar spectral condenser device used IQWs designed with an optical transition wavelength of 1310nm, which matches that of a seed laser used to boost the effect of the device. The idea was that the seed laser would be coupled into the waveguide below the gain layer, and the gain layer would be inversely populated by solar

illumination of 16 suns (calculated in detail in Chapter 5). Additional solar illumination above 16 suns would then be converted to 1310nm through stimulated emission so that these additional photons have the same momentum as the seed laser. The amplified seed laser signal is then collected by a multimode optical fiber at the output of the device. The theory was tested in Chapter 6, and it was found that there is indeed amplification of the seed laser with the solar illumination. Amplification, total power converted, and a term called "inverse response," a figure for efficiency, were extracted by analyzing the data. The efficiency of the device was estimated by using the inverse response figure to be 3% for the largest number of suns. Spectral measurements were also done to observe the effect of bias voltage.

7.2   Future work

The research done in this dissertation proved the concept of the effects of IQWs in solar power devices. For a more accurate assessment of the absolute efficiency of the IQWSC and solar spectral condenser, optimization of the experimental conditions and the device design should be done to measure their absolute efficiencies. For example, the IQWSC had very low efficiency for a III-V solar cell, but compared to the control samples, the IQWSC efficiency was largest. The absolute efficiency should be measured using an IQWSC optimized with antireflective coatings, no parasitic resistances, and larger absorbing volume.

7.2.1   Future work for intrastep quantum well photovoltaic cell

In Chapters 3 and 4 the transport of electrons and holes out of the quantum wells was assumed to be only by thermal escape, which is reasonable in this case since the IQWs and QWs of the tested devices were indeed relatively shallow and the barriers between wells were relatively thick. Future work can be done to study the effect of tunneling currents in IQWSCs.

In this dissertation the IQWs studied had two steps within the quantum well area, and since InGaAsP was used the bandgap alignment was Type I straddling. However, many different shapes can be conceived for the inside of the well such as multiple steps, graded bandgap, rounded wells, and different bandgap alignments. The purpose of this is the same as in this study: to increase efficiency by improving the overlap of electron and hole wavefunctions and decreasing the apparent barrier for carriers, especially holes, to escape the wells.

7.2.2   Future work for solar spectral condenser

For the solar spectral condenser, an important future experiment would be to measure the gain of a device that has 100% of the solar illuminated area to be the active area, or the area illuminated by the seed laser. In the measurement done in this study the active area was only 2.5% of the total solar illuminated area, which made it difficult to decouple the photocurrent from the optical gain. Also, the 2.5% was only an estimation from the Beamprop simulation. The purpose of having the active area

exactly match 100% of the solar illuminted area is to be able to have a larger contrast between the gain in open circuit and in short circuit. The idea is during open circuit of the device, all of the solar photons should convert into optical energy at the seed laser wavelength, but in short circuit, some of the solar photons convert into electrical current by contributing to the photocurrent.

The reason that the active area in this study is only 2.5% of the total area is that the input seed shape is very narrow while the waveguide is a slab. One way to make the active area of the solar spectral condenser closer to 100% of the solar illuminated area is to change the waveguide to be narrower by patterning narrower ridges rather than a square slab waveguide. Also, a coupling region can be added to the input side of the waveguide that helps spread the seed laser before entering the solar illuminated area.

7.2.3   Quantum dots for solar spectral condenser

Quantum dots should be the next major step for the solar spectral condenser device. The requirement for transparency, or population inversion, for the IQW structure with 1310nm wavelength optical transition was calculated in Chapter 5 to be 16 suns. The reason for this number of suns is that the effective density of states of the quantum well, a 2D quantum structure. However, the number of suns required for population inversion decreases with decreasing dimensions. Thus, quantum wires (1D) and quantum dots (0D) would require less illumination to achieve transparency.

Appendix A

Simulation MATLAB code for IQW structure

This appendix contains the MATLAB code for calculating the wavefunctions of the electrons and holes in the intrastep quantum wells (IQWs) for different electric fields (bias voltages). The code was first written in Mathematica by Dr. Dong-soo Shin, modified by Dr. Alan Chen, and later translated to MATLAB by Dr. Xiaobo Xie. It was modified for this dissertation to include positive and negative electric fields in one run.

```
%2011/03/01 This program was modified to calculate the wavefunctions of
%intrastep quantum wells for the purpose of solar cell i-layer, can be
%modified for different structures.  Rewritten by Winnie Chen
%The specific structure here is
%(barrier/intra/well/barrier)=(InP/InGaAsP/InGaAsP/InP)=(50/80/20/50),
%where the intra is on the left of the well.  This MATLAB code can
%simultaneously evaluate for both the IQW and Flipped IQW by going from
%positive to negative bias voltages.

% Based on the program from Xiaobo Xie in quotes below:

% "This program is used to calculate quantum well (QW) properties for
% electroabsorption modulator (EAM) design.
% rewritten by Xiaobo Xie based on Mathematica code from Dong-soo Shin
% ver. 1.0, 3/3/2006
% modified on 09/23/2006 to calculate blueshift QW material
% (InP/InAsP/InGaAs/InP)"
```

```
clear; % clear all variables
t = cputime % used to calculate total calculation time
format long;

% physical constants
hbar = 1.05457e-34; % reduced Planck constant, J-s
q = 1.60218e-19; % electron charge, C
me = 9.1094e-31; % electron mass, kg
c = 2.998e8; % speed of light, m/s
eps0 = 8.85419e-12; % permittivity in vacuum, F/m
x0 = sqrt(hbar^2/me/q)*1e10; % normalized length unit used in calculation

r = 2.0/x0^2;
v0 = 0.0; % constant energy shift

% quantum well structure: THESE ARE VARIABLES THAT SHOULD BE CHANGED FOR
% THE DIFFERENT IQW STRUCTURES
wellwidth = 100; % total intra plus well quantum well thickness in Angstroms
intrawidth = 80; % intra-step quantum well thickness in Angstroms
ithickness = 1250; % intrinsic layer thickness in Angstroms--this is the total
%i-layer thickness that the voltage will drop on.  The actual calculation
%of the Schrodinger equation is done only on the one IQW
% bias voltage setting: THIS SHOULD BE SET BY THE USER TO ADJUST FOR
% DIFFERENT BIAS VOLTAGES
vmax = -0.6; % maximum bias voltage.  The entry for this value should
%be a negative number.  The calculation will go from positive absolute
%value of this number to negative absolute value of this number
vstep = -.1; % step of voltage increment.  This should be negative.

% material properties: THESE SHOULD BE SET BY THE USER
% InGaAsP
aswell =0.25; % As composition in well material

mcwell = 0.071199;
mvwell = 0.5471;

epswell = 12.5;
mcbarrier = 0.077;
mvbarrier = 0.56;
mcintrabarrier = 0.074361;
mvintrabarrier = 0.55353;
wellbandgap = 1.1775;
barrierbandgap = 1.35; % InP
intrabandgap = 1.2619;
deltabandgap = barrierbandgap - wellbandgap;

coffset = 0.4*deltabandgap;
voffset = 0.6*deltabandgap;
cintraoffset = coffset - 0.4*(barrierbandgap - intrabandgap);
vintraoffset = voffset - 0.6*(barrierbandgap - intrabandgap);
```

```
    mu = me*mcwell*mvwell/(mcwell+mvwell);

    % some useful equations
    %alpha0 = 1e8*q^2*mu*(19.7+5.6*aswell)/(4*eps0*c*me*hbar*sqrt(epswell)*2*wellwidth); % cm^(-
    1)
    alpha0=15000;
    ryd = q^3*mu/(2*eps0^2*hbar^2); % Rydberg constant in eV
    lambdaex0 = 100; % starting point of trying exciton radius, in Angstroms
    alpha0

    % quantum well eigen function and eigen value calculation
    range = wellwidth;
    npoints = 1000; % number of grid points
    h = 2.0*range/(npoints+1); % step of grid
    wover2 = wellwidth/2; % half of the well width

    meshnum = 10;
    kstep = 1;

    for i=1:meshnum
       lambdaex = lambdaex0+(i-1)*10;
       for j=1:npoints
          integ(i,j) = 0;
          for k=kstep:kstep:1000
             integ(i,j) = integ(i,j)+k*exp(-2*k/lambdaex)/sqrt(k^2+(h*(j-1))^2);
          end;
       end;
    end;

    for vbn=0:(2*vmax/vstep+1)
       vbias = vbn*vstep-vmax;
       vb(vbn+1) = vbn*vstep-vmax;
       efield = vbias/ithickness; % in V/Angstrom
       ef(vbn+1) = efield;
       vbias;
       xi = -range+h:h:range-h;
       xi2 = -range+h/2:h/2:range-h/2; % used in p and q construction
       % define intra-step QW structure
       for i=1:npoints
          if abs(xi(i))<wover2
             if xi(i)<(intrawidth-wover2)
                vc(i, vbn+1) = v0+cintraoffset-efield*xi(i);
                vv(i, vbn+1) = v0+vintraoffset+efield*xi(i);
                mc(i, vbn+1) = mcintrabarrier;
                mv(i, vbn+1) = mvintrabarrier;
             else
                vc(i, vbn+1) = v0-efield*xi(i);
                vv(i, vbn+1) = v0+efield*xi(i);
                mc(i, vbn+1) = mcwell;
                mv(i, vbn+1) = mvwell;
```

```matlab
            end;
        else
            vc(i, vbn+1) = v0+coffset-efield*xi(i);
            vv(i, vbn+1) = v0+voffset+efield*xi(i);
            mc(i, vbn+1) = mcbarrier;
            mv(i, vbn+1) = mvbarrier;
        end;
    end;
end;
% construction of p and q arrays
for i=1:2*npoints+1
    if abs(xi2(i))<wover2
        if xi2(i)<(intrawidth-wover2)
            pc(i) = 1/mcintrabarrier;
            qc(i) = 2/x0^2*(v0+cintraoffset-efield*xi2(i));
            pv(i) = 1/mvintrabarrier;
            qv(i) = 2/x0^2*(v0+vintraoffset+efield*xi2(i));
        else
            pc(i) = 1/mcwell;
            qc(i) = 2/x0^2*(v0-efield*xi2(i));
            pv(i) = 1/mvwell;
            qv(i) = 2/x0^2*(v0+efield*xi2(i));
        end;
    else
        pc(i) = 1/mcbarrier;
        qc(i) = 2/x0^2*(v0+coffset-efield*xi2(i));
        pv(i) = 1/mvbarrier;
        qv(i) = 2/x0^2*(v0+voffset+efield*xi2(i));
    end;
end;
for i=1:npoints
    ac(i) = pc(2*i-1)/r;
    av(i) = pv(2*i-1)/r;
    cc(i) = pc(2*i+1)/r;
    cv(i) = pv(2*i+1)/r;
    bc(i) = -(ac(i)+cc(i)+(h^2*qc(2*i)/r));
    bv(i) = -(av(i)+cv(i)+(h^2*qv(2*i)/r));
end;
ac = ac(2:npoints);
av = av(2:npoints);
cc = cc(1:npoints-1);
cv = cv(1:npoints-1);
Ac = diag(bc)+diag(ac, -1)+diag(cc, 1);
Av = diag(bv)+diag(av, -1)+diag(cv, 1);

% solve eigen value problem
[ceigvec, ceigval] = eig(Ac);
[veigvec, veigval] = eig(Av);
ceigval = -diag(ceigval)./h^2;
veigval = -diag(veigval)./h^2;
cselect = find(ceigval>(v0-abs(efield)*wover2) & ceigval<(v0+coffset-abs(efield)*wover2));
ceigvec = ceigvec(:,cselect);
```

```
        ceigval = ceigval(cselect)-v0;
        vselect = find(veigval>(v0-abs(efield)*wover2) & veigval<(v0+voffset-abs(efield)*wover2));
        veigvec = veigvec(:,vselect);
        veigval = veigval(vselect)-v0;
        cselectground = find(ceigval==min(ceigval));
        ceigvalground = ceigval(cselectground);
        ceigvecground = ceigvec(:,cselectground);
        ceigvecground = sign(ceigvecground(npoints/2)).*ceigvecground;
        vselectground = find(veigval==min(veigval));
        veigvalground = veigval(vselectground);
        veigvecground = veigvec(:,vselectground);
        veigvecground = -1*sign(veigvecground(npoints/2)).*veigvecground;

        cplot(vbn+1,:) = ceigvecground'+ceigvalground+wellbandgap;
        clevelplot(vbn+1,:) = ceigvalground*ones(1,npoints)+wellbandgap;
        vplot(vbn+1,:) = veigvecground'-veigvalground;
        vlevelplot(vbn+1,:) = -veigvalground*ones(1,npoints);

        overfun(vbn+1) = sum(abs(ceigvecground.*veigvecground));

        % some more calculation
        tranenergy(vbn+1) = wellbandgap+ceigvalground+veigvalground;
        tranwavelength(vbn+1) = 1.24/tranenergy(vbn+1); % for 1550 nm wavelength

        % wavefunction overlap integration etc.
        % exiton binding energy and exciton radius

        zemin = -range+h;
        zemax = range-h;
        zhmin = -range+h;
        zhmax = range+h;
        rmax = 1000;
        eps = 12.35;
%       meshnum = 10;
%       kstep = 1;
%
%       for i=1:meshnum
%           lambdaex = lambdaex0+(i-1)*10;
%           for j=1:npoints
%               integ(i,j) = 0;
%               for k=kstep:kstep:1000
%                   integ(i,j) = integ(i,j)+k*exp(-2*k/lambdaex)/sqrt(k^2+(h*(j-1))^2);
%               end;
%           end;
%       end;
        excitonenergy=0;
        for m=1:meshnum
            excitonenergy0 = 0;
            lambdaex = lambdaex0+(m-1)*10;
            for i=1:npoints
                for j=1:npoints
```

```
        excitonenergy0  =  excitonenergy0+(ceigvecground(i))^2*(veigvecground(j))^2*integ(m,abs(i-
j)+1)
      end;
    end;
    excitonenergy0=-10^23*hbar^2/2/mu/lambdaex^2/q+
10^13*q/pi/eps/eps0/lambdaex^2*excitonenergy0*kstep;
    if excitonenergy0>excitonenergy
      excitonenergy=excitonenergy0;
      radfun(vbn+1) = lambdaex;
    end;
  end;
  excitonenergy;
  exeenergy(vbn+1) = tranenergy(vbn+1) - excitonenergy/1000;
  % calculation of total absorption
  gamag = 7.5/1000; % assume exciton has Gaussian broadening, FWHM gamag is in meV
  gamal = 5/1000; % assume band to band has Lorentzian broadening, FWHM gamal is in meV

  for i=1:351
    wave(i) = 0.8 + 0.001*(i-1);
    wave_energy(i) = 1.24/wave(i);
    alphabb(vbn+1,i)                                                                            =
alpha0*(overfun(vbn+1))^2*wave(i)/1.24*((1.24/wave(i))>tranenergy(vbn+1))*2/(1+exp(-
2*pi*sqrt(abs(1.24/wave(i)-tranenergy(vbn+1))/ryd)));
    alphaex(vbn+1,i)                                                                            =
1.88*10^20*hbar^2*alpha0*(overfun(vbn+1))^2/q/1.24*wave(i)/(radfun(vbn+1))^2/gamag/mu/sqrt(
2*pi)*exp(-(1.24/wave(i)-exeenergy(vbn+1))^2/2/gamag^2);
    alphabb1(vbn+1, i) = 0;
    for j=1:2000
      tr1(j) = -2.001+0.002*j;
      wave2(j) = 1.24/tr1(j);
      alphabb2(vbn+1,j)                                                                         =
alpha0*(overfun(vbn+1))^2*wave2(j)/1.24*((1.24/wave2(j))>tranenergy(vbn+1))*2/(1+exp(-
2*pi*sqrt(abs(1.24/wave2(j)-tranenergy(vbn+1))/ryd)));
      alphabb1(vbn+1,i)                      =                      alphabb1(vbn+1,i)+0.002*alphabb2(vbn+1,
j)*gamal/pi/(gamal^2+(1.24/wave(i)-1.24/wave2(j))^2);
    end;
    alphatt(vbn+1, i) = alphaex(vbn+1, i)+alphabb1(vbn+1, i);
  end;


end;

% hold on;
% for vbn=0:(vmax/vstep)
%    plot(wave, alphatt(vbn+1,:)/10000);
% end;

figure(1);
plot(wave, alphatt(1,:), wave, alphatt(2,:), wave, alphatt(3,:), wave, alphatt(4,:), wave, alphatt(5,:),
wave, alphatt(6,:), wave, alphatt(7,:), wave, alphatt(8,:));
xlabel('Wavelength (\mum)');
```

```
ylabel('Absorption Coefficient (cm^{-1})');

figure(2);
plot(xi, vc + wellbandgap, xi, clevelplot, xi, cplot, xi, -vv, xi, vlevelplot, xi, vplot);

figure(3);
plot(vb, tranenergy, '--s', vb, exeenergy, '--d');

figure(4);
plot(vb, overfun,'--o');

figure(5);
plot(wave_energy, alphatt(1,:), wave_energy, alphatt(2,:), wave_energy, alphatt(3,:), wave_energy,
alphatt(4,:), wave_energy, alphatt(5,:), wave_energy, alphatt(6,:), wave_energy, alphatt(7,:),
wave_energy, alphatt(8,:), wave_energy, alphatt(9,:));
xlabel('Energy (eV)');
ylabel('Absorption Coefficient (cm^{-1})');

figure(6);
plot(wave_energy, alphaex(1,:), wave_energy, alphaex(2,:), wave_energy, alphaex(3,:), wave_energy,
alphaex(4,:), wave_energy, alphaex(5,:), wave_energy, alphaex(6,:), wave_energy, alphaex(7,:),
wave_energy, alphaex(8,:), wave_energy, alphaex(9,:));
xlabel('Energy (eV)');
ylabel('Exciton Absorption Coefficient (cm^{-1})');

figure(7);
plot(wave_energy, alphabb1(1,:), wave_energy, alphabb1(2,:), wave_energy, alphabb1(3,:),
wave_energy, alphabb1(4,:), wave_energy, alphabb1(5,:), wave_energy, alphabb1(6,:), wave_energy,
alphabb1(7,:), wave_energy, alphabb1(8,:), wave_energy, alphabb1(9,:));
xlabel('Energy (eV)');
ylabel('Band-to-band Absorption Coefficient (cm^{-1})');

%figure(5);
%[C,h]=contour(wave_energy, vb, alphatt, 20);
%clabel(C,h);


cputime-t
```
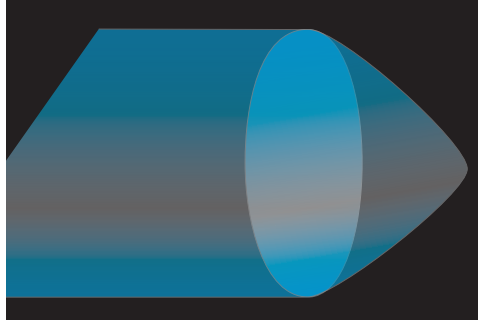
Appendix B

Conical lensed fiber

Figure B-1   Conical lensed fiber tip.

In this appendix the conical lensed fiber beam is calculated by approximating the beam as a Gaussian and using ray transfer matrix analysis. In the Gaussian beam approximation formulation, an optical beam can be characterized by a complex beam parameter $q(z)$,

$$\frac{1}{q(z)} = \frac{1}{R(z)} - i\frac{\lambda}{\pi n \omega^2(z)}$$

where $R(z)$ is the radius of curvature of the phase front of the beam, λ is the wavelength in vacuum, n is the index of refraction, and ω is the beam radius at $1/e^2$ intensity at point z, relative to the beam waist.

Figure B-2 shows a diagram of a SMF-28 fiber with a conical taper with core diameter of 8.2um, cladding diameter (not shown to scale) 125um, effective index n_{eff} 1.47, mode field diameter (at 1310nm wavelength) 9.2um, and radius of curvature of the polished lens r. For simplicity the beam exiting the SMF before the lens at point 1 is assumed to be a Gaussian beam with radius infinity and waist equal to the mode field diameter. This initial beam q_1 is expressed as

$$\frac{1}{q_1} = -i \frac{\lambda}{\pi n_1 \omega_1^2}$$

where λ=1.31um, n_1=1.47, and ω_1=9.2um. The beam q_1 can also be written as

$$q_1 = i z_1 \quad , \quad \text{where } z_1 \equiv \frac{\pi n_1 \omega_1^2}{\lambda}$$

The focal length of the lens can be found using the thin lens approximation, assuming a plano-convex lens with radius of curvature r and index n.

$$\frac{1}{f} \approx (n-1)(\frac{1}{r}) = (1.47 - 1)(\frac{1}{r})$$
$$f = \frac{r}{0.47}$$

The initial beam q_i first passes through a lens with radius of curvature of the lens r to point 2. Then from point 2 to point 3 the beam travels a working distance d in air to point 3, the location of the waist, or the narrowest part, of the beam.

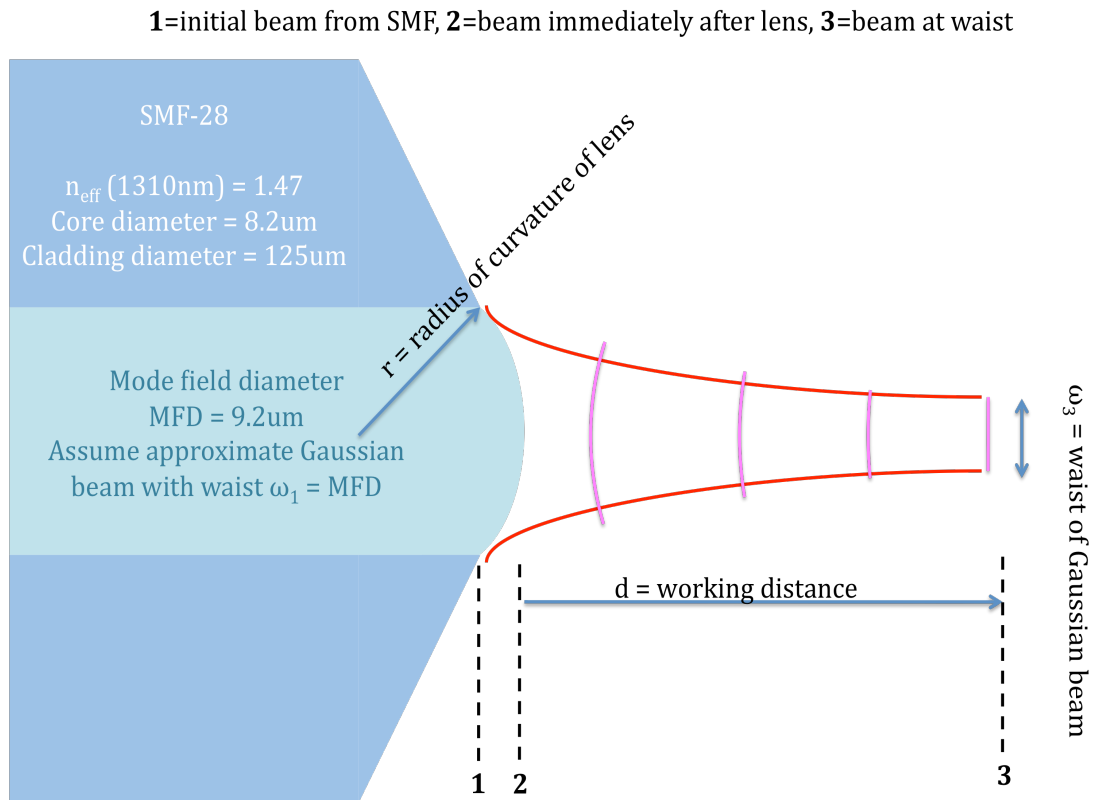**1**=initial beam from SMF, **2**=beam immediately after lens, **3**=beam at waist

Figure B-2   Gaussian beam approximation for conical lensed fiber. Diagram of optical beam coming out of a single-mode fiber with a conical lens tip, approximated by a Gaussian beam. Figure not drawn to scale.

Using ray transfer matrix analysis, any optical element such as a medium with certain distance or lens can be characterized as a 2 by 2 matrix with elements *A*, *B*, *C*, and *D*. The characteristic transform matrices for a Gaussian beam through a lens with focal length *f* and free space with distance *d* are listed below.

$$\begin{bmatrix} A & B \\ C & D \end{bmatrix} = \begin{cases} \begin{bmatrix} 1 & 0 \\ -\frac{1}{f} & 1 \end{bmatrix} & \text{for lens with focal length f} \\ \\ \begin{bmatrix} 1 & d \\ 0 & 1 \end{bmatrix} & \text{for air with distance d} \end{cases}$$

For more than one optical element the matrix is cascaded in order from right to left for matrix multiplication. In Figure B-2 the total ray transfer matrix is then

$$\begin{bmatrix} A_{total} & B_{total} \\ C_{total} & D_{total} \end{bmatrix} = \begin{bmatrix} 1 & d \\ 0 & 1 \end{bmatrix} \begin{bmatrix} 1 & 0 \\ -\frac{1}{f} & 1 \end{bmatrix} = \begin{bmatrix} 1 - \frac{d}{f} & d \\ -\frac{1}{f} & 1 \end{bmatrix}$$

The final complex beam parameter $q_f(z)$ is related to the initial $q_i(z)$ by:

$$q_f(z) = \frac{A_{total} q_i(z) + B_{total}}{C_{total} q_i(z) + D_{total}}$$

The location of point 3 is defined as the point of the Gaussian beam waist, where $\omega(z) = \omega_3$, the waist. In this case $1/q_3$ is zero, since the radius of curvature of the phase front R_3 is infinity. According to this definition, q_3 can be written as

$$\frac{1}{q_3} = -i \frac{\lambda}{\pi n_3 \omega_3^2}$$

where λ is still 1.31um and $n_3=1$, since the medium is air. The distance d is therefore

the unknown in this case. Applying the ray transfer matrix,

$$q_3 = \frac{q_1(1 - \frac{d}{f}) + d}{q_1(-\frac{1}{f}) + 1}$$

$$\frac{1}{q_3} = \frac{-\frac{q_1}{f} + 1}{q_1(1 - \frac{d}{f}) + d} = \frac{-i\frac{z_1}{f} + 1}{iz_1(1 - \frac{d}{f}) + d}$$

$$= \frac{(1 - i\frac{z_1}{f})(d - iz_1(1 - \frac{d}{f}))}{d^2 + z_1^2(1 - \frac{d}{f})^2}$$

$$= \frac{[d - \frac{z_1^2}{f}(1 - \frac{d}{f})] - i[(1 - \frac{d}{f})z_1 + d\frac{z_1}{f}]}{d^2 + z_1^2(1 - \frac{d}{f})^2}$$

$$= \frac{[d - \frac{z_1^2}{f}(1 - \frac{d}{f})]}{d^2 + z_1^2(1 - \frac{d}{f})^2} - i\frac{z_1}{d^2 + z_1^2(1 - \frac{d}{f})^2} \equiv -i\frac{\lambda}{\pi n_3 w_3^2}$$

The distance d between the lens and the point of the beam waist can be found by

taking only the real part of the left side of the equation above,

$$\mathrm{Re}(\frac{1}{q_3}) = \frac{[d - \frac{z_1^2}{f}(1 - \frac{d}{f})]}{d^2 + z_1^2(1 - \frac{d}{f})^2} \equiv 0$$

$$d = \frac{z_1^2}{f}(1 - \frac{d}{f})$$

$$d(1 + \frac{z_1^2}{f^2})\frac{f^2}{z_1^2} = \frac{z_1^2}{f}\frac{f^2}{z_1^2}$$

$$d(\frac{f^2}{z_1^2} + 1) = f$$

$$d = \frac{f}{1 + (\frac{f}{z_1})^2}$$

where f is related to r, the radius of curvature of the lens by $f=r/0.47$. The distance d

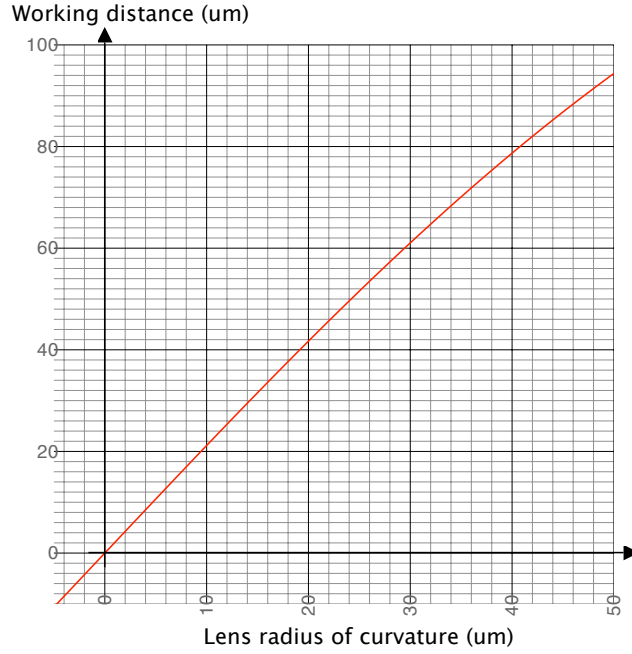from the lens to the beam waist is plotted as a function of r in Figure B-3.

Figure B-3 d versus r of curvature for conically lensed fiber.

The spot size, or waist at point 3, ω_3 is found by taking the imaginary part of $1/q_3$:

$$\mathrm{Im}(\frac{1}{q_3}) = -\frac{z_1}{d^2 + z_1^2(1-\frac{d}{f})^2} \equiv -\frac{\lambda}{\pi n_3 \omega_3^2}$$

$$-\frac{\lambda}{\pi n_3 \omega_3^2} = \frac{z_1}{d^2 + z_1^2 - 2\frac{d}{f}z_1^2 + z_1^2(\frac{d}{f})^2}$$

$$= \frac{z_1}{d^2(1+\frac{z_1^2}{f^2}) + z_1^2 - 2\frac{d}{f}z_1^2} \cdot \frac{\frac{f^2}{z_1^2}}{\frac{f^2}{z_1^2}}$$

$$= \frac{f^2/z_1}{d^2(1+\frac{f^2}{z_1^2}) + f^2 - 2df}$$

$$\text{From the Real part, } d = \frac{f}{1+(\frac{f}{z_1})^2}$$

$$\text{Im}(\frac{1}{q_3}) \equiv -\frac{\lambda}{\pi n_3 \omega_3^2} = \frac{f^2/z_1}{(\frac{f}{1+(\frac{f}{z_1})^2})^2(1+(\frac{f}{z_1})^2) + f^2 - 2(\frac{f}{1+(\frac{f}{z_1})^2})f}$$

$$= \frac{f^2/z_1}{\frac{f^2}{1+(\frac{f}{z_1})^2} + f^2 - 2(\frac{f^2}{1+(\frac{f}{z_1})^2})}$$

$$= \frac{f^2/z_1}{f^2 - (\frac{f^2}{1+(\frac{f}{z_1})^2})}$$

$$= \frac{1/z_1}{1 - (\frac{1}{1+(\frac{f}{z_1})^2})}$$

$$= \frac{1/z_1}{\frac{1+(\frac{f}{z_1})^2}{1+(\frac{f}{z_1})^2} - \frac{1}{1+(\frac{f}{z_1})^2}}$$

$$= \frac{1/z_1}{\frac{(\frac{f}{z_1})^2}{1+(\frac{f}{z_1})^2}}$$

$$= \frac{1}{z_1}\frac{1+(\frac{f}{z_1})^2}{(\frac{f}{z_1})^2}$$

$$= \frac{\lambda}{\pi n_1 \omega_1^2}\frac{1+(\frac{f}{z_1})^2}{(\frac{f}{z_1})^2}$$

Evaluating the equation above the beam waist or spot size ω_3 is found:

$$\omega_3^2 = \frac{\lambda}{\pi n_3} \frac{\pi n_1 \omega_1^2}{\lambda} \frac{(\frac{f}{z_1})^2}{1+(\frac{f}{z_1})^2}$$

$$\omega_3 = \omega_1 \frac{f}{z_1} \sqrt{\frac{n_1/n_3}{1+(\frac{f}{z_1})^2}}$$

Similarly to the working distance, with $f=r/0.47$, the beam waist or spot size ω_3 can be

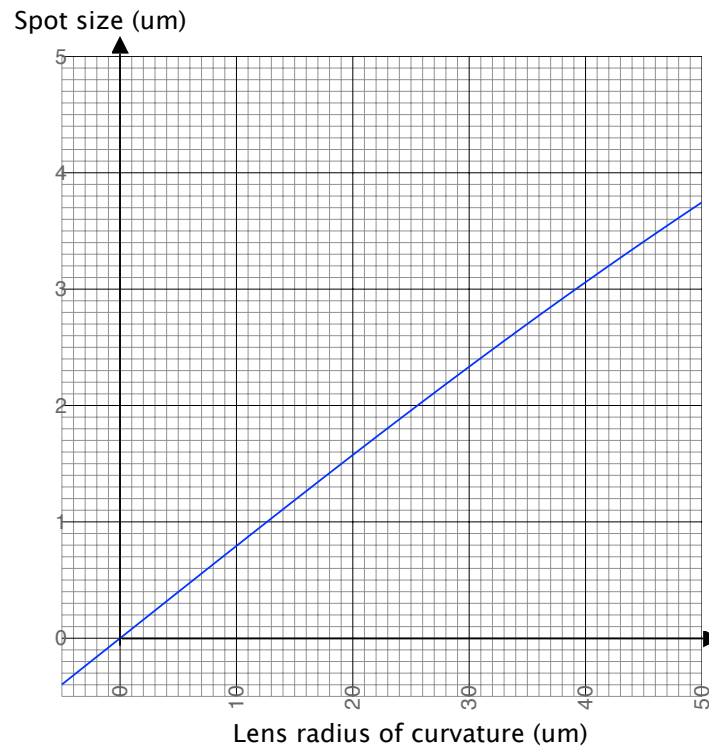plotted as a function of lens curvature radius r, as seen in Figure B-4.

Figure B-4   Spot size versus lens radius of curvature for conically lensed fiber.

Appendix C

Optical fiber alignment for solar spectral condenser

This appendix contains step-by-step instructions on how to align the optical fibers for the solar spectral condenser measurements.

Table C-1   Solar spectral condenser measurement input and output fiber alignment steps.

Step	Alignment	Evaluation
1	Fiber-to-fiber at close proximity	When SMF and MMF are close together, either fibers were moved to obtain maximum optical power read on handheld power meter.
2	Fiber-to-fiber distance at ~1mm (length of waveguide) in air. At this point, the waveguide positioner is set much lower than the fibers.	SMF and MMF were pulled apart to the distance approximate equal to the waveguide length. Either fiber was moved to obtain maximum optical power read on handheld power meter. If there was a significant offset between the original position and the maximum position, step 1 was repeated with the addition of adjusting the tilt and yaw angles of the fibers.
3	Device vertical axis is moved up slowly until waveguide is in the same line as the fibers. Device positioner resolution is 10um. (See Figure C-1)	After step 2, the power from fiber to fiber at ~1mm is noted. As the device moves up in the vertical axis, the waveguide will come in between the fibers, where the laser is properly coupled into the waveguide (<5um range). At this point the power read at the output is minimum. As the device is moved further up, the laser will be coupled into the substrate, and a relatively constant power is observed. When the device is completely above the fibers, the power drops to zero. This position should be equal to the thickness of the wafer. Finally, the waveguide is moved back to the position at which the laser was properly coupled.
4	Electrical connections were made for monitoring photocurrent.	Once the device position is set, electrical connections can be made. For the p-contact, a needle probe is placed on one of the metal pads on the device under test. For the n-contact, a microplunger clip is used to connect to a metal part of the device stage (usually one of the screws holding the copper mount is a good place to connect). The n-side of the wafer, fabricated with Ti/Pd/Au on the entire surface, was electrically connected to the copper mount via conductive epoxy Epotek H20E. Device under test was connected to a voltage source and current meter in series. Current is monitored in the next setup steps as well as throughout the measurement.

Table C-1   Solar spectral condenser measurement input and output fiber alignment steps, Continued.

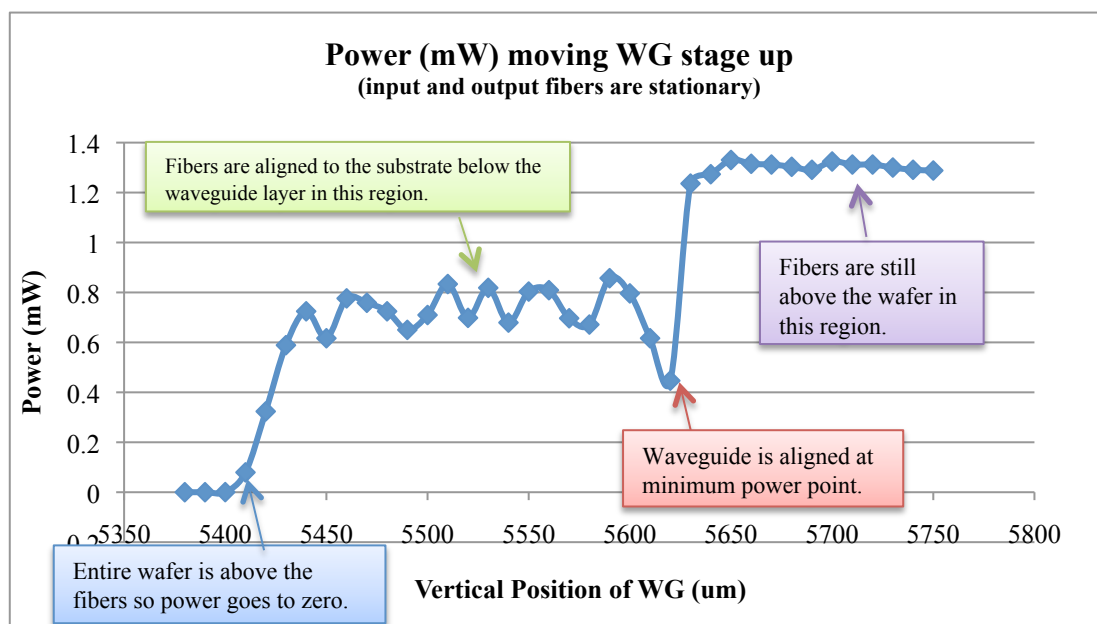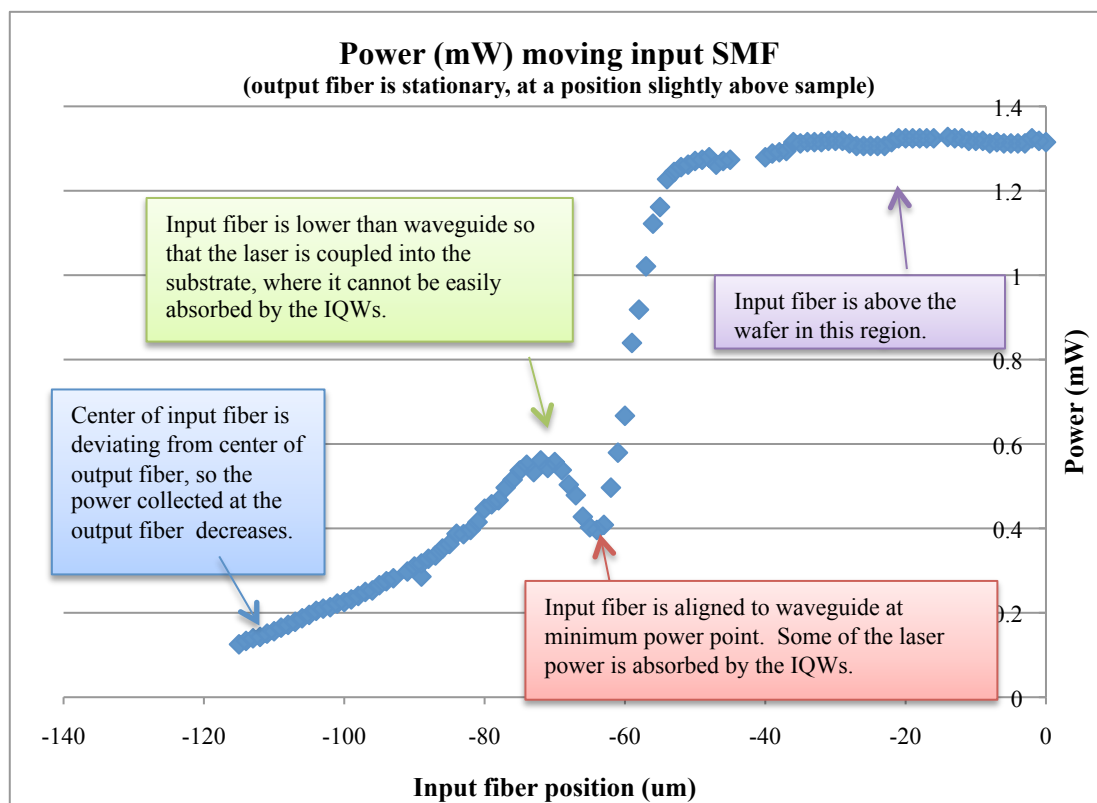| Step	Alignment	Evaluation
5	Input fiber is adjusted for *minimum* optical power and photocurrent. Fiber positioner resolution is 1um. (See Fig. C-2)	The input fiber is adjusted slightly to achieve *minimum* optical power. The point of minimum power indicates that the laser is optimally aligned to the waveguide, because the IQWs in the device are able to absorb the light from the laser. At the same time, the photocurrent is maximized, indicating that the laser photons were absorbed and generated carriers. The vertical axis is adjusted because step 3 can only roughly (~10um range) align the waveguide to the fiber. The horizontal axis (parallel to the edge of the device when looking from a bird's eye view) is adjusted because there could be regions on the facet of the device that have more or less loss. The last axis, which controls how far the fiber is from the wafer, is adjusted to optimize the working distance between the input fiber and the waveguide. The most sensitive and important axis is the vertical axis. The point of minimum optical power and maximum photocurrent is within the positioner's resolution range of 1um in the vertical direction. A slight deviation from this point results in an obvious drop in photocurrent and increase in optical power.
6	Output fiber is adjusted for maximum power.	After step 5, the input and output fibers may no longer be in a straight line. A slight adjustment of the output fiber can maximize the output power.

Figure C-1

Figure C-2